The Satellites and Stellar Halos of Nearby Milky Way-Mass Galaxies

by

Adam James Smercina

A dissertation submitted in partial fulfillment
of the requirements for the degree of
Doctor of Philosophy
(Astronomy and Astrophysics)
in The University of Michigan
2020

Doctoral Committee:

Professor Eric F. Bell, Chair
Associate Professor Jeremy Bailin
Professor David Gerdes
Professor Mario Mateo
Professor John-David T. Smith
Research Professor Monica Valluri

Deer Mountain, RMNP

Adam Smercina

asmerci@umich.edu

ORCID iD: 0000-0003-2599-7524

For Darian, my love and greatest friend.

ACKNOWLEDGEMENTS

This dissertation would not have been possible without the love and support of a number of very special people. I first want to thank my Mom and Dad. Throughout my formative years, you *always* encouraged me to ask questions — like: "how does Davis–Besse work?" (Davis–Besse is the local nuclear plant in Ottawa County, OH) — and think creatively. Whether I was interested in dinosaurs or LEGOs, you always provided me a space to grow and find myself. This encouragement and support ultimately fueled my creative spirit, my quest for greater knowledge, and my drive to follow my dreams. You have also continued to support me with unending enthusiasm through these later years, most importantly throughout my graduate career at Michigan. Whether it be driving to Ann Arbor and meeting for dinner or downloading and reading my papers as soon as they showed up on the arXiv (after learning what the arXiv *was*), you have remained constant pillars of support and joy in my life. None of my accomplishments, including this dissertation, would have been possible without you.

Next, I want to thank my twin brother, Drew. I think most people view their siblings as their early partners in life, but a twin is something different. We shared nearly every aspect of our early lives: playing, fighting, growing, and learning about the world. We have each found our own directions in life, both very different. Yet, even as we follow different paths, you continue to inspire me with your intelligence, groundedness, and resilience. Whether being 'Best Man' at my wedding, helping to change the brakes on my car, or driving to meet me at a conference in Aspen, you

continue to have such a positive influence on my life and I'm proud to call you my brother. Many times during the work which forms this dissertation, I have been frustratingly stuck by a problem and have asked myself "what would Drew do?" Thank you for your constant support and encouragement in all I do.

On a professional note, I have benefited from the support of countless people throughout my time at Michigan. I first want to acknowledge and thank the entire University of Michigan Department of Astronomy, especially the faculty who taught my graduate courses. My time at Michigan has been marked by such intellectual and professional growth and, though challenging at times, has culminated in a graduate education that I am proud of. This Department is a truly special place, full of special people, and I am exceedingly grateful to have had such a fulfilling graduate experience. I also want to thank my fellow graduate students. The support of one's fellow students is such an important part of 'surviving' the ups-and-downs of graduate school. Throughout all of the milestones — graduate coursework, prelim exam, job application season — the friendship and fellowship I found in my peers helped me to persevere. In particular, I'd like to thank Ryan Farber. Ryan, you and I have undergone this journey together from the start, and even further, during the UW Madison REU program. Throughout all of my time at Michigan, you have been a constant friend and colleague, always able to provide thoughtful insight on any problem.

I've also been fortunate, throughout nearly all of the work related to this dissertation, to have a close group of collaborators. In particular, I'd like to thank Antonela Monachesi, Jeremy Bailin, Colin Slater, and Paul Price. You have all been such a huge part of my growth as a scientist, helping me to write and refine nearly every paper and proposal I've produced thus far in my career. My work is inarguably better because of your thoughtful and insightful contributions, and friendship.

In the same vein, I'd like to thank the members of the Stellar Halos Group at

Michigan: Monica Valluri, Ian Roederer, Oleg Gnedin, Sarah Loebman, Kohei Hattori, Gillen Brown, and Molly Meng. The list is long, but each and every one of you has been part of my scientific community every week. Though many of you have moved on to other things, you have all played a huge role in making this weekly meeting a joy to attend over the years. My growth has been so impacted by all of our discussions, from arXiv papers to hot-off-the-press figures. You have often been the first group of people to which I have brought new results, and your insight has always proved useful. You have all been incredible mentors, colleagues, and friends and I cannot thank you enough.

Next, a few people deserve special thanks for their role in my professional development. First, I want to thank JD Smith. JD, you were my earliest scientific mentor, teaching me all of the initial skills one needs in this career: how to code, how to read papers, how to write. I have already passed on a number of your pearls of wisdom to many undergradute students, such as (parahrasing) "the computer doesn't *do* anything you didn't *tell* it to do". I truly believe that the freedom you gave me in my early research has helped shape me into the scientist I am today. I am especially fortunate to have been able to continue working with you as a colleague during graduate school. I'll never forget workshopping the 'After The Fall' paper on the phone, while driving across Iowa on my way to Colorado. Ritter will always feel like home because of your mentorship and friendship.

I'd also like to thank Richard D'Souza. I am so fortunate to have overlapped with you during your time at Michigan. You are truly one of the kindest and most insightful people I have met in this field, not to mention my life in general. Your diligent and creative approach to science is truly inspiring, and a model of the scientist I strive to be. So many of the ideas and results presented in this dissertation were inspired by our afternoon coffee chats, or joint discussions in Eric's office. I also consider you the 'master of the introduction'. So many of my proposals and papers in recent years

have been improved due to your critical eye and knack for seeing the story through the 'weeds'. I look forward to all of our collaboration in the future (you are now my excuse to visit Rome!). Thank you.

Last, but certainly not least of these special people, I want to thank my advisor, Eric Bell. Eric, my time working with you has truly been the highlight of my years at Michigan. Starting graduate school is such an enormous and often frightening step. Yet, from our first correspondence in my senior year at Toledo, I knew I had chosen the right advisor. For the past five years, your office has been such a safe, encouraging place for me. Coming up and knocking on your door, I've so often been met with the sight of you on your couch, feet up, hands behind your head, face reflective. This has *always* prefaced a stimulating scientific discussion, often a long one! Your enthusiasm is infectious, and your broad understanding of astrophysics is something I strive to emulate daily. But your real special power has been your ability to mentor me while also making me feel like a colleague, and that has been perhaps the single most valuable aspect of my entire graduate career. I will never forget our trip to observe with Subaru; you put me in the 'driver's seat', listened to my opinions, and made me feel like my interpretation of the observations were truly valuable. While I also love the 'lonely giant' project for other, scientific, reasons, our teamwork in building the story from beginning to end is the big one. I am sad that my time under your tutelage is coming to a close, but I look forward to our continued collaborative efforts. You have been a colleague, a mentor, and, above all else, a friend. Thank you for everything.

I also want to thank my dissertation committee: Eric Bell, Jeremy Bailin, David Gerdes, Mario Mateo, JD Smith, and Monica Valluri. Many of you have been mentioned elsewhere in these acknowledgements, but I want to separately express my gratitude to all of you for your part in the completion of this dissertation. I know that committee meetings can often be a source of stress for graduate students, but

that has never been the case for me. Over the last few years, you have been the best committee one could hope for, giving me the guidance, advice, and support I needed to get this dissertation to the finish line.

This next person comes last because of their unending, holistic contribution to my personal, as well as professional, growth: my wife, Darian. Darian, it's hard to find the words to express what your love has meant to me during the writing of this dissertation. You have accompanied me on all parts of this journey. You are the person I've celebrated with following my successes, as well as the person from whom I've drawn support and comfort following my failures. From helping me study for my prelim exam, to listening to practice-talks, and your proof-reading of proposals, manuscripts, and countless emails, your feedback and insight has been constant and invaluable. Your kindness, perseverance, and brilliance have inspired me in so many ways. This inspiration has, undoubtedly, been the cornerstone of this dissertation. I am so proud and overjoyed to have embarked on this journey of life with you, and I am certain of one thing: I could not have done this without you. For that, I dedicate this dissertation to you. Thank you from the bottom of my heart for your constant love and friendship.

Darian and I have embarked on a number of adventures together during my time in graduate school. These forays ranged from the woods of central Michigan to the lush rainforests of the Olympic Peninsula, high-alpine ridges of the Rockies, painted walls of the Grand Canyon, snow-covered wonderlands of the Cascades, and wildflower-covered slopes of Gran Sasso, to name a few. I have drawn such an inspiration from these diverse faces of nature. Included as the *frontispiece* of this dissertation is a picture of one such excursion in Rocky Mountain National Park, Colorado. Walking down a trail, the smell of crushed pine needles, peaks all around, and the loudest sound my own feet crunching along the rocky path: it is in these moments that I feel a true connectedness with the universe I study. Staring at the band of the Milky Way

under a dark sky, in the middle of the eastern Washington desert for example, gives an unbelievable sense of scale. The visible stars, star clusters, and dust lanes are but a hint of the full scale of the Galaxy, not to mention the countless others, such as the M81 triplet I often search for in my binoculars. At times like these, I appreciate in full the magnitude of what I do. Deciphering the origins of these shockingly complex and expansive systems we call galaxies begins to feel like the highest of callings.

"The trip has been long and the cost has been high,
but no great thing was ever attained easily. A long
tale, like a tall Tower, must be built a stone at a time."

— Stephen King, *The Dark Tower*

TABLE OF CONTENTS

LIST OF FIGURES

Figure

LIST OF TABLES

Table

ABSTRACT

The outskirts of galaxies like the Milky Way (MW) are important testing grounds for our understanding of galaxy formation and evolution. Models and observations agree that their vast accreted halos, while incredibly faint and difficult to observe, tantalizingly encode the properties of past merger events. Further, discrepancies between the predicted properties and distribution of their satellite galaxy populations constitute one of the most important open challenges to galaxy formation models. Yet, to-date, our observational insight in both of these regimes has been limited to the Local Group. To address this deficit, I have conducted a survey of the halos and satellite populations of two nearby galaxies with the Subaru Hyper Suprime-Cam. Using deep resolved stellar populations allows measurement of the stellar halo to unprecedented surface brightness depths and the detection satellites down to the threshold of ultra faint dwarf galaxies, such as the faint M81 satellite d1005+68. Though the survey is ongoing, these systems have yielded a number of important insights. The sparse satellite population of the 'lonely giant' M94 challenges all current model predictions, and suggests that low-mass galaxy formation could be more stochastic than previously thought. Additionally, I have used the stellar halo of M81 to show that it has experienced a surprisingly quiet accretion history to this point. Yet, its current interaction with M82 (and NGC 3077) will eventually result in one of the most massive stellar halos in the nearby universe, rivaling the behemoth M31. Lastly, building on these revelations of the unexpected diversity in satellite populations and merger histories of MW-mass systems, and including the numerous other recent satellite and stellar halo surveys of nearby systems, I investigate a possible relationship between

these two fundamental galactic components. Using data from seven nearby systems, I find a strong and previously-unknown positive correlation between their satellite populations and the mass of their most massive merger events. Surprisingly, current flagship galaxy formation simulations fail to reproduce this relationship — an acute shortcoming of the theoretical framework upon which our current galaxy formation paradigm is built.

CHAPTER I

Introduction

1.1 Galactic formation and structure in Cold Dark Matter

Our Galaxy: a complex amalgam of stars, gas, and dust, with each playing a distinct, nuanced role in maintaining the galactic ecosystem. The interplay between these components, mediated by radiation and gravity, forms the Milky Way (MW) as we see it from our 'Pale Blue Dot'. However, the band of light we see above us on a clear night is but a piece of a much larger galactic environment.

Humans have been studying the large-scale structure of the MW for thousands of years — long before the era of modern galactic astronomy. As an example, ancient bark paintings of the Large and Small Magellanic Clouds — the MW's largest satellite companions — have been found among the native peoples of Australia (*Mountford*, 1956). Aristotle's *Meteorologica* even suggests that some ancient Greek philosophers, such as Democritus, speculated that the *via lactea* (i.e. 'Milky Way') was composed of distant stars. Though we did not then have a sense of the scale of our own 'galactic neighborhood', we have since pieced together a cohesive picture of our Galaxy over the centuries. We now know that most of the MW's stars are embedded in a disk, which is host to several spiral arms, as well as a central stellar bar.

In the last century, our view of the Milky Way system expanded. It was discovered that numerous observed, confounding 'spiral nebulae' were actually distinct galactic

systems from our Galaxy (*Hubble*, 1925). This revolution in our understanding of the universe resulted in the realization that the MW actually resides within a relatively rich 'group' environment. This group includes a number of much less massive, gravitationally-bound 'satellite' galaxies (*Baade and Hubble*, 1939), which reside in the MW's halo, as well as a close neighbor — M31, the Andromeda galaxy — less than 1 Mpc away (e.g., *Hubble*, 1925; *Schmidt-Kaler*, 1967), with its own population of satellite galaxies (*van den Bergh*, 1974). Around the same time, it was discovered that the MW has another, much more extended component: a *stellar halo*. Stars in the stellar halo were found to exist at substantially larger distances than the disk, and, rather than following disk-like orbits, these stars follow orbits that are much more random, with low net angular momentum (e.g., *Spitzer and Shapiro*, 1972). Not only did we learn that there are nearly innumerable distinct galaxies in the universe, but our own MW extends far beyond its visible disk (that so enthralled ancient humans) and resides at the center of a vast ecosystem.

With this newfound insight into the structure of the universe, the field began searching for a model which could describe this seemingly hierarchical distribution of matter in the universe. Early models suggested that galaxies like the MW form via top-down collapse: first forming giant, galaxy group-scale clouds of gas (i.e. 'proto-galaxies') and fragmenting to form galactic disks and globular clusters (*Eggen et al.*, 1962; *Larson*, 1969; *Tinsley and Larson*, 1978) — akin to prevailing theories of the formation of stars within molecular clouds (e.g., *Shu et al.*, 1987). However, while relatively successful in producing disk galaxies, these models struggled to explain the observed clustering of galaxies and the full range of galaxy masses and morphologies (e.g., *Peebles*, 1978; *Tohline*, 1980). Around this same time, a vastly different model was rapidly gaining acclaim: cold dark matter (CDM). Evidence from the divergence (flattening) of spiral galaxy rotation curves (e.g., *Rubin*, 1983), relative to Keplerian expectations, as well as the mass distributions of galaxy clusters (e.g.,

Clowe et al., 2004), suggested that galaxies actually reside in much larger halos of 'dark matter'. The stellar halo of the MW appears to be largely spatially coincident with this extended mass distribution. Rather than 'top-down' fragmentation, galaxy formation proceeds in these hierarchically-assembled dark matter halos, with smaller halos merging to form larger larger structures. Galaxy formation within these hierarchical dark structures much better explains the observed clustering of galaxies (*White and Rees*, 1978). In the years since, dark matter has become the central player in our theory of structure formation in the universe.

In the current CDM paradigm, following Big Bang nucleosynthesis and the production of a 'primordial soup' of highly-ionized Hydrogen and Helium nuclei, dark matter, with little initial kinetic energy, forms quantum density perturbations in the early universe, which then grow as the universe expands (e.g., *Press and Schechter*, 1974; *Peebles*, 1982). As these density perturbations grow to form early dark matter halos (DMHs), the ionized medium eventually cools and recombines as the universe expands, forming neutral Hydrogen and Helium. Following this recombination, the newly-released baryons fall into these ready-made dark matter halos, setting the stage for the era of galaxy formation (*Ryden and Gunn*, 1987). The scientific direction of observational astronomy was shaped by this new cosmological model. The new millennium ushered in a new era of wide-field, digital galaxy redshift surveys — imaging and obtaining spectra for millions of galaxies. The striking similarity between the large-scale structure produced in dark-matter-only (DMO) simulations and the observed structure seen in these surveys, such as the Sloan Digital Sky Survey (SDSS; *York et al.*, 2000) and the more recent Dark Energy Survey (DES; *Melchior et al.*, 2015), serves as some of the strongest evidence in favor of the CDM model of the universe.

Yet, numerous mysteries remain. As dark matter is not (currently) directly detectable, the most viable method of testing and constraining the CDM model is

studying how baryonic matter behaves in dark matter's presence. Galaxies in the observable universe display a broad diversity of properties, including their masses, morphologies, baryonic content, levels of star formation, and environments. Yet, all of the complexity of galaxies — their interactions and evolution — is a façade covering their much more massive reservoirs of dark matter. These dark matter halos likely govern the assembly and evolution of galaxies in diverse and complex ways, driving the formation and evolution of galaxies like our MW, and their associated structures.

1.2 Challenges to CDM at Dwarf Galaxy Scales

Though seemingly insignificant relative to massive galaxies such as the MW, or behemoths such as giant ellipticals, dwarf galaxies are among the most important galaxy populations for testing and refining the CDM model. CDM predicts that cosmic structure grows hierarchically, with the smallest dark matter structures associated with and 'feeding' the largest structures. The properties of these smallest structures (i.e. halos) are among the most robust predictions of the CDM model, yet we can only detect and study the halos which host baryons. Thus an optimal testing ground for CDM is the regime where halos are massive enough to hold onto some baryons, but the existing baryons are vastly outweighed by dark matter: this is the realm of dwarf galaxies. It is at precisely these dwarf galaxy scales that some of the largest tensions between the CDM model and observations exist.

More than two decades ago, results from dark matter-only (DMO) simulations brought into focus a tension between the number of dark matter subhalos predicted to exist within a halo similar to that of our MW and the number of observed, luminous satellite galaxies, which should reside in these subhalos (*Klypin et al.*, 1999; *Moore et al.*, 1999) — the 'Missing Satellites' problem. Since then, it has become clear that, indeed, the number and mass distribution of the subhalos produced in these DMO simulations differ from the properties of observed dwarf galaxy populations our Local

Group (LG) environment. In addition to the 'Missing Satellites' problem, there has long been a discrepancy between the observed mass distribution and rotation curves in low surface brightness (LSB) galaxies (*McGaugh and Bothun*, 1994; *Zwaan et al.*, 1995; *McGaugh and de Blok*, 1998; *van den Bosch et al.*, 2000). Upon discovery that this discrepancy extended to nearby dwarf galaxies, which defied the 'cusp'-like mass profiles predicted in CDM in favor of central cores (*Simon et al.*, 2003; *Weldrake et al.*, 2003; *Simon et al.*, 2005), the tension was generalized as the 'Core–Cusp' problem. A recasting of this problem found that the central velocities of the brightest MW satellites, measured from spectroscopy of individual stars (e.g., *Mateo et al.*, 1991, 1993; *Armandroff et al.*, 1995; *Mateo et al.*, 1998), which should also reside in the most massive subhalos, are substantially lower than CDM predictions for these most massive subhalos (*Boylan-Kolchin et al.*, 2011) — the 'Too Big to Fail' problem.

Motivated largely by these tensions, the past decade has seen an explosion of dwarf galaxy science. Both the MW and M31 were already known to host approximately 10 low-mass dwarf satellite galaxies each, with many more in the large-scale Local Group environment (e.g., *Mateo*, 1998, and references therin). However, with the advent of digital sky surveys, a new class of 'ultra faint' dwarf galaxies (UFDs) were discovered (e.g., *Willman et al.*, 2005a,b; *Zucker et al.*, 2006a,b; *Belokurov et al.*, 2006, 2007; *Simon and Geha*, 2007, and others) with stellar masses less than $\sim 10^5\ M_\odot$[1] (see *McConnachie*, 2012, for a more recent census that includes many of these faint discoveries). These UFDs have such low surface brightness that they are undetectable in traditional astronomical imaging. Their detection requires the identification of a concentration of resolved stars in a color–magnitude diagram (CMD). The discovery of these UFDs bridged the gap between our more solid understanding of galaxy formation physics at large scales and our dearth of knowledge about how small galaxies form. These UFDs are extreme dwarf galaxies, with nearly uniform ancient stellar

[1] $M_\odot$ = The mass of the sun

populations — suggesting that the majority of their star formation ended many billions of years ago, in contrast with normal galaxies. The most common interpretation of this early star formation shutdown is that the halos in which these tiny galaxies formed are of such low mass that their virial temperatures were below the temperature of the intergalactic medium (IGM) at the time of reionization and, thus, their growth quickly halted (e.g., *Bullock et al.*, 2001; *Benson et al.*, 2002). Recent observations have refined this idea, suggesting UFDs ($M_\star < 10^5\,M_\odot$) form >80% of their stars by $z = 2$, compared to ∼30% for higher-mass galaxies (*Brown et al.*, 2014; *Weisz et al.*, 2014).

Simultaneously, work continued on the discrepancy between observed and predicted dwarf galaxy mass distributions. Motivated by the 'Core–Cusp' and 'Too Big to Fail' problems, there was substantial progress on physical avenues that could lead to the observed velocity differences — feedback from star formation was an early proposition (*Navarro et al.*, 1996). In the last decade, models which include baryons have begun to show the viability of feedback from star formation — mainly supernovae (SNe) and winds from massive stars (e.g, *McKee and Ostriker*, 1977) — as a substantial agent in effecting changes to the central dark matter distribution in intermediate DMHs (e.g., *Macciò et al.*, 2010; *Font et al.*, 2011). Further evidence has shown that for DMHs in the mass range of 10^{10}–$10^{11}\,M_\odot$ — precisely where the 'Cusp–Core' and 'Too Big to Fail' problems are most contentious — these winds are predicted to be efficient at driving rapid expulsion and or redistribution of gas at the potential's center (*Brooks et al.*, 2013; *Wetzel et al.*, 2016).

Despite this important progress, robust comparisons between observed dwarf galaxy populations and modern hydrodynamic simulations remain largely elusive. The baryonic mass resolution required to simulate low-mass 'classical' dwarfs, let alone UFDs, prohibits many models from producing them. For example, field-standard cosmological hydrodynamic models, such as Illustris (*Pillepich et al.*, 2014; *Vogels-*

berger et al., 2014) or EAGLE (*Schaye et al.*, 2015), are only able to confidently resolve dwarf galaxies with stellar masses $M_\star > 10^8\,M_\odot$ (e.g., *Elias et al.*, 2018). More crucially, the relationship between the stellar masses and DMH masses — the 'stellar mass–halo mass' (SMHM) relation (*van den Bosch et al.*, 2003; *Berlind et al.*, 2003; *Conselice et al.*, 2005; *Yang et al.*, 2008; *Behroozi et al.*, 2013) — of these low-mass dwarfs is substantially shallower (biased to high stellar masses) than the most current constraints from observations. Yet, these observational constraints are also fraught with uncertainty. Currently, every single dwarf galaxy which has both a robust stellar mass measurement and an estimate of its dynamical mass from resolved stellar kinematics is a satellite of either the MW or M31. Consequently, many may have experienced some loss of mass — i.e. tidal processing — due to the group environment (e.g., *Mayer et al.*, 2001; *Zolotov et al.*, 2012), leading to substantial uncertainty in what their DMH mass may have been at the time of formation (i.e. 'peak' halo mass), which, in CDM, is what should set the initial stellar mass of the galaxy. As such, the field still lacks a robust model of which DMHs the lowest-mass galaxies inhabit.

1.3 Merging and Accretion as Drivers of Galaxy Evolution

Another consequence of the hierarchical growth of structure predicted in CDM is frequent interactions — i.e. 'mergers' — between galaxies (e.g., *White and Rees*, 1978; *Bullock et al.*, 2001). These galaxy mergers are predicted to have potentially drastic impacts on galaxies and their dark matter halos, including the growth of stellar mass, morphology, and dynamical structure (*Toomre and Toomre*, 1972). Due to the conservation of momentum, mergers between galaxies funnel gas to the center of the joint gravitational potential, often stimulating the formation of new generations of stars, and enriching the existing interstellar medium (ISM) with metals from these newly formed stars (*Barnes and Hernquist*, 1991).

These mergers can be massive, with merger ratios — the mass ratio of the 'sec-

ondary' compared to the 'primary' — close to unity and representing a significant stellar mass growth pathway (e.g., *Gallagher and Ostriker*, 1972; *Richstone*, 1976), or can be much smaller 'accretions' of dwarf satellites by the central galaxy. These smaller accretions are by far the most common mode of galaxy interaction. As the secondary falls into the central potential, it experiences increasing tidal forces, until it eventually disrupts completely — as is currently occurring to the Sagittarius dwarf galaxy around the MW (*Ibata et al.*, 1994). Throughout the tidal disruption process, a substantial amount of material from the accreting satellite is deposited at large galactic radii. The composite reservoir of accreted stellar material from all accretion events resides in the stellar halo (e.g., *Spitzer and Shapiro*, 1972; *Searle and Zinn*, 1978).

The significance of these merger events to galaxy evolution has remained one of the primary open questions in extragalactic astronomy for the better part of the last century. Much of the work in that time has regarded galaxies currently in the midst of merger events, such as the seminal paper of *Toomre and Toomre* (1972), as, though locally rare, these events are highly distinct and, therefore, easier to study. From the generation of large, statistical galaxy samples, gathered across broad swaths of both the sky, such as Galaxy Zoo with SDSS (*Darg et al.*, 2010), and redshift, such as CANDELS with *HST* (e.g., *Grogin et al.*, 2011), galaxy mergers have emerged as the most oft-suggested primary drivers of numerous fundamental galaxy properties. These include the growth of stellar bulges (e.g., *Baugh et al.*, 1996; *Kauffmann*, 1996; *Aguerri et al.*, 2001; *Springel and Hernquist*, 2005; *Eliche-Moral et al.*, 2006; *Hopkins et al.*, 2010), the growth of central supermassive black holes (SMBHs), including the triggering of quasars, and the formation of giant elliptical galaxies (e.g., *Springel et al.*, 2005; *Hopkins et al.*, 2006), and the origin of infrared-luminous galactic starbursts (*Sanders and Mirabel*, 1996; *Hopkins et al.*, 2006; *Armus et al.*, 2009). Yet, as these properties are both diverse (e.g., the properties of stellar bulges) and rare (e.g.,

the occurrence of quasars and starbursts), extracting unbiased inferences about how merger history impacts galactic evolution can be difficult.

An alternative approach would be to focus on nearby galaxies, for which their merger histories can be extracted both more extensively (i.e. more ancient merger events) and in greater detail. The two best case studies we have at our disposal to better understand the impact of mergers on galaxies are our own MW and our nearest neighbor, M31, The Andromeda Galaxy. A relatively substantial merger is occurring in our own backyard: the MW itself is currently interacting with its two largest satellites, the Large and Small Magellanic Clouds (e.g., *Kerr*, 1957), in addition to the Sagittarius dwarf galaxy (*Ibata et al.*, 1994). There has been much discussion about the impact these interactions have had on our galaxy, such as warping of the galactic disk (*Kerr*, 1957; *Fujimoto and Sofue*, 1976; *Spight and Grayzeck*, 1977; *Davies and Wright*, 1977; *Laporte et al.*, 2018), and on the buildup of the MW's stellar halo (e.g., *Helmi and White*, 1999; *Bullock and Johnston*, 2005; *Bell et al.*, 2008).

Recently, our view of the MW's assembly has been transformed. The *Gaia* spacecraft (*Gaia Collaboration et al.*, 2016), launched in 2013, has currently measured the parallax distances and proper motions of more than one billion stars in the MW, and radial velocities for more than six million (as of Data Release 2; *Gaia Collaboration et al.*, 2018). These data from *Gaia* have allowed the separation of MW disk and halo stars using their kinematics, allowing the discovery of numerous new halo streams and substructures (e.g., *Malhan et al.*, 2018), revealing the MW's rich accretion history. With the vastly improved distinguishing power of *Gaia*, a distinct population of MW halo stars was identified with radial orbits and high metallicities. These stars are thought to be the remnants of a significant ancient merger event, coined 'Gaia-Enceladus', which may have been the origin of the MW's chemically-distinct 'thick disk' (*Helmi et al.*, 2018).

Our view of our neighbor M31 has been similarly transformed. Detailed studies of M31 have revealed the history of our neighbor system in never-before-seen-detail. The Panchromatic Hubble Andromeda Treasury (PHAT) survey (*Dalcanton et al.*, 2012) used the *Hubble Space Telescope* (*HST*) to resolve more than 100 million individual stars across $\sim$1/3 of M31's disk. PHAT leveraged the essentially common distances of these stars (i.e. all at the 780 kpc distance of M31, as opposed to studies of stars in the MW) to study properties such as M31's star formation history (SFH; e.g., *Williams et al.* 2015), its dust content (e.g., *Dalcanton et al.*, 2015), and its lifetime transport of metals (e.g., *Telford et al.*, 2019). Likewise the first of its kind, the Pan-Andromeda Archaeological Survey (PAndAS; *McConnachie et al.* 2010) used several hundred hours on the Canada-France-Hawaii Telescope (CFHT), with the MegaCam wide-field imager, to perform a wide-field survey of M31 out to 150 kpc in galactic radius — more than 300 deg^2 in all, spread over four years. With this exquisite first-of-its-kind dataset, PAndAS resolved nearly all of M31's stellar halo in unprecedented detail.

Together with additional studies, such as the Spectroscopic and Photometric Landscape of Andromeda's Stellar Halo (SPLASH) survey (*Gilbert et al.*, 2012), these ground-breaking surveys provide a powerful window onto M31's history: it appears to have experienced a substantial merger event — with a 1:2–1:4 merger ratio — approximately 2–4 Gyr ago[2] (*Hammer et al.*, 2018; *D'Souza and Bell*, 2018b). This merger appears to have had a substantial impact on M31's properties. Around the same time as the merger, M31's disk was thickened to a nearly 1 kpc scale height (*Dalcanton et al.*, 2015; *Williams et al.*, 2015) — 3$\times$ thicker than the MW's disk at a comparable radius. These intermediate-age disk populations, traced by several Gyr-old giant-branch stars also possess substantially higher velocity dispersions — $\sim$90 km s^{-1} — than comparable MW populations (*Dorman et al.*, 2015). Moreover,

[2] 1 Gyr = 1 billion years

the entire disk of M31 appears to have undergone a burst of star formation commensurate in time with the final stages of this large merger, followed by a general decline — or 'quenching' — of its star formation up to the present day (*Williams et al.*, 2015, 2017).

Together, the MW and M31 show us that even for galaxies of approximately the same mass and structure — i.e. disk galaxies with stellar mass $M_\star \simeq 5\times10^{10}\,M_\odot$ — may have experienced very different 'dominant' mergers throughout their lives. The MW experienced a much earlier, much lower mass merger, relative to M31, whose large dominant merger event was quite recent. This stark contrast suggests that there is considerable diversity in the mergers that MW-mass galaxies experience, yet the magnitude of this diversity remains unclear.

1.4 The Importance of Placing the Local Group in Context

Though they are comparable in mass (MW: $M_\star = 6.1\times10^{10}\,M_\odot$, *Licquia and Newman* 2015; M31: $M_\star = 11.7\times10^{10}\,M_\odot$, *Geehan et al.* 2006, *Sick* 2018), the MW and M31 are quite different. First, they have very different structure; M31's disk is thicker than the MW's and it possesses a substantially larger central bulge. Their merger histories are also very different, with M31 experiencing a much larger and much more massive merger, which may contribute to their structural differences (e.g., § 1.3). M31 also hosts roughly twice the number of satellites at all galactic radii within 150 kpc (e.g., *McConnachie*, 2012). Moreover, recent evidence suggests that the satellite radial profiles are very different, with the MW possessing very few satellites beyond 150 kpc (*Samuel et al.*, 2020). How do these two different systems generalize to galaxy populations at large?

Even as the nearest examples, studying the satellites and stellar halos of both the MW and M31 present considerable observational difficulties. Both components possess very low surface brightness, requiring either sensitive imaging with well-controlled

scattered light and precise background estimation (e.g., *Malin and Hadley*, 1997), or deep photometry of faint, individual stars (e.g., *Ibata et al.*, 2001). As such, over the last several decades, during the time that the CDM model and CDM-founded galaxy formation have come to the fore, our Local Group has served as the benchmark. As such, the properties of MW-mass systems have directed the scope of some of the most important problems in galaxy formation. Models predict that they should experience diverse merger histories, manifesting in diverse stellar halo properties (e.g., *Bullock and Johnston*, 2005; *Deason et al.*, 2015a), and should also exhibit some diversity in their satellite galaxy populations, including their SFHs (e.g., *Simpson et al.*, 2018; *Garrison-Kimmel et al.*, 2019a,b). Yet, with the Local Group serving as the sole benchmark of the validity of model predictions in this critical regime of galaxy formation, we have no reliable method to determine the true scatter in these fundamental properties. The processes which give rise to these properties — e.g., dark matter–baryon interactions, feedback processes, evolution in group environments, the galaxy stellar mass function — are thus intrinsically tied to the generalizability of the MW and M31 systems; *a fragile 'house of cards' foundation for galaxy formation.*

The optimal way to alleviate this potential 'house of cards' is to study the satellite populations and stellar halos of nearby MW-mass systems (e.g., central galaxies with stellar masses of $M_\star > 3\times10^{10}$), to help place the MW and M31 in context. Great strides have recently been made towards this goal, with a number of different approaches taken, including: (1) integrated light surveys (e.g., *Chiboucas et al.*, 2009; *Martínez-Delgado et al.*, 2010; *Merritt et al.*, 2016; *Watkins et al.*, 2016), (2) narrow-field *HST*-based resolved star surveys (e.g., *Radburn-Smith et al.*, 2011; *Rejkuba et al.*, 2011), (3) wide-field resolved star surveys (e.g., *Martin et al.*, 2013; *Ibata et al.*, 2014; *Crnojević et al.*, 2016; *Carlin et al.*, 2016), and (4) wide-field spectroscopic surveys (e.g., *Geha et al.*, 2017). These studies not only vary in technique, but also in radial coverage, photometric detection limits, surface brightness depth, and

image resolution, often making comparisons to each other, and to the Local Group, difficult.

In general, most studies of MW-analog satellite populations have thus far been sensitive only to dwarf galaxies well within the MW's 'classical' mass regime — $M_V < -10$, $M_\star > 10^6$. As such, it has taken some care to contextualize the results of these surveys with the MW, particularly given the discovery of UFDs. Even so, these works have provided useful context. Many MW-analogs in the nearby Universe, such as M81 (*Karachentsev and Kudrya*, 2014), Centaurus A (*Müller et al.*, 2015b; *Crnojević et al.*, 2019), and NGC 4258 (*Spencer et al.*, 2014), appear to host substantially more satellites than the MW, comparable to M31. Likewise, some appear to host less than expected, such as NGC 253 (e.g., *Carlin et al.*, 2016). Additionally, while nearly every MW satellite with $M_\star < 10^7\,M_\odot$ is quenched (e.g., *Slater and Bell*, 2014), this may not be the case around other hosts (e.g., *Spencer et al.*, 2014; *Carrillo et al.*, 2017; *Geha et al.*, 2017). These results are tantalizing evidence of a diversity in the satellite populations of MW-mass galaxies.

Similarly, the stellar halos of a number of nearby galaxies have now been studied using a variety of techniques, each with their own merits and challenges. Programs such as the Dragonfly Nearby Galaxy Survey (*Merritt et al.*, 2016), using the Dragonfly Telephoto Array (*Abraham and van Dokkum*, 2014), have now studied the global diffuse stellar halos of more than a dozen galaxies within the Local Volume. However, while integrated light techniques can provide stellar mass estimates, this requires assumptions regarding the stellar populations present, as they do not resolve individual stars. This also precludes measurement of more direct properties, such as metallicity, age, or recent star formation, making inferences about the merger history from the stellar halo difficult. In contrast, deep individual star measurements with *HST*, as was done in the Galactic Halos, Outer disks, Substructure, Thick disks, and Star clusters (GHOSTS) survey (*Radburn-Smith et al.*, 2011), can directly measure these

properties of the stellar halo populations. The weakness of such surveys is that they necessarily cover only small fractions of stellar halo, due to *HST*'s small field-of-view (FOV), relative to ground-based telescopes. GHOSTS, for example, targets fields along the major and minor axes of the observed galaxies. This is potentially limiting, as models of stellar halos suggest that they are highly structured (e.g., *Bullock and Johnston*, 2005). Last is the hybrid method of employing wide-field imagers on large telescopes to resolve stellar halo populations on large scales, modeled after the PAndAS survey. This method provides comparable area to the best integrated light surveys, while also providing the advantages of resolved stellar populations. However, the ground-based image quality is substantially poorer than *HST*, resulting in much higher 'contamination' from distant, background galaxies that are small enough to resemble stars in the ground-based imaging. Thus, achieving comparable fidelity to *HST*-based measurements requires significant care.

With the results from these numerous recent studies in hand, the field has begun the difficult task of deciphering the stellar halos of these nearby galaxy samples. Results from surveys such as Dragonfly and GHOSTS indicate that MW-mass galaxies exhibit a diversity of stellar halo properties, including masses (*Merritt et al.*, 2016; *Harmsen et al.*, 2017), shape (*Harmsen et al.*, 2017), and metallicity (*Monachesi et al.*, 2016a). A possible complication presents itself in the form of *in situ* stars — stars which formed in the central potential, but which have been kicked out to larger galactic radii, representing a potentially significant confounding population when attempting to decipher the accreted stellar populations (*Purcell et al.*, 2010; *Pillepich et al.*, 2015; *Monachesi et al.*, 2019). However, recent comparisons between these observational results and galaxy formation models indicate that this diversity in stellar halo properties is likely grounded in differences in the stellar populations these galaxies have *accreted*, due to experiencing different merger histories (*Monachesi et al.*, 2016b; *D'Souza and Bell*, 2018a; *Monachesi et al.*, 2019) — as has been hinted

at by the stark difference between the MW and M31.

It is clear from studies of both the satellite populations and stellar halos of nearby galaxies that the context they provide is sorely needed. Though approached using a variety of methods, the satellite populations of MW-mass galaxies in the nearby universe are clearly diverse, both in number and star formation properties. Likewise, stellar halo surveys appear to present an encouraging route to deciphering the apparently diverse merger histories experienced by MW-mass galaxies. Moving forward with more complete surveys, the question now becomes: does this diversity in the large-scale properties of MW-mass systems fit with, or require modifications to, our understanding of galaxy formation?

1.5 Aims of this work

Substantial progress has been made in our understanding of the assembly of the MW and the Local Group, including their satellite galaxy populations and merger histories — both of which have strong predictions in CDM. The success of improved galaxy formation models, including baryons, at easing tensions between observed satellite galaxy properties (see § 1.2) has led to pronouncements that these problems have been solved (e.g., *Simon and Geha*, 2007; *Kim et al.*, 2017). However, we understand little about how generalizable the MW and M31 truly are. Galaxy formation models are often specifically tuned to produce Local Group-like galaxy groups and reproduce satellite galaxy populations comparable to the MW and M31 (e.g., *Simpson et al.*, 2018; *Garrison-Kimmel et al.*, 2019a), due in large part to the dearth of complete satellite surveys for other MW-analogs. Yet, these same simulations often fail to reproduce merger histories comparable to the MW, or other low-mass halos such as M81 (*Harmsen et al.*, 2017) or M101 (*Jang et al.*, 2020), instead predicting more massive, more recent accretions for most simulated MW-mass systems (e.g., *Sanderson et al.*, 2018; *Monachesi et al.*, 2019). Is the MW unusual in this regard?

Alternatively, is its satellite population typical, and thus appropriately generalizable, afterall? Until we understand how these properties of the MW compare to other similarly massive galaxies, much of our galaxy formation foundation is built on a 'house of cards'.

This work attempts to alleviate the current lack of context regarding the satellite populations and merger history of the MW, which in many cases serve as solitary tests of the CDM model. *Is the MW representative of galaxies at its mass scale and how might the answer impact our understanding of galaxy formation?*

Specifically, this work introduces new observations of the outskirts of two nearby MW-mass central galaxies — analogs of our own MW — including their satellite populations and stellar halos. Until about 10 years ago, we had a strikingly poor understanding of the large-scale structure of nearby MW-mass systems, relative to our own galaxy. This work includes new resolved-star techniques for detecting faint satellite galaxies in these distant systems and measuring their stellar halos, and attempts to contextualize these new measurements with all recent literature results. For the first time, the satellite populations and stellar halo properties have been measured for a sample of MW-analogs.

Chapter II will present the discovery of a new faint satellite around M81, as part of a deep resolved-star survey with the Subaru Hyper Suprime-Cam (HSC). As one of the faintest galaxies every detected outside of the Local Group, as well as potentially the first known 'satellite-of-a-satellite' (predicted in a 'self-similar' CDM model), this work will contribute to ushering in a new era of dwarf galaxy discovery in the coming decades. Chapter III presents a Subaru HSC survey of the nearby galaxy M94. In this survey, reaching out to a projected radius of 150 kpc from M94, only two low-mass satellite galaxies were detected, despite being sensitive to all dwarf galaxies within the MW's 'classical' dwarf mass range ($M_\star \gtrsim 4\times10^5\,M_\odot$). This is in stark contrast with the MW's eight satellites and M31's 12 within the same radius — a completely

unexpected result. Moreover, when compared to predictions from galaxy formation simulations, M94's sparse satellite population is in tension with all current models, suggesting that our small-scale problems with CDM are not yet solved.

Chapter IV follows the survey of M81 presented in Chapter II, focusing on a global view of M81's stellar halo. This is the most detailed map of a stellar halo outside of our own Local Group ever constructed. Though M81's stellar halo is found to be currently low-mass and metal-poor, its current interaction with M82 and NGC 3077 is shown to foreshadow the creation of an enormous, M31-like stellar halo in the near-future. Chapter V introduces new, unpublished work on a compilation of nearby galaxy satellite populations and stellar halo properties. Combining the work in Chapter III and Chapter IV with recent studies of other MW-analogs, this work defines a new metric for the largest merger a galaxy has or will experience. Using this new metric, this new work finds a strong relationship between the largest merger experienced by a MW-mass galaxy and its total number of satellites above $M_\star \gtrsim 4{\times}10^5\,M_\odot$. Surprisingly, this relationship is not seen in any current galaxy formation model, likely due to the complexities of star formation feedback in and tidal processing of satellites. Chapter VI summarizes the work presented here and presents an outlook on how this work will contribute to related future efforts.

CHAPTER II

d1005+68: A New Faint Dwarf Galaxy in the M81 Group

2.1 Abstract

We present the discovery of d1005+68, a new faint dwarf galaxy in the M81 Group, using observations taken with the Subaru Hyper Suprime-Cam. d1005+68's color-magnitude diagram is consistent with a distance of $3.98^{+0.39}_{-0.43}$ Mpc, establishing group membership. We derive an absolute V-band magnitude, from stellar isochrone fitting, of $M_V = -7.94^{+0.38}_{-0.50}$, with a half-light radius of $r_h = 188^{+39}_{-41}$ pc. These place d1005+68 within the radius–luminosity locus of Local Group and M81 satellites and among the faintest confirmed satellites outside the Local Group. Assuming an age of 12 Gyr, d1005+68's red giant branch is best fit by an isochrone of [Fe/H] $= -1.90 \pm 0.24$. It has a projected separation from nearby M81 satellite BK5N of only 5 kpc. As this is well within BK5N's virial radius, we speculate that d1005+68 may be a satellite of BK5N. If confirmed, this would make d1005+68 one of the first detected satellites-of-a-satellite.

2.2 Introduction

The past decade has seen an awakening in the field of dwarf galaxy discovery. Large photometric surveys such as the Sloan Digital Sky Survey (SDSS), the Panoramic Survey Telescope Rapid Response System (Pan-STARRS), and the Dark Energy Survey (DES) have permitted the discovery of >30 faint and ultrafaint dwarf galaxy (UFD) candidates in the Local Group (e.g., *Belokurov et al.*, 2006; *Martin et al.*, 2013; *Drlica-Wagner et al.*, 2016; *Homma et al.*, 2016). These discoveries have informed the nearly two-decade-old "missing satellites problem" (hereafter MSP; *Klypin et al.* 1999). This apparent tension between the low-end halo mass function slope, predicted by ΛCDM, and the considerably flatter slope of the Milky Way dwarf galaxy luminosity function is a sensitive probe of dark matter properties and galaxy formation in the lowest-mass dark matter halos (e.g., *Macciò et al.*, 2010; *Brooks et al.*, 2013). Yet, with improved understanding, new puzzles have emerged. An apparent dearth of luminous high-velocity subhalos – the "too big to fail" problem (hereafter TBTF; *Boylan-Kolchin et al.* 2011) — is an extension of MSP that is not alleviated by the discovery of UFDs (see *Simon and Geha* 2007, *Macciò et al.* 2010, *Font et al.* 2011, and *Brooks et al.* 2013 for discussion of possible solutions to MSP and TBTF). Furthermore, mounting evidence suggests that both the Milky Way's and M31's satellites form potentially planar structures (*Pawlowski et al.*, 2013). Though ΛCDM predicts anisotropic accretion due to infall along cosmic filaments (e.g., *Li and Helmi* 2008), potentially resulting in planar satellite distributions (*Sawala et al.*, 2016), the thinness of the Local Group planes remains difficult to replicate.

ΛCDM predicts that all galaxy halos host subhalos, the most massive of which will host luminous satellites. Consequently, many of the satellites around Milky Way–mass galaxies also likely possess, or possessed before infall, their own orbiting subhalos. These "satellites-of-satellites" are difficult to detect, owing to their intrinsic faintness. Recent work suggests that several of the Milky Way satellites nearest to

the Magellanic Clouds may be satellites of the Clouds themselves (*Drlica-Wagner et al.*, 2016), with possibly $> 30\%$ of Milky Way satellites originating around the Large Magellanic Cloud (LMC; *Jethwa et al.*, 2016).

It is clear that our understanding of dwarf galaxy populations in the ΛCDM paradigm is currently limited. A key hurdle is that our understanding of dwarf galaxy luminosity functions, spatial distributions, and properties is almost entirely confined to the Local Group. Characterization of satellite populations around other Local Group analogs is crucial if we are to obtain a complete description of low-mass galaxy formation.

Propelled by the advent of wide-field imagers on large telescopes, discovery and characterization of faint 'classical dwarfs' ($M_V < -10$) has become possible in nearby galaxy groups and clusters using large area (approaching 100 deg^2) diffuse light surveys (e.g., *Chiboucas et al.*, 2009; *Müller et al.*, 2015a; *Muñoz et al.*, 2015; *Ferrarese et al.*, 2016). Observationally expensive, smaller area deep surveys of resolved stellar populations in nearby galaxy groups are bringing even fainter dwarf galaxies within reach (e.g., *Sand et al.*, 2015; *Carlin et al.*, 2016; *Crnojević et al.*, 2016; *Toloba et al.*, 2016).

In this Letter, we present the discovery of a faint dwarf spheroidal galaxy in the M81 group, d1005+68 (following the naming convention of *Chiboucas et al.* 2013), detected as an overdensity of stars in observations taken with the Subaru Hyper Suprime-Cam. At $M_V = -7.9$ (see § 2.4), d1005+68 is one of the faintest confirmed galaxies discovered outside of the Local Group.

2.3 Detection

We use observations taken with the Subaru Hyper Suprime-Cam (HSC; *Miyazaki et al.* 2012) through NOAO Gemini-Subaru exchange time (PI: Bell, 2015A-0281).

Table 2.1. d1005+68 Parameters

Parameter	Value
α (J2000)	$10^h05^m31\overset{s}{.}82 \pm 1\overset{s}{.}1$
δ (J2000)	$+68°14'19\overset{''}{.}56 \pm 5\overset{''}{.}95$
$D_{\rm TRGB}$	$3.98^{+0.39}_{-0.43}$ Mpc
M_V [a]	$-7.94^{+0.38}_{-0.50}$
r_h	$9\overset{''}{.}7 \pm 2\overset{''}{.}0$
r_h	188^{+39}_{-41} pc
$\log_{10}(M_*/M_\odot)$ [b]	$5.40^{+0.22}_{-0.16}$
[Fe/H] [c]	-1.90 ± 0.24

Note. — [a] Isochrone fitting, assuming $D_{\rm TRGB}$. [b] Current stellar mass, assuming 40% mass loss. [c] Metallicity of best-fit isochrone, assuming $[\alpha/{\rm Fe}] = 0.25$.

The observations consist of two pointings for a survey footprint area of ~ 3.5 deg^2, in three filters: g, r, and i, with ~ 3600 s per filter per pointing. The data were reduced using the HSC pipeline (*Bosch et al.*, 2018), which was developed from the LSST Pipeline (*Axelrod et al.*, 2010). The data were calibrated using photometry and astrometry from Pan-STARRS1 (*Magnier et al.*, 2013). An aggressive background subtraction using a 32 pixel region for determining the background was used. Objects are detected in i band and forced photometry is performed in g and r. The average FWHM in M81 Field 2 (in which d1005+68 was discovered) is $\sim 0\overset{''}{.}7$ in all bands, giving limiting 5σ point-source magnitudes of $g \sim 27$, $r \sim 26.5$, and $i \sim 26$. All magnitudes use the SDSS photometric system, corrected for foreground Galactic extinction using the *Schlegel et al.* (1998) maps as calibrated by *Schlafly and Finkbeiner* (2011b).

As the dwarf galaxies of interest are low surface brightness and possess little diffuse emission, we detect dwarf candidates by resolving them into individual stars. At the distance of M81 (3.6 Mpc; *Radburn-Smith et al.* 2011), only stars in the top $\sim$25%, or tip of the RGB (TRGB), are visible. TRGB stars are relatively numerous, and as they trace the old stellar population of galaxies, their number can be scaled to a total

luminosity with modest uncertainty (*Harmsen et al.*, 2017).

At our survey depths, contaminants – high-redshift background galaxies – dominate. The majority of these galaxy contaminants must be removed in order to reach the surface brightness sensitivity necessary to detect faint dwarf satellites ($\mu_V \lesssim 28$ mag arcsec^2). We reject galaxies using a combined morphology and color cut; such a process sacrifices completeness in order to dramatically suppress contamination (this will be revisited in § 2.4). To be defined as a star, a source must satisfy two criteria: (1) FWHM $\leqslant 0.6''$ across all three bands (we will consider less stringent cuts later), and (2) consistent with the $g-r$ vs. $r-i$ stellar locus within σ_{g-r} (the photometric uncertainty) + 0.2 mag (intrinsic scatter; *High et al.* 2009). Next, we locate stars on the RGB from the $g-r$ vs. r color-magnitude diagram (CMD) and divide them into three metallicity bins using simple polygonal boundaries (see Figure 2.1).

d1005+68 stands out as a significant overdensity of metal-poor stars in the sparse, metallicity-binned RGB star map of M81's stellar halo (Figure 2.1), with nine RGB stars visible in a $1' \times 1'$ region centered on d1005+68. To quantify the prominence of this overdensity against the surrounding diffuse stellar halo, we extract 500 $1' \times 1'$ (independent) regions from a 0.14 deg^2 region south of d1005+68, away from the stellar debris associated with the tidal disruption of NGC 3077. We compute the discrete probability distribution of the number of RGB stars returned in each region and fit it to a Poisson distribution, $p(N|\lambda)$. From the best-fit Poisson distribution, we take a mean background of $\lambda = 0.38 \pm 0.03$ RGB stars arcmin^{-2}. Integrating over the best-fit distribution, and correcting for the number of independent 1 arcmin^2 regions (10^4) in the target footprint, we obtain a cumulative probability of drawing nine RGB stars arcmin^{-2} of $4.2 \times 10^{-6} \pm 3.5 \times 10^{-6}$. Placed into terms of standard error, this is a $4.5 - 5\sigma$ detection. Thus, we expect to detect 0.01 such random overdensities in our target footprint. In the following section, we discuss the derivation of d1005+68's

properties, which are summarized in Table 2.1. Its position relative to other M81 Group members is shown in the map of M81's stellar halo in Figure 2.1. In Figure 2.2 we show the i-band image of d1005+68 with detected RGB stars encircled, as well as the curve of growth.

2.4 Properties

The $g-i$ vs. i CMD of probable member stars of d1005+68 are shown in Figure 2.3. We define membership based on the shape of the curve of growth (Figure 2.2, bottom right panel), where the background-subtracted profile asymptotes to a ∼constant value. In contrast to the stringent cut used for detection of the dwarf, we use broader criteria for membership determination and the derivation of the dwarf's properties. At low signal-to-noise, the measured sizes of objects are subject to significant scatter, causing tight tolerances on size to reject many true stars. Consequently, the stars shown on the CMD were chosen using the same color constraint as for detection, but with a looser size constraint – FWHM in x and $y \leqslant 0\farcs84$. Also shown in Figure 2.3 are CMDs of nearby (in projection) dwarf galaxy BK5N – both full and randomly down-sampled to the number of observed stars in d1005+68.

The centroid, half-light radius, and number of member stars (and therefore luminosity) are the averages of a range of values estimated by varying the size cut between $0\farcs6$ and $1\farcs34$, the number of stars used to define the position of the center (relative to the optical center) between 5 and 12, and the Poisson background value (see § 2.3). For each iteration, the number of member stars are determined using the turnover of the background-subtracted curve of growth, from which the half-light radius is also derived. The mean values of the centroid and half-light radius can be found in Table 2.1, along with the standard deviations of the various iterations.

The TRGB can be used as a robust distance estimator, due to its near-constant luminosity ($M_I = -4.04$ in the Johnson-Cousins system) at low metallicities (*Bellazzini*

et al., 2001). The TRGB for d1005+68's CMD (see Figure 2.3) was calculated as in *Monachesi et al.* (2016a), but also includes the completeness in the model luminosity function (LF), ϕ (see below), as in *Makarov et al.* (2006):

$$\phi(m|\mathbf{x}) = \int \psi(m'|\mathbf{x})\, e(m|m')\, \rho(m')\, dm' \tag{2.1}$$

where ψ is the true LF, e is the Gaussian error kernel, ρ is the completeness, and $\mathbf{x}$ is the vector of model parameters that we fit. See Appendix C of *Monachesi et al.* (2016a) for details. The completeness was tabulated in 0.3 mag i-band bins using the area in common with GHOSTS and smoothed with a three-bin boxcar (the smoothing has no effect on the derived TRGB magnitudes). We find a TRGB of $i_{TRGB} = 24.48^{+0.17}_{-0.26}$. Using a SDSS "Lupton prescription," [1], in the JC system, this corresponds to $I_{TRGB} = 23.96^{+0.20}_{-0.25}$, or a distance modulus of $m - M = 28.00^{+0.20}_{-0.25}$. Thus, we derive a distance to d1005+68 of $3.98^{+0.39}_{-0.43}$ Mpc.

d1005+68's luminosity was estimated using the number of stars visible to a certain i-band "depth" below the TRGB. To convert the number of observed stars to a total number of stars above this i-band limit, we use the GHOSTS fields for M81 (*Radburn-Smith et al.*, 2011) to compute the stellar completeness in the Subaru field, as a function of i-band magnitude, for our three size cuts (0.″6, 0.″84, 1.″34). For all three size cuts, we estimate a total number of 32 ± 6 RGB stars to a depth of $\sim$1.2 mag below the TRGB, and 25 ± 4 to a depth of $\sim$1.1 mag below the TRGB. We then randomly sample our best-fit isochrone in that magnitude range given a *Chabrier* (2003) stellar initial mass function (IMF). We record the resulting number of RGB stars drawn at each stellar mass and compute a probability distribution of drawing the observed number of stars at each mass, at the given RGB depth. We obtain a most probable initial mass of $\log_{10}(M_*/M_\odot) = 5.62$, which, after the standard 40% mass-loss correction (*Bruzual and Charlot*, 2003), corresponds to a current stellar

[1] https://www.sdss3.org/dr8/algorithms/sdssUBVRITransform.php

mass of $\log_{10}(M_*/M_\odot) = 5.40$ or $M_* = 2.5 \times 10^5 M_\odot$. We then convert the stellar mass distribution to a V-band luminosity, while randomly varying the number of stars in each isochrone, at a fixed stellar mass. Accounting for the variance in the different depths considered, as well as sampling variance along the IMF, we obtain a V-band luminosity of $M_V = -7.94^{+0.38}_{-0.50}$. The primary uncertainties on this estimate come from our TRGB distance range and the width of the best-fit stellar mass distribution.

To estimate the metallicity, we fit a suite of PARSEC stellar isochrone models (*Bressan et al.*, 2012) with a fixed 12 Gyr age, from $Z = 0.0001 - 0.001$. The best-fit isochrone, for the $g - i$ vs. i CMD, corresponds to a metallicity of $Z = 0.0004$. Assuming $[\alpha/\mathrm{Fe}] = 0.25$, this corresponds to $[\mathrm{Fe/H}] = -1.90$. For each iteration in the centroid calculation (above) we draw 10 bootstrap samples and compute the best-fit isochrone for each case. We then combine the standard deviation of the resulting distribution with the TRGB distance uncertainties. We obtain a final metallicity estimate of $[\mathrm{Fe/H}] = -1.90 \pm 0.24$.

d1005+68 has a projected separation from M81 of 1.°22, or, using the distance to M81, 76.4 kpc. Using the adopted TRGB distance to d1005+68 of $3.98^{+0.39}_{-0.43}$ Mpc, this corresponds to a large range in possible 3D distances. The projected physical separation between d1005+68 and the nearby (on the sky) dwarf spheroidal BK5N is only $\sim$ 5 kpc at the distance of BK5N (3.78 Mpc; *Karachentsev et al.* 2000). Assuming a stellar mass for BK5N of $\sim 10^7 M_\odot$ ($M_V = -11.33$; *Caldwell et al.* 1998) and extrapolating from the stellar mass–halo mass relation of *Behroozi et al.* (2013), the virial radius of BK5N is likely $\sim$ 40 kpc. Therefore, were d1005+68 at a similar distance as BK5N, it would be well within BK5N's virial radius. In support of this, the CMD of d1005+68 is well approximated by a random sampling of BK5N's CMD, as in Figure 2.3. However, the 3D separation could be much higher when factoring in the uncertainty in d1005+68's TRGB distance.

2.5 Discussion and Closing Remarks

In this Letter, we presented a new faint dwarf galaxy, d1005+68, with properties consistent with being a satellite of the M81 Group. It was detected as a 5σ overdensity in our 3.5 deg^2 Subaru Hyper Suprime-Cam survey of M81's resolved stellar halo. We find that the CMD is best fit by an isochrone of age 12 Gyr and metallicity [Fe/H] $= -1.90 \pm 0.24$. d1005+68 has projected physical distances from M81, NGC 3077, and BK5N of $\sim$76 kpc, 40 kpc, and 5 kpc, respectively. The estimated heliocentric TRGB distance of $3.98^{+0.39}_{-0.43}$ Mpc provides strong evidence for group membership; however, the high uncertainties prohibit accurate estimates of 3D separation from other group members. Its current stellar mass, determined from isochrone fitting, is $M_* = 2.5^{+1.7}_{-0.8} \times 10^5 M_\odot$, corresponding to an absolute V-band magnitude of $M_V = -7.94^{+0.38}_{-0.50}$.

Figure 2.4 shows d1005+68 in context of Local Group and M81 Group members. d1005+68 is among the faintest confirmed galaxies discovered outside of the Local Group – similar in brightness to M81 group member d0944+69 (*Chiboucas et al.* 2013; $M_V = -8.05$ with no claimed uncertainty), NGC 2403 member MADCASH J074238+652501-dw (*Carlin et al.* 2016; $M_V = -7.7 \pm 0.7$), Centaurus group member Dw5 (*Crnojević et al.* 2016; $M_V = -7.2 \pm 1.0$), and Fornax cluster member Fornax UFD1 (*Lee et al.* 2017; $M_V = -7.6 \pm 0.2$) – and probes the very faintest end of the known M81 satellite luminosity function.

The projected separation between d1005+68 and BK5N of 5 kpc is well within the estimated virial radius of BK5N ($\sim$ 40 kpc). With our highly uncertain TRGB distance (due to scarcity of stars) and the similarity between the two CMDs (Figure 2.3), this introduces the *possibility* that d1005+68 is a satellite of BK5N. If confirmed (via more accurate distance estimates and line of sight velocity information), this would make it the first satellite-of-a-satellite discovered outside of the Local Group.

Acknowledgements

This material is based upon work supported by the National Science Foundation Graduate Research Fellowship Program under grant No. DGE 1256260. Any opinions, findings, and conclusions or recommendations expressed in this material are those of the author(s) and do not necessarily reflect the views of the National Science Foundation.

Based on observations obtained at the Subaru Observatory, which is operated by the National Astronomical Observatory of Japan, via the Gemini/Subaru Time Exchange Program. We thank the Subaru support staff – particularly Akito Tajitsu, Tsuyoshi Terai, Dan Birchall, and Fumiaki Nakata – for invaluable help preparing and carrying out the observing run.

The Pan-STARRS1 Surveys (PS1) have been made possible through contributions of the Institute for Astronomy, the University of Hawaii, the Pan-STARRS Project Office, the Max-Planck Society and its participating institutes, the Max Planck Institute for Astronomy, Heidelberg and the Max Planck Institute for Extraterrestrial Physics, Garching, The Johns Hopkins University, Durham University, the University of Edinburgh, Queen's University Belfast, the Harvard-Smithsonian Center for Astrophysics, the Las Cumbres Observatory Global Telescope Network Incorporated, the National Central University of Taiwan, the Space Telescope Science Institute, the National Aeronautics and Space Administration under grant No. NNX08AR22G issued through the Planetary Science Division of the NASA Science Mission Directorate, the National Science Foundation under grant No. AST-1238877, the University of Maryland, and Eotvos Lorand University (ELTE).

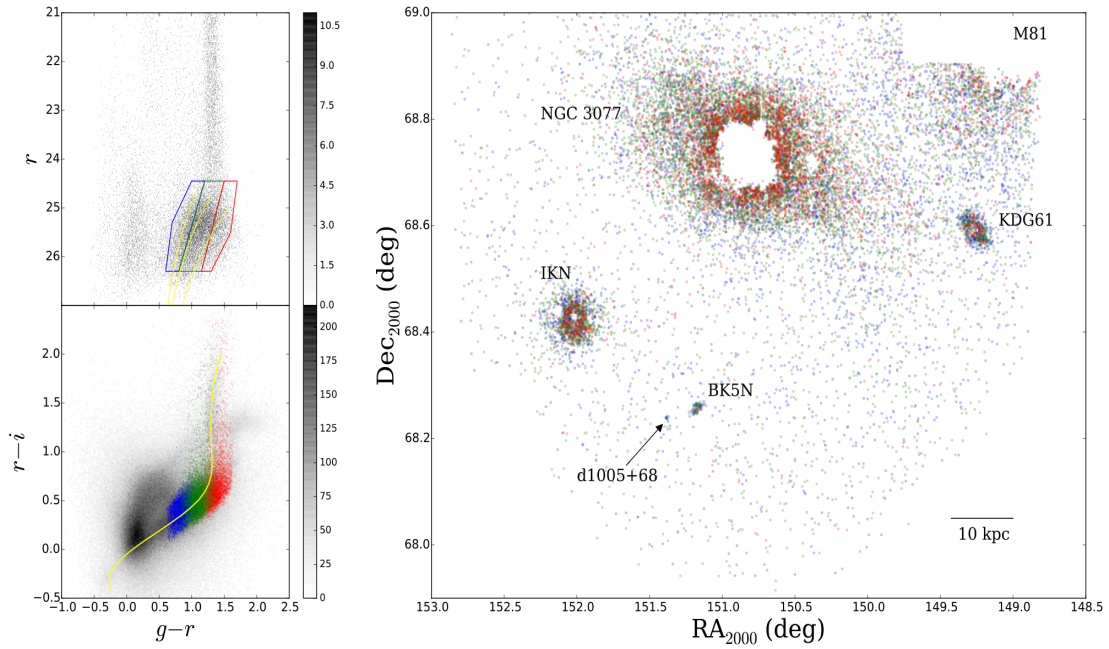

Figure 2.1: Top left: the $g-r$ vs. r CMD (de-reddened) of all stars (see § 2.3) in the Subaru field, separated into ∼0.01 mag bins. The RGB is encapsulated within the drawn polygon, which has been divided into three metallicity bins by eye, blue being the most metal-poor. The blue locus is likely a combination of young Helium burners and unresolved high-redshift background galaxies. The stripe at bright magnitudes is composed of Milky Way foreground stars. The yellow lines are 12 Gyr PARSEC isochrones (*Bressan et al.*, 2012), with [Fe/H] = −2.1 (left), [Fe/H] = −1.7 (center), and [Fe/H] = −1.2 (right), shown here for reference. Bottom left: the $g-r$ vs. $r-i$ color-color diagram of photometrically identified sources. The stellar locus (*High et al.*, 2009) is shown as a yellow curve. RGB stars defined by our morphological, CMD, and stellar locus criteria (§ 2.3) are shown as either blue, green, or red points, corresponding to their metallicity bin. The darkest region is the galaxy locus. Right: a cutout of the map of M81's stellar halo in resolved RGB stars (*Smercina et al.*, 2019). The colors correspond to the metallicity bins defined on the CMD in the top left figure. The known galaxies in the field are labeled. d1005+68 is located at the bottom left of the map, indicated by a black arrow. It appears as a significant overdensity of blue (metal-poor) RGB stars, very near to the dwarf spheroidal, BK5N.

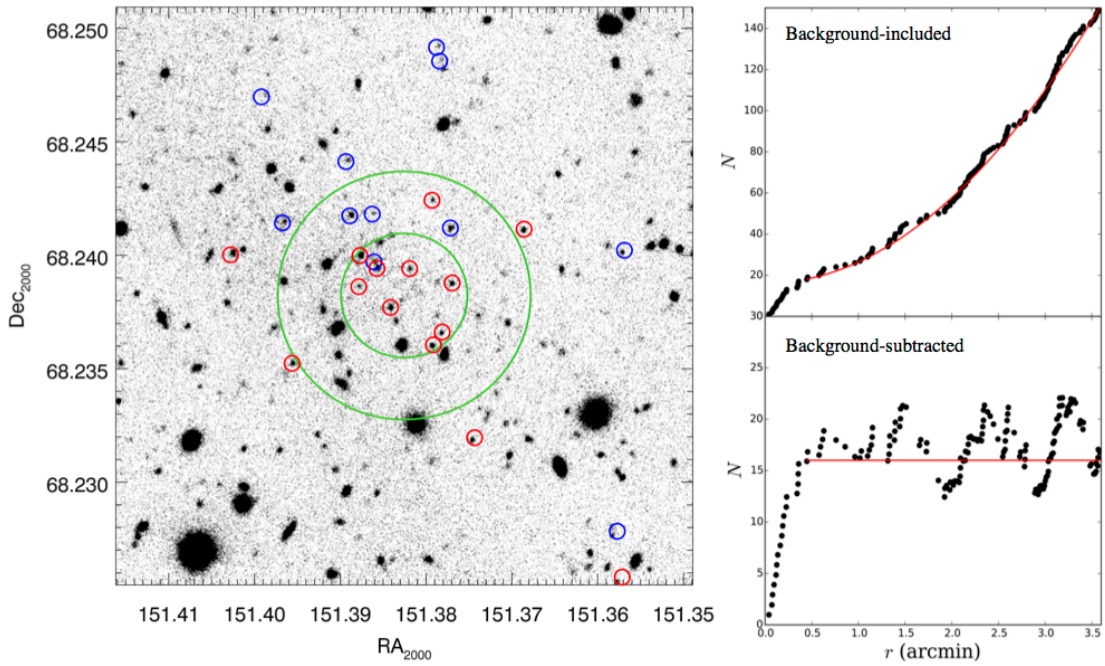

Figure 2.2: Left: the HSC i-band image of d1005+68. The concentric green circles correspond to apertures with 1 and 2× the derived half-light radius, centered on the estimated centroid. Member stars are encircled, with stars passing the 0.″84 size cut shown in red and those passing the broader 1.″34 size cut in blue (see § 2.4). Top right: the curve of growth for d1005+68, using RGB stars defined by the 1.″34 size cut (the union of the blue and red stars). The red curve corresponds to an $N = \Sigma_{BG} r^2$ model of the background, using the derived Poisson mean with a 10% correction ($\Sigma_{BG} \sim$ 3.3 RGB stars arcmin^{-2}). Bottom right: the background-subtracted curve of growth. The red line denotes the median value of $N - \Sigma_{BG} \pi r^2$, which we take as the number of member stars. The "sawtooth" nature of the radial profile is simply due to random over- and underdensities in the halo.

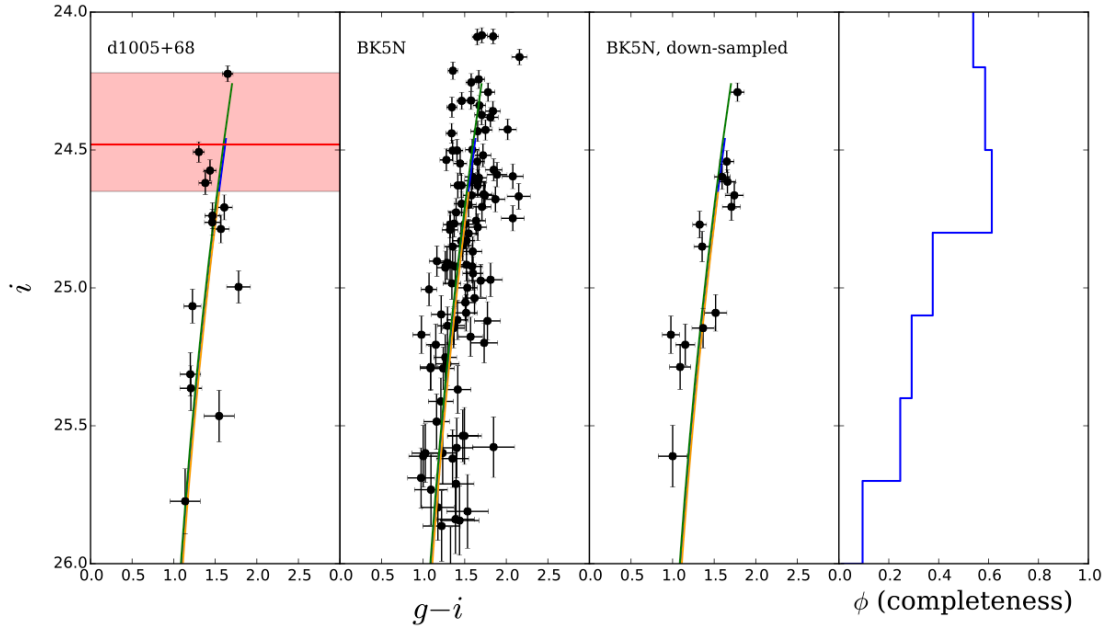

Figure 2.3: Left: the color-magnitude diagram of d1005+68. Stars shown are identified with the 0.″84 size cut (see § 2.4), extending to ∼0.′5 or ∼$3r_h$. The TRGB is shown as a red line, with the 90% confidence shown as the red shaded region. The three blue curves on each diagram correspond to the best-fit 12 Gyr isochrones at each distance bound, with respective metallicities (from left to right) of [Fe/H] = −1.76 (green), −1.90 (blue), and −2.02 (orange). Center left: The CMD of BK5N in RGB stars, with ∼ 100 detected RGB stars. Center right: BK5N's CMD, randomly down-sampled to match the number of member stars in d1005+68. Right: the i-band completeness function, ϕ.

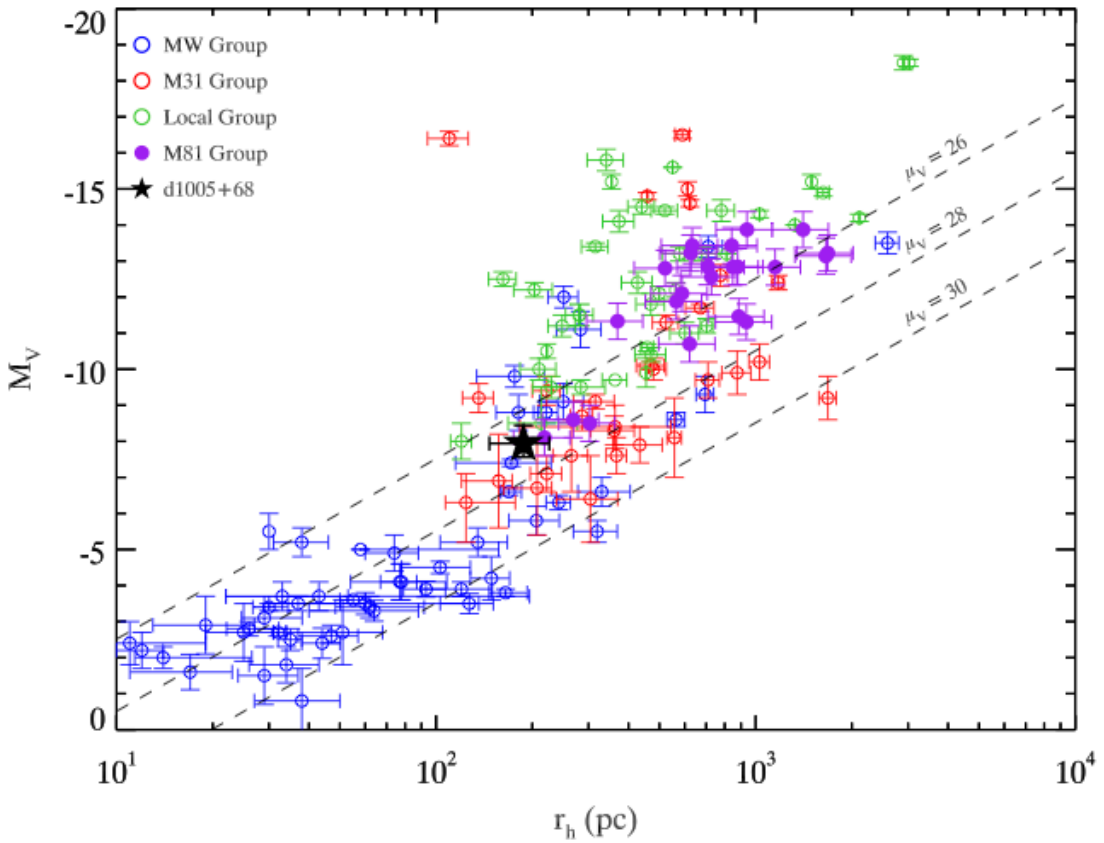

Figure 2.4: Half-light radius–luminosity diagram for Milky Way, M31, Local Group, and M81 Group satellites. Milky Way satellites are shown as blue circles, M31 satellites as red circles, general Local Group members (outside the virial radius of MW or M31) as green circles, and M81 members as filled purple circles. Local Group data are compiled from the catalog of *McConnachie* (2012), from the recent slew of Dark Energy Survey (*Bechtol et al.*, 2015; *Drlica-Wagner et al.*, 2015; *Koposov et al.*, 2015) and Pan-STARRS (*Laevens et al.*, 2015) discoveries, and from other isolated discoveries (*Belokurov et al.*, 2014; *Kim et al.*, 2015; *Homma et al.*, 2016). M81 Group data are compiled from *Karachentsev et al.* (2000), *Lianou et al.* (2010), and *Chiboucas et al.* (2013). In the absence of M_V and r_h uncertainties in the literature, typical Local Group uncertainties of 20% have been adopted for M81 members. d1005+68 is shown as a black star. Lines of constant surface brightness are shown for reference. Our derived r_h and M_V for d1005+68 place it well within the locus of Local Group satellites, while it is one of the faintest members of the M81 Group.

CHAPTER III

A Lonely Giant: The Sparse Satellite Population of M94 Challenges Galaxy Formation

3.1 Abstract

The dwarf satellites of 'giant' Milky Way (MW)-mass galaxies are our primary probes of low-mass dark matter halos. The number and velocities of the satellite galaxies of the MW and M31 initially puzzled galaxy formation theorists, but are now reproduced well by many models. Yet, are the MW's and M31's satellites representative? Were galaxy formation models 'overfit'? These questions motivate deep searches for satellite galaxies outside the Local Group. We present a deep survey of the 'classical' satellites ($M_\star \geqslant 4\times10^5 M_\odot$) of the MW-mass galaxy M94 out to 150 kpc projected distance. We find *only two* satellites, each with $M_\star \sim 10^6 M_\odot$, compared with 6–12 such satellites in the four other MW-mass systems with comparable data (MW, M31, M81, M101). Using a 'standard' prescription for occupying dark matter halos (taken from the fully hydrodynamical EAGLE simulation) with galaxies, we find that such a sparse satellite population occurs in $< 0.2\%$ of MW-mass systems — a $< 1\%$ probability among a sample of five (known systems + M94). In order to produce an M94-like system more frequently we assume satellite galaxy formation is much more stochastic than is currently predicted, by dramatically increasing the slope and

scatter of the stellar mass–halo mass (SMHM) relation. Surprisingly, the SMHM relation must be altered even for halos masses up to $10^{11} M_{\odot}$ — significantly above the mass scales predicted to have increased scatter from current hydrodynamical models. The sparse satellite population of this 'lonely giant' thus advocates for an important modification to ideas of how the satellites around MW-mass galaxies form.

3.2 Introduction

While the Λ-Cold Dark Matter (ΛCDM) paradigm successfully explains the large-scale properties of the Universe, many of its predictions on small scales appear to be in tension with the number and properties of dwarf galaxies (see the review by *Bullock and Boylan-Kolchin*, 2017). While the Milky Way (MW) hosts ∼10 'classical' dwarf satellite galaxies with velocity scales of $\gtrsim$10 km s^{-1} (see *McConnachie* 2012), dramatically more DM halos were predicted to exist at those scales — the 'Missing Satellites Problem' (MSP; *Klypin et al.* 1999; *Moore et al.* 1999). Later work appeared to sharpen the problem by suggesting that the velocities of the few satellites the MW does have are substantially lower than the velocity scales of the most massive predicted dark matter (DM) halos — the 'Too Big to Fail' problem (TBTF; *Boylan-Kolchin et al.* 2011).

While it is possible that these observations may signal the need for an important modification to ΛCDM, it is widely accepted that improved galaxy formation physics is the likely resolution to these problems. Feedback from supernovae is predicted to dramatically suppress the number of stars in even relatively massive DM halos ($M_h \sim 10^{10} M_{\odot}$) (*Macciò et al.*, 2010; *Font et al.*, 2011). Furthermore, supernovae-driven outflows can drag DM to larger radii and could reduce the central velocities of these halos to observed values (*Brooks et al.*, 2013; *Wetzel et al.*, 2016). Recently, it has been suggested that tidal disruption of satellites and their subhalos around massive galaxies like the Milky Way reduces the number of predicted satellites further (e.g.,

Garrison-Kimmel et al., 2017b). These models, along with more a more complete census of MW satellites from surveys such as SDSS and DES, have been so successful that it has been argued 'there is no missing satellites problem' (*Kim et al.*, 2017).

Nearly all of our understanding of the small-scale challenges to ΛCDM has been based on observations of satellites in the Local Group (LG), prompting important questions:

1. Are the LG's satellites representative?

2. Are galaxy formation models in turn representative, or have they instead been over-tailored to fit the LG's satellites?

These questions motivate a deep census of the satellites of 'giant' MW-mass galaxies and low-mass field dwarf galaxies. A variety of approaches are being taken: deep spectroscopic surveys (e.g., *Spencer et al.*, 2014; *Geha et al.*, 2017), field H I observations (*Papastergis et al.*, 2015; *Yaryura et al.*, 2016), large-area integrated light surveys around nearby galaxies (e.g., *Chiboucas et al.*, 2009; *Müller et al.*, 2015b; *Danieli et al.*, 2017), and narrower and deeper surveys which allow satellites to be resolved into stars (e.g., *Toloba et al.*, 2016; *Carlin et al.*, 2016; *Crnojević et al.*, 2016; *Smercina et al.*, 2017). Discovering and confirming a complete sample of even 'classical' satellites around nearby galaxies requires a formidable combination of depth and area. Such a sample exists for only four MW-like systems: the MW and M31 (*McConnachie*, 2012), M81 (*Karachentsev and Kudrya*, 2014), and M101 (*Danieli et al.*, 2017).

In this paper we present the discovery of two low-mass satellites of the nearby MW-mass galaxy M94 (NGC 4736; $M_\star \simeq 4{\times}10^{10} M_\odot$, *Karachentsev et al.* 2013; $D = 4.2\,\mathrm{Mpc}$, *Radburn-Smith et al.* 2011), detected in a deep Hyper Suprime-Cam (HSC) survey with an effective radius of 150 kpc. Rather than discovering the ∼10 'classical' satellites which were expected by scaling the other MW-mass systems, *we discovered*

only two, both with stellar masses only $\lesssim 10^6 M_\odot$ — a satellite population completely unlike any other known galaxy. We further show that, more than being unexpected, M94's satellite population cannot be explained using 'standard' galaxy formation models — directly advocating for significant modifications to the physics of low-mass halo occupation.

3.3 Observations

Our HSC survey, carried out through the NOAO Gemini–Subaru exchange program (PI: Smercina, NOAO 2017A-0312), consists of six HSC pointings in g-band (for satellite discovery), three in i, and two in r (for stellar halo characterization). The deepest two fields were observed for ∼7200s per filter in gri. The remaining four fields were observed for 1200s per filter. The average seeing FWHM in g-band is $\sim 0\farcs8$ for all fields. The g-band survey footprint is symmetric around M94 and has an area equal to a 150 kpc radius circular region, giving an 'effective' radius of 150 kpc (see Fig. 3.1).

The data were reduced as described in *Smercina et al.* (2017), using the updated HSC pipeline (*Bosch et al.*, 2018). Data were calibrated using the Pan-STARRS1 survey (*Magnier et al.*, 2013), but all magnitudes are in the SDSS photometric system and have been corrected for foreground Galactic extinction using the updated *Schlafly and Finkbeiner* (2011b) corrections.

The satellite-focused part of the survey consists of six fields with moderately deep to very deep g-band data. These six fields were visually inspected for low surface brightness (SB) candidate dwarf galaxies with resolved or semi-resolved stars with luminosities and half-light radii similar to Local Group satellites following *Chiboucas et al.* (2009) — only two were found. One of these dwarfs, M94-Dw1, was detected as a dwarf galaxy candidate (dw1255+40) in the integrated light survey of *Müller et al.* (2017). The locations and properties of these dwarfs are given in Figure 3.1

and Table 3.1.

3.3.1 Completeness

In order to understand our satellite detection completeness limits we conducted ∼500 individual artificial galaxy tests in the g-band data. Satellites were inserted with a range of projected distances to M94 of $15 < D/kpc < 150$. Tests were done by eye on isolated images to eliminate subconscious cross-referencing with known areas in the field, and with multiple authors to produce independently verifiable results. Dwarf galaxies were simulated by sampling random stars from a 12 Gyr isochrone and injecting them into the survey images. These artificial galaxies were created from single stellar populations and thus resemble quiescent satellites in the LG. The positions of stars were drawn randomly from independent Gaussian profiles in X and Y, with randomly-generated galaxy centers, elliptical half-light radii ranging from 0.1–1 kpc, and corresponding ellipticities $\epsilon \leqslant 0.9$. Position angles were also chosen at random, ranging from 0°–360°. Additionally, in a given test there was a 30% chance of not injecting an artificial galaxy.

Most effort was spent sampling galaxies with luminosities $-9.1 > M_V > -10.3$, spanning the range of the two candidates — constituting 300 tests. We conducted an additional 140 tests in the luminosity range $-10.3 > M_V > -12.3$. As further explained in § 3.5, we account for up to 1 Mpc uncertainty in line-of-sight (LOS) distance between satellites and the central galaxy (M94 in this case). LOS distance variance only significantly affects the luminosity of satellites at the distance of M94 when it exceeds 0.4 Mpc (∼0.2 mag). From simulations (see § 3.5), the distribution of satellite LOS distances from MW-mass galaxies is well-fit by a Lorentzian distribution — the large-distance wings stemming from the two-point correlation function of galaxies. We estimate that ∼10% of apparent satellites around MW-mass galaxies likely have $\Delta\, d = \pm 0.4$–1 Mpc. To explore this effect on our test results, 30 additional tests were

conducted, focused on satellites in the $-9.1 > M_V > -10.3$ luminosity range ($\sim$10% of our original 300 tests in that luminosity range), and placed at varying distances, drawn from a Lorentzian distribution with $\Delta\, d = \pm 0.4$–$1\,\mathrm{Mpc}$.

Figure 3.2 shows the results of our tests, with three example artificial satellites. Overall completeness was high, with >70% of all injected satellites recovered. The rate of false detection was *very* low (2%) and only occurred in the very lowest-surface brightness ($\mu_V \lesssim 28\,\mathrm{mag\,arcsec^{-2}}$) cases. Completeness is a relatively smooth function of SB (middle panel), with $\sim$80% completeness corresponding to a SB of $\mu_V = 27\,\mathrm{mag\,arcsec^{-2}}$. Overall completeness is $\sim$10% higher on average in the two deeper fields, but otherwise there is little dependence on field location, even when binning by SB. The lower left panel shows the completeness binned as a function of luminosity and half-light radius, along with the LG satellites with luminosities approximately within our test range. Applied to the properties of LG satellites, we estimate an average completeness of 85% in the range $-9.1 > M_V > -10.3$. Our satellite tests in the range $-10.3 > M_V > -12.3$ yield a very high 97% average completeness, and is $\sim$100% when applied to LG satellites. The effect of LOS distance variance was negligible, following our 30 additional tests. Average completeness remained the same, likely owing to the competing effects of lower completeness at farther LOS distances and proportionally higher completeness at closer distances.

Scaling from the mass-to-light ratios of LG satellites (*McConnachie*, 2012), our 85% completeness limit of $M_V = -9.1$ corresponds to $M_\star \sim 4\times10^5 M_\odot$. Consequently, M94, a MW-mass galaxy, very likely hosts only two satellite galaxies with projected radii $< 150\,\mathrm{kpc}$ and $M_\star \gtrsim 4\times10^5 M_\odot$ — a satellite population unlike any other known galaxy of its kind.

Table 3.1. Dwarf Parameters

Parameter	M94-Dw1	M94-Dw2
α (J2000)	$12^h55^m02\overset{s}{.}49$	$12^h51^m04\overset{s}{.}4$
δ (J2000)	$40°35'21\overset{''}{.}9$	$41°38'09\overset{''}{.}9$
$D_{\rm TRGB}$	4.1 ± 0.2 Mpc	$4.7^{+0.2}_{-0.4}$ Mpc
M_V [a]	-10.1 ± 0.1	$-9.7^{-0.1}_{+0.2}$
r_h	618 ± 90 pc	316 ± 40 pc
$\mu_{V,eff}$ [b]	27.4 mag arcsec $^{-2}$	26.4 mag arcsec $^{-2}$
$M_\star$ [c]	$9.7\times10^5 M_\odot$	$6.7\times10^5 M_\odot$
[Fe/H] [d]	-2.1 ± 0.1	-2.1 ± 0.1

Note. — [a] Profile fitting, assuming $D_{\rm TRGB}$. [b] Effective V-band surface brightness within the half-light radius. [c] Comparing to dwarf irregulars of similar luminosity in the Local Group (*McConnachie*, 2012). [d] Metallicity of best-fit isochrone, assuming [α/Fe] = 0.25.

3.4 Satellite Properties

The two dwarfs were detected in the two fields with *gri* imaging, allowing for analysis of their stellar populations. In Figure 3.1 we show the r-band images and color–magnitude diagrams (CMDs) of the dwarfs. Aperture photometry using successive elliptical apertures was used to construct brightness profiles and a total flux for each dwarf. The profiles were also used to determine half-light radii. g and r-band magnitudes were converted to V-band using the SDSS 'Lupton 2005' photometric transformation[1].

Distances for the dwarfs were determined from the tip of the red giant branch (TRGB), estimated using a maximum-likelihood analysis following Appendix C of *Monachesi et al.* (2016a) and *Smercina et al.* (2017). We determined r-band completeness using artificial stars for the highly crowded regions of M94-Dw2. Dw1 and Dw2 are 4.1 ± 0.2 Mpc and $4.7^{+0.2}_{-0.4}$ Mpc away, both reasonably consistent with M94

[1] http://www.sdss.org/dr12/algorithms/sdssubvritransform

group membership ($D_{\rm M94}\sim$4.2 Mpc). We thus estimate absolute V-band magnitudes of -10.1 and -9.7, with 0.1–0.2 mag uncertainties dominated by the TRGB distance. Projected distances from M94 are 69 kpc for Dw1 and 38 kpc for Dw2.

Both Dw1 and Dw2 have stars bluer than the RGB with colors typical of young main sequence and intermediate-age core helium-burning stars (*Radburn-Smith et al.*, 2011), indicating ongoing star formation. Furthermore, both dwarfs have irregular morphologies characteristic of star-forming galaxies at similar magnitudes (*Carrillo et al.*, 2017). While isolated dwarf galaxies are invariably star-forming (*Geha et al.*, 2012), the vast majority of LG satellites are quiescent (*Slater and Bell*, 2014) — assumed to be due to ram-pressure stripping during infall (e.g., *Emerick et al.*, 2016; *Simpson et al.*, 2018). Consequently, the star formation in M94's two satellites, with projected distances <100 kpc, is puzzling. If these galaxies are shown to be significantly further from M94, it would make their star formation easier to understand, but would mean that M94 hosts even fewer satellites within its virial radius. Alternatively, this may indicate that M94 lacks the hot gas required to strip gas from satellites (*Slater and Bell*, 2014).

Given Dw1 and Dw2's V-band luminosities and a stellar $M/L_V\sim1$ for similar star-forming dwarf galaxies in the LG (following *McConnachie* 2012), we estimate stellar masses of $9.7\times10^5 M_\odot$ and $6.7\times10^5 M_\odot$.

Metallicities were determined by fitting PARSEC isochrone models (*Bressan et al.*, 2012) to the $g-r$ colors and r-band magnitudes, with a fixed 12 Gyr age and metallicities in the range $Z = 0.0001$–0.001. The best-fit isochrones, placed at the respective TRGB distances for each dwarf, each have metallicity $Z = 0.0002$, corresponding to an iron abundance of [Fe/H] $= -2.1$, assuming an $[\alpha/{\rm Fe}] = 0.25$. This is consistent with the RGB-derived metallicities of similarly-massive star-forming dwarf galaxies in the LG (e.g., Sagittarius dIrr; *McConnachie* 2012).

3.5 Implications for Galaxy Formation

As discussed in § 3.2, the satellite populations of only four other MW-mass galaxies are known down to $< 10^6 M_\odot$ with good completeness: the MW, M31, M81, and M101 — all central galaxies in low-density environments. Among these four, the average number of satellites with $M_\star > 4{\times}10^5 M_\odot$, within a *projected* 150 kpc radius from the central, is 9 ± 3. Projected distances for MW and M31 satellites were determined using the derived physical LG coordinates of *Pawlowski et al.* (2013), and simulating 10,000 random LOS's from external reference positions. All four galaxies also host at least one satellite with $M_\star > 10^9 M_\odot$. Placed in context with these systems, the satellite population of M94, a MW-mass central galaxy in a low-density environment, is completely unexpected — possessing only two 'classical' satellites, with a most massive satellite of only $\sim 10^6 M_\odot$. However, was such a system predictable in simulations?

While a thorough theoretical analysis is beyond the scope of this paper, we explore the implications of our results for galaxy formation models using a simple halo occupation approach. For such an exercise, we require a simulation which a) provides a large diversity of accretion histories for MW-mass halos, b) resolves dark matter subhalos capable of hosting the satellites we are interested in ($M_{\rm h,peak} > 10^9\, M_\odot$), and c) can accurately account for subhalo disruption due to the potential of the central disk (e.g., *Garrison-Kimmel et al.*, 2017b). The current generation of large-volume cosmological hydrodynamical simulations best meet these criteria. Here we use the dark matter subhalos of the large-volume, ($\sim$100 Mpc^3) fully hydrodynamical version of the EAGLE simulation (*Schaye et al.*, 2015). We confirm the robustness of EAGLE's subhalo catalogs at low masses by comparing the average subahlo mass function to a higher-resolution simulation ($\sim$ 25 Mpc^3) also made available by the EAGLE collaboration, finding that they converge for $M_{\rm h,peak} > 10^9\, M_\odot$. This is more than sufficient for our purposes, as most current models predict that cosmic reioniza-

tion and stellar feedback should produce mostly 'dark' halos below $M_{\rm h,peak} < 10^9 M_\odot$ (e.g., *Sawala et al.*, 2015; *Ocvirk et al.*, 2016; *Munshi et al.*, 2017). We choose not to directly use the stellar masses and properties of satellites from EAGLE (see e.g., *Shao et al.* 2018) in this analysis, primarily because we need to explore the impact of varying prescriptions about how satellite galaxies populate dark matter halos.

We assign galaxies to dark matter halos and subhalos using their 'peak' (or infall) mass (denoted as $M_{\rm h,peak}$). Our halo occupation model, which applies equally for both central and satellite galaxies, follows the commonly-adopted *Behroozi et al.* (2013) SMHM relation, with a fixed 0.2 dex log-normal scatter, down to $M_{\rm h,peak} \geqslant 5{\times}10^9 M_\odot$. The SMHM relation at low masses is very uncertain and an extrapolation of the *Behroozi et al.* (2013) SMHM relation over-predicts the number of dwarf satellites of the Milky Way (e.g., *Dooley et al.*, 2017). Consequently, we adopt a somewhat steeper slope with increased mass-dependent scatter for $M_{\rm h,peak} < 5{\times}10^9 M_\odot$, following *Munshi et al.* (2017). Figure 3.3 (left panel) shows the adopted relationship between halo/subhalo mass and galaxy stellar mass for EAGLE dark matter halos.

Next, we define 'MW-mass galaxies' to be central halos with $6{\times}10^{11} M_\odot \leqslant M_{\rm h,peak} \leqslant 3{\times}10^{12} M_\odot$, which host a galaxy with model-derived stellar mass of $M_\star \geqslant 4 \times 10^{10} M_\odot$ — a sample of 1,500 galaxies. As these halos are centrals, they automatically exclude halos in dense environments (cluster members or other satellites), but otherwise span a range of large-scale environments. In turn, we define 'satellites' within a range of projected radii 15 kpc $< D_{proj} <$150 kpc from each EAGLE MW-mass central, and within 1 Mpc in LOS (Z) distance — a realistic observational constraint for satellites around nearby galaxies.

Figure 3.4 (left panel) shows the resulting satellite mass function for MW-mass galaxies in EAGLE, against known satellite mass functions within 150 kpc projected distance from the central. The simulated satellite mass functions have been completeness-corrected to match our results for M94 (see § 3.3.1) — 85% for $4{\times}10^5\ M_\odot < M_* <$

$1.2{\times}10^6\ M_\odot$ ($-9.1 > M_V > -10.3$). The 'standard' halo occupation model typically produces more satellites than all nearby MW-mass systems, in particular producing a MW-mass galaxy with $\leqslant 2$ satellites $< 0.2\%$ of the time. Treating each of the five known galaxies as an independent binomial trial, a $< 0.2\%$ success rate should yield one success with a $< 1\%$ probability. Moreover, there is *not a single simulated galaxy* whose most massive satellite has $M_\star \leqslant 10^6 M_\odot$. Interestingly, in our 'standard' model, the typical galaxy with a satellite population similar to M94 has approximately the mass of the Large Magellanic Cloud.

To further explore this unexpected result, we also adopt a schematic altered SMHM relation (see Figure 3.3; right panel), with increased mass-dependent scatter starting at a halo mass of $10^{11} M_\odot$, and a significantly steeper slope ($\sim$3) for halos $< 3{\times}10^{10} M_\odot$, along with a 10% probability of not forming a galaxy at all (a 10% 'failure rate'; e.g., *Sawala et al.* 2015) below $10^{10} M_\odot$. Figure 3.4 (right panel) shows that this 'stochastic' halo occupation model reproduces more accurately the typical number of satellites of a MW-mass galaxy, and gives a significantly higher likelihood of producing an M94-like system: >4% of MW-mass galaxies host $\leqslant 2$ satellites — a >16% chance for five galaxies. Additionally, several systems are produced which host a most massive satellite with $M_\star \lesssim 10^6 M_\odot$, though the probability is still $< 1\%$.

While this 'stochastic' model is primarily used for illustrative purposes, it nonetheless strongly resembles the model used by *Garrison-Kimmel et al.* (2017a) to help alleviate the TBTF problem. A broader range in the observed satellite populations around MW-mass hosts in surveys like SAGA (*Geha et al.*, 2017), and even in nearby systems excluding M94 (e.g., M101/MW vs. M81), seems to provide tentative support for this approach. The adopted slope in our stochastic model is quite similar to that of *Moster et al.* (2013) extrapolated to lower halo masses (*Dooley et al.*, 2017). However, we find that adopting such a slope without dramatically increasing the scatter up to high masses cannot adequately reproduce M94's lack of a $M_\star \gtrsim 10^7 M_\odot$

satellite.

To summarize, M94 directly challenges the 'standard' halo occupation model. While our exploration is far from exhaustive, we find that the sparse and low-mass satellite system of M94 may indicate that galaxy formation within DM halos is much more stochastic than predicted, even for halos as massive as $\sim 10^{11} M_{\odot}$ — far above the TBTF mass scale predicted to signal an increase in stochasticity by most current hydrodynamical models (e.g., *Munshi et al.*, 2017; *Fitts et al.*, 2017; *Garrison-Kimmel et al.*, 2019a).

3.6 Conclusions

We have presented the discovery of two low-mass satellites of the MW-mass galaxy M94 in a deep, 150 kpc-radius Subaru HSC survey. Both satellites have $M_V \sim -10$ and $M_{\star} \lesssim 10^6 M_{\odot}$. Both also appear to be actively star-forming, despite projected distances from M94 of < 100 kpc.

We have conducted artificial galaxy tests and have found that our 'classical' dwarf ($M_V \gtrsim -9.1$; $M_{\star} \gtrsim 4 \times 10^5 M_{\odot}$) detection completeness is 85% within our survey footprint up to $\sim 10^6 M_{\odot}$ and is >99% at higher masses — M94 very likely hosts only two 'classical' satellites between projected radii of 15 kpc and 150 kpc.

Furthermore, we have found that most currently accepted SMHM relations and 'standard' method of DM halo occupation cannot produce a satellite population like M94's with sufficient likelihood — $\lesssim 0.2\%$ of MW-mass central galaxies painted onto EAGLE dark matter halos host $\leqslant 2$ 'classical' satellites within 150 kpc in projection, and *none* host a most massive satellite with $M_{\star} \leqslant 10^6 M_{\odot}$. Furthermore, 'standard' halo occupation reproduces the overall satellite population of MW-mass galaxies poorly. In order to substantially increase the probability of forming an M94-like system and improve the fit to the overall population, we have presented a model which increases the scatter in the SMHM relation above 0.2 dex for halos as massive

as $10^{11} M_{\odot}$, culminating in >1 dex of scatter for $10^{9} M_{\odot}$ halos. We also increased the power-law slope of the SMHM relation to $\sim$3 for halos $< 3 \times 10^{10} M_{\odot}$ and assume that some fraction of $< 10^{10} M_{\odot}$ halos fail to form visible galaxies. Consequently, M94 — a 'lonely giant' which appears to only host two low-mass satellites and is completely devoid of massive companions — may advocate for an important modification to current ideas of how the satellites around MW-mass galaxies form.

Acknowledgements

We thank the referee for their thoughtful feedback, which improved this paper. We also thank Annika Peter, Sergey Koposov, and Mario Mateo for helpful suggestions. AS acknowledges support for this work by the National Science Foundation Graduate Research Fellowship Program under grant No. DGE 1256260. Any opinions, findings, and conclusions or recommendations expressed in this material are those of the author(s) and do not necessarily reflect the views of the National Science Foundation.

Based on observations obtained at the Subaru Observatory, which is operated by the National Astronomical Observatory of Japan, via the Gemini/Subaru Time Exchange Program. We thank the Subaru support staff – particularly Tsuyoshi Terai, Chien-Hsiu Lee, and Fumiaki Nakata – for invaluable help preparing and carrying out the observing run.

Based on observations utilizing Pan-STARRS1 Survey. The Pan-STARRS1 Surveys (PS1) and the PS1 public science archive have been made possible through contributions by the Institute for Astronomy, the University of Hawaii, the Pan-STARRS Project Office, the Max-Planck Society and its participating institutes, the Max Planck Institute for Astronomy, Heidelberg and the Max Planck Institute for Extraterrestrial Physics, Garching, The Johns Hopkins University, Durham University, the University of Edinburgh, the Queen's University Belfast, the Harvard-Smithsonian

Center for Astrophysics, the Las Cumbres Observatory Global Telescope Network Incorporated, the National Central University of Taiwan, the Space Telescope Science Institute, the National Aeronautics and Space Administration under Grant No. NNX08AR22G issued through the Planetary Science Division of the NASA Science Mission Directorate, the National Science Foundation Grant No. AST-1238877, the University of Maryland, Eotvos Lorand University (ELTE), the Los Alamos National Laboratory, and the Gordon and Betty Moore Foundation.

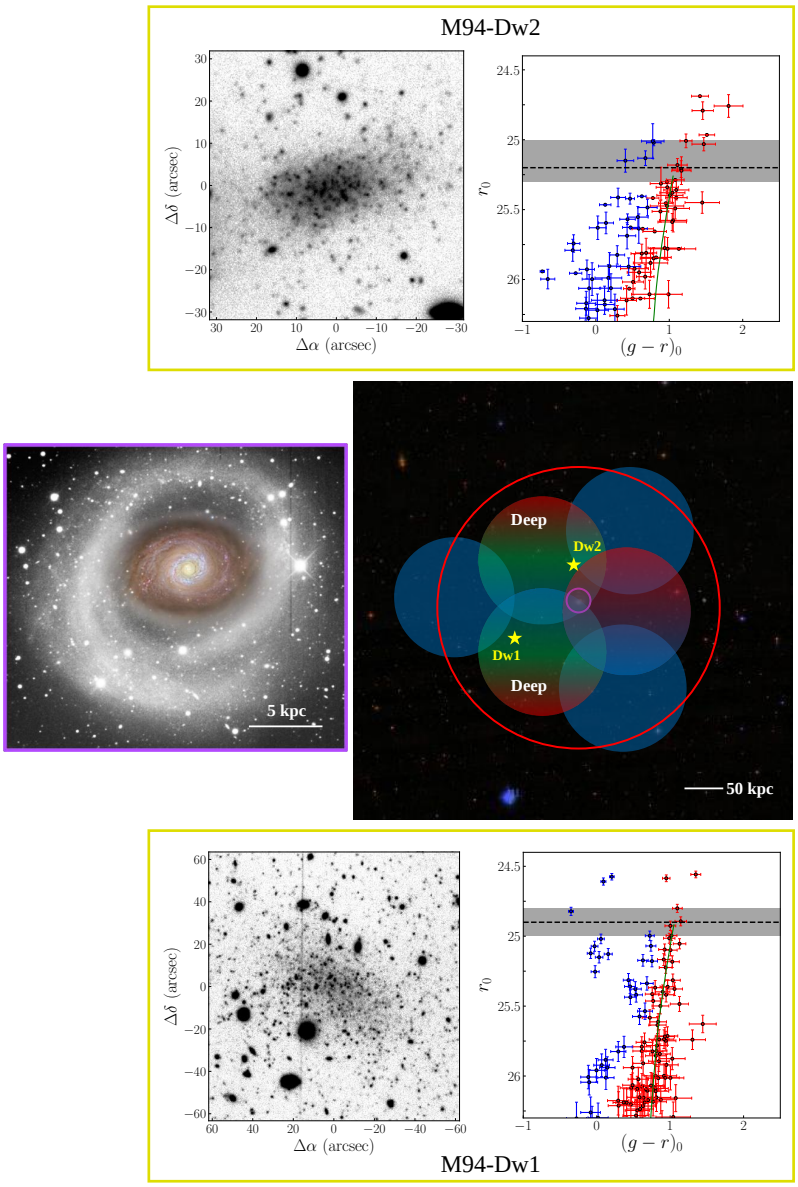

Figure 3.1: Right panel: A ∼5×5 □° SDSS image centered on M94 (magenta circle). The colored circles show the six-pointing HSC survey footprint, while the red circle shows a circle of the same area with 150 kpc 'effective' radius. Blue denotes pointings observed in g-band, green in r-band, and red in i-band. The two deep pointings are labeled. The positions of Dw1 and Dw2 are shown as yellow stars. Bottom panel: Deep r-band image of Dw1, accompanied by a CMD of detected stars in the dwarf. Red points represent RGB stars and blue points represent candidate core Helium-burning stars. The dashed line and gray region show the best-fit TRGB with uncertainty, while the green curve is the best-fit isochrone at that distance. Top panel: Imaging and CMD for Dw2, following the same schema as for Dw1. Left panel: Deep image of M94, taken from *Trujillo et al.* (2009).

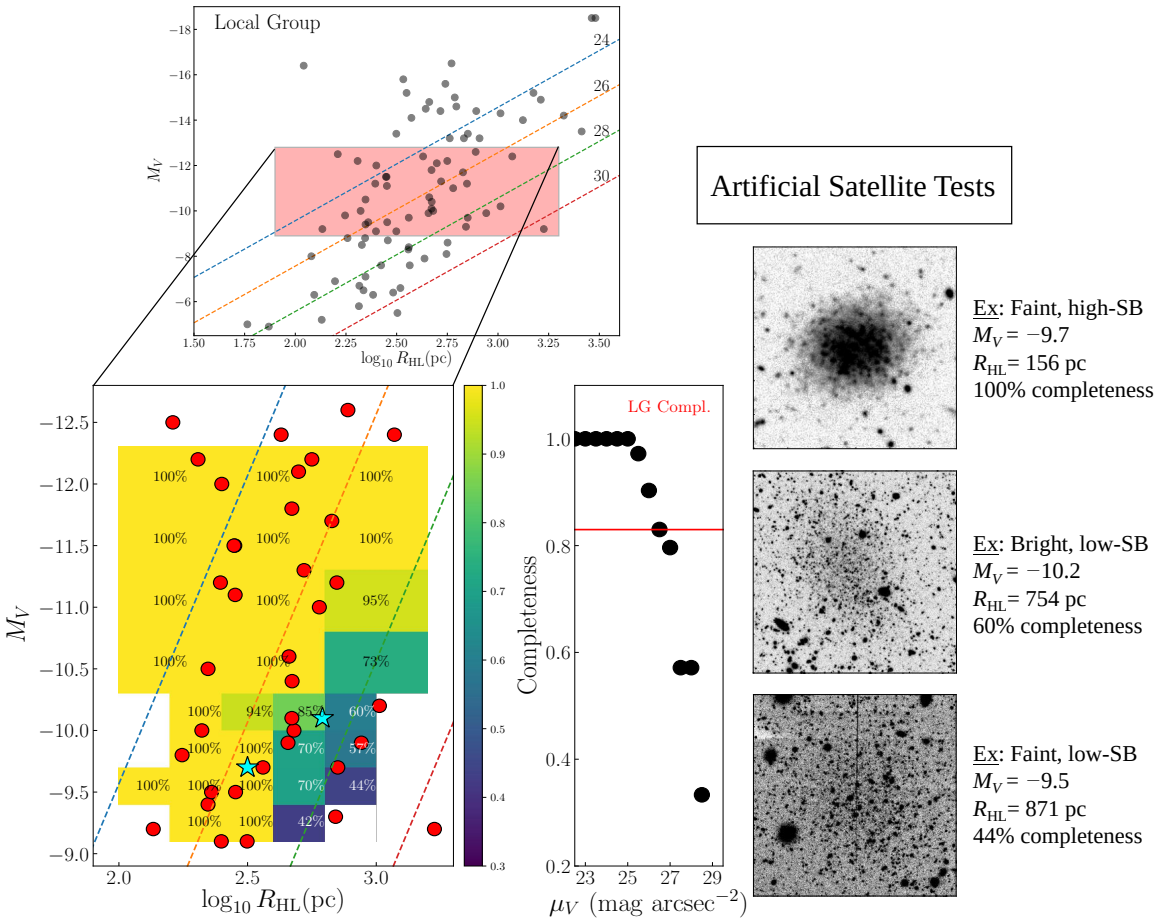

Figure 3.2: Results of our artificial satellite tests. Top left: Size–luminosity relation for *all* satellites of the Local Group in *McConnachie* (2012). Lines of constant SB are shown at 24 (blue), 26 (orange), 28 (green), 30 (red) mag arcsec $^{-2}$. The red patch denotes the approximate region probed by our artificial satellite tests. Bottom left: Recovery completeness map for injected artificial satellites in size–luminosity space. The red circles are LG satellites. The cyan stars represent Dw1 and Dw2. *Right panel*: Completeness as a function of SB for artificial satellites. The red line shows our 85% detection completeness for LG satellites in the range $-9.1 > M_V > -10.3$. Right: Selected examples of detected artificial dwarfs in three different luminosity/SB regimes.

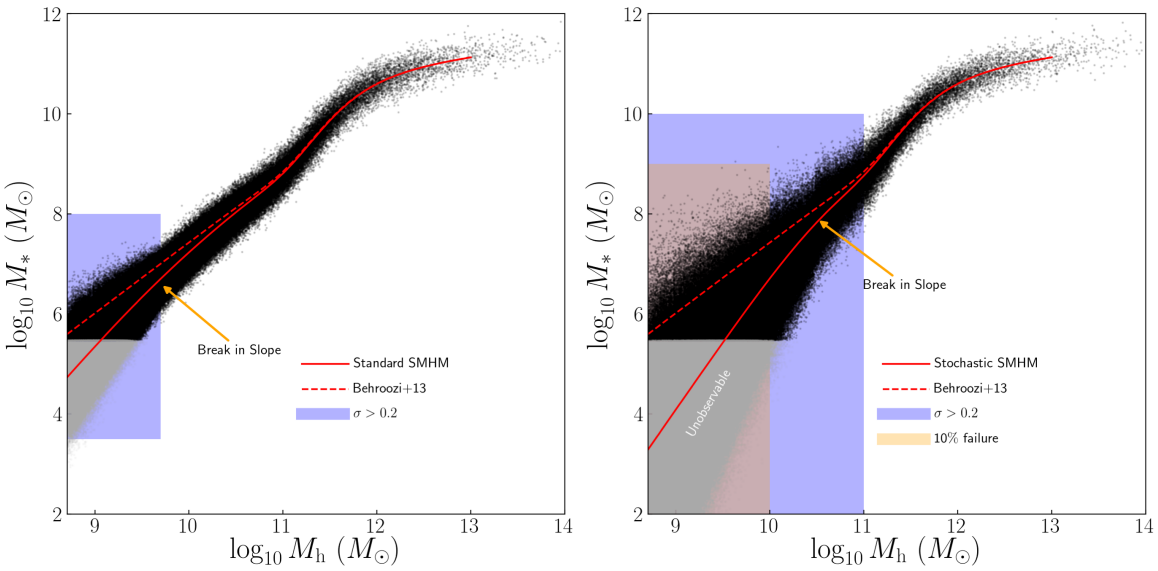

Figure 3.3: Left: The SMHM relation for DM halos in EAGLE using 'standard' halo occupation. The dashed red curve is taken from *Behroozi et al.* (2013). A standard 0.2 dex log-normal scatter is assumed for $M_{\rm h,peak} > 5 \times 10^9 M_\odot$. Below this mass, increased mass-dependent scatter and a steeper slope are adopted following *Munshi et al.* (2017). Gray points denote galaxies which are likely unobservable in our survey of M94. Right: A radically altered SMHM relation, reflecting the stochastic halo occupation implied by M94's sparse satellite population. Increased, mass-dependent scatter is adopted for all halos with $M_{\rm h,peak} < 10^{11} M_\odot$. A significantly steeper slope is also assumed for halos with $M_{\rm h,peak} < 3 \times 10^{10} M_\odot$, along with a fixed 10% rate of galaxy failure for $M_{\rm h,peak} < 10^{10} M_\odot$.

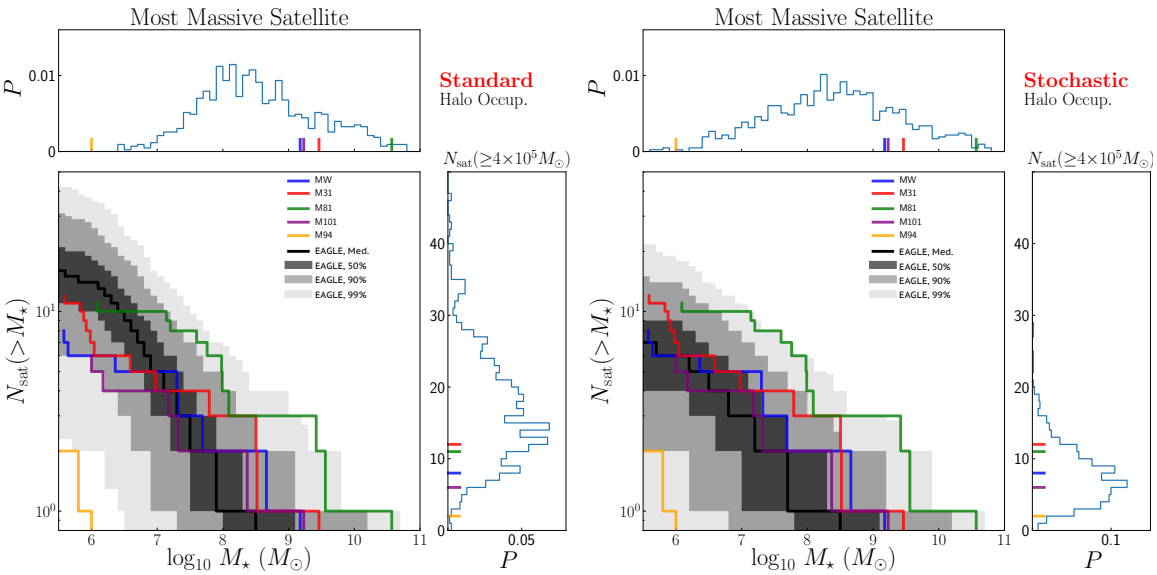

Figure 3.4: Satellite stellar mass functions and statistics for M94 and other nearby galaxies and EAGLE halos, assuming two halo occupation models. Left: Satellite mass functions for nearby galaxies: M94 (orange), the MW (blue), M31 (red), M81 (green), and M101 (purple). Also shown are the median (black line) and 50% (dark gray), 90% (gray), and 99% (light gray) confidence intervals for simulated satellite mass functions for MW-mass galaxies in EAGLE (completeness-corrected for $M_* < 10^6\ M_\odot$), assuming the 'standard' halo occupation described in Figure 3.3. 'Standard' halo occupation produces M94-like systems $< 1\%$ of the time. *Top panel*: Normalized histogram of the most massive satellite formed around each central EAGLE. Known galaxies are shown by vertical lines. *Right panel*: Normalized histogram of the total number of $M_\star > 4\times10^5 M_\odot$ satellites for each central in EAGLE. Known galaxies are shown by horizontal lines. Right: Same as the left panel, but assuming stochastic halo occupation. The shape of the mass function and subsequent distribution of the total number of satellites has changed dramatically, producing M94-like systems >4% of the time.

CHAPTER IV

The Saga of M81: Global View of a Massive Stellar Halo in Formation

4.1 Abstract

Recent work has shown that Milky Way-mass galaxies display an incredible range of stellar halo properties. Yet, the origin of this diversity is unclear. The nearby galaxy M81 — currently interacting with M82 and NGC 3077 — sheds unique light on this problem. We present a Subaru Hyper Suprime-Cam survey of the resolved stellar populations in M81's halo. Using a unique three-filter strategy, and numerous HST calibration fields, we reveal M81's halo in never-before-seen detail. We resolve the halo to unprecedented V-band equivalent surface brightnesses of >34 mag arcsec^{-2}, and produce the first-ever global stellar mass density map for a Milky Way-mass stellar halo outside of the Local Group (LG). Using the minor axis, we confirm the previous assessment of M81 as one of the lowest mass and metal-poorest stellar halos known ($M_\star \sim 10^9 M_\odot$, [Fe/H] ~ -1.2) — indicating a relatively quiet prior accretion history. Yet, in our global stellar mass census we find that tidally unbound material from M82 and NGC 3077 provides a substantial infusion of metal-rich material ($M_\star \simeq 6{\times}10^8\ M_\odot$, [Fe/H] $\simeq -0.9$). We further show that, following the accretion of its massive satellite M82 (and the LMC-like NGC 3077), M81 will host one of the

most massive and metal-rich stellar halos in the nearby universe. Thus, the saga of M81: following a relatively passive history, M81's merger with M82 will completely transform its halo from a low-mass, anemic halo rivaling the MW, to a metal-rich behemoth rivaled only by systems such as M31. This dramatic transformation indicates that the observed diversity in stellar halo properties is primarily driven by diversity in the largest mergers these galaxies have experienced.

4.2 Introduction

In the Λ–Cold Dark Matter (ΛCDM) paradigm, galaxies assemble hierarchically, experiencing frequent mergers with other galaxies (e.g., *White and Rees*, 1978; *Bullock et al.*, 2001). These events transform the morphological and kinematic structure of the central galaxy (*Toomre and Toomre*, 1972), and funnel cold gas into the center of the gravitational potential, stimulating the formation of new generations of stars and enriching the existing interstellar reservoirs (*Barnes and Hernquist*, 1991). As a result of short ($\lesssim$1 Gyr) dynamical and star formation timescales, the impacts of such mergers quickly become well-mixed into the main body of the galaxy, making it incredibly difficult to infer the properties of the progenitor merging system long afterwards.

Fortunately, mergers also deposit a significant amount of loosely-bound stellar material which is retained within the DM halo — the integral debris of all such events comprises the central galaxy's 'stellar halo' (e.g., *Spitzer and Shapiro*, 1972; *Bullock and Johnston*, 2005). Stellar halos act as index fossils of past merger events, encoding the properties of these events long after their impact has been all-but-erased from typical observational diagnostics within the galaxy. Taking advantage of their close proximity, the stellar halos of the Milky Way (MW) and the Andromeda galaxy (M31) have been studied in exquisite detail, from their stellar populations (e.g., *Bell et al.*, 2008, 2010; *Ibata et al.*, 2014; *Gilbert et al.*, 2014; *Williams et al.*, 2015), to

their structure (e.g., *Ibata et al.*, 2001; *Carollo et al.*, 2010; *Deason et al.*, 2011) and kinematics (e.g., *Kafle et al.*, 2012; *Gilbert et al.*, 2018).

The stellar halos of a number of MW-mass galaxies in the Local Volume (LV) have also been studied in detail. As stellar halos of MW-mass galaxies are both large ($\sim$100 kpc) and diffuse ($\mu_V > 28\,\mathrm{mag\,arcsec^{-2}}$), there are several approaches which have been taken: (1) deep integrated light surveys (e.g., *Merritt et al.*, 2016; *Watkins et al.*, 2016), (2) deep 'pencil beam' Hubble Space Telescope (HST) surveys which resolve individual stars (e.g., GHOSTS; *Radburn-Smith et al.*, 2011; *Monachesi et al.*, 2016a; *Harmsen et al.*, 2017), and (3) wide field, ground-based surveys which resolve individual stars (e.g., M31, *Ibata et al.* 2014; M81, *Okamoto et al.* 2015; Cen A, *Crnojević et al.* 2016). Each approach has competing strengths and limitations, including field-of-view (advantage: integrated light), star–galaxy separation (advantage: *HST*), and sensitivity to global halo properties (advantage: ground-based resolved stars). Many nearby MW-like galaxies reside in regions of the sky plagued by significant galactic cirrus. This cirrus emission can substantially limit the sensitivity of integrated light to even bulk halo properties (e.g., *Watkins et al.*, 2016; *Harmsen et al.*, 2017). In these cases, resolved stellar populations are the optimal approach.

These efforts have revealed that, among the $\sim$10 best-measured stellar halos of nearby MW-mass galaxies, there exists a spread of nearly *two orders of magnitude in stellar halo mass*, and more than *1 dex in stellar halo metallicity* (e.g., *Monachesi et al.*, 2016a; *Harmsen et al.*, 2017; *Bell et al.*, 2017, and references therein). Surprisingly, the MW and M31 sit on opposite ends of this distribution — the MW being the least massive and metal-poorest (e.g., *Bell et al.*, 2008), while M31 is the most massive and metal-rich (e.g., *Ibata et al.*, 2014) — highlighting the enormous diversity in the accretion histories of MW-mass galaxies.

Hints of this diversity in stellar halo properties have begun to appear in simulations (e.g., *Monachesi et al.*, 2016b; *D'Souza and Bell*, 2018a; *Monachesi et al.*, 2019),

with indications that much of this diversity can be explain by the slope and scatter in the galaxy stellar mass–halo mass relation below L^*. Yet, the process of stellar halo assembly, and the associated mergers' impacts on the evolution of the central galaxies, is unclear. The question remains: *how are these halos built?*

- It is now becoming clear from models that the most massive merger a galaxy experiences may dominate the observed properties of its stellar halo (e.g., *D'Souza and Bell*, 2018a,b; *Fattahi et al.*, 2019; *Lancaster et al.*, 2019). Yet, what other important mergers did the galaxies experience before the largest event?
- Do large stellar halos require a higher number of substantial mergers over a galaxy's life, as seen in many simulations (e.g., *Johnston et al.* 2008; *Monachesi et al.* 2019), and interpreted from observations of galaxies such as M31 (e.g., *Ibata et al.* 2014; *McConnachie et al.* 2018; *Mackey et al.* 2019)? Or, can halo properties be dominated by a single merger?

The mergers a galaxy experiences throughout its life are likely important drivers of its evolution. However, if stellar halo properties are, indeed, dominated by a single dominant merger, then the other substantial mergers a galaxy may have experienced will be effectively hidden from us for most systems. A powerful approach to address this observational impairment would be to study in detail the stellar halos of systems which are currently undergoing significant (i.e. dominant) mergers. This could simultaneously enable the inference of, and comparisons between, both their *past* and *future* largest mergers, and how such an event impacts the stellar halo. When combined with current measurements for non-merging systems, such an approach could shed invaluable light on the build-up of stellar halos and the evolution of MW-mass systems.

In this paper, we present a Subaru Hyper Suprime-Cam (HSC) survey of the resolved stellar halo populations of the interacting M81 Group (see Fig. 4.1; similar to the earlier survey of *Okamoto et al.* 2015) — the most detailed study of a stellar

Table 4.1. M81 HSC Observations

	Field 1		Field 2	
Filter	# Exposures[a]	Integration time[b] (s)	# Exposures	Integration time (s)
g	14	4200	18	5400
r	11	3300	12	3600
i	11	3300	11	3300

Note. — [a] Total number of 300 s exposures for a single field. [b] Total integration time (i.e. $300\,\mathrm{s} \times N_{exp}$).

halo yet obtained outside of the Local Group (LG). The M81 Group is a quintessential example of a triple-interacting system — hosting vast bridges of tidally stripped H I gas liberated from the two interacting satellites, M82 and NGC 3077 (*Yun et al.*, 1994; *de Blok et al.*, 2018) — and is the nearest ongoing significant merger (3.6 Mpc; *Radburn-Smith et al.* 2011). Using a three-filter, equal-depth observing strategy, as well as numerous overlapping *HST* calibration fields, we combine the relative advantages of 'pencil beam' and ground-based surveys, revealing M81's stellar halo in never-before-seen detail. We use this new quantitative insight to show that, in a single merger event, M81 will span nearly the entire stellar halo mass–metallicity relation: transitioning from a low-mass, metal-poor halo, to one of the most massive, metal-rich halos known — rivaled only by the halos of galaxies such as M31.

4.3 Observations

These observations were taken with the Subaru HSC, through the Gemini–Subaru exchange program (PI: Bell, 2015A-0281). Imaging was undertaken in the 'classical' observing mode over the nights of March 26–27, 2015. The survey consists of two

pointings (each $\sim$1.°5 FOV), in each of three (g, r, i) filters. Pointings were primarily chosen to fully cover the outer regions of all three interacting galaxies — M81, M82, and NGC 3077. Integration times for each field+filter combination are given in Table 4.1. Differences in observing time between the two fields in the same filter reflect adjustments made in response to changing conditions (e.g., sky transparency, background, and seeing).

The data were reduced with the HSC optical imaging pipeline (*Bosch et al.*, 2018). The pipeline performs photometric and astrometric calibration using the Pan-STARRS1 catalog (*Magnier et al.*, 2013), but reports the final magnitudes in the HSC natural system, which we then finally correct to the SDSS filter system. The version of the pipeline adopted here performs background subtraction with an aggressive 32-pixel mesh, optimizing point-source detection and removing most diffuse light. Sources are detected in all three-bands, though i-band is prioritized to determine reference positions for forced photometry. Forced photometry is then performed on sources in the *gri* co-added image stack.

All magnitudes were corrected for galactic extinction following *Schlafly and Finkbeiner* (2011a). We find that, broadly, the M81 Group has relatively consistent E(B–V) $\simeq 0.1$. However, the innermost regions of M82 suffer 'contamination' from dust emission, causing artificially higher estimated extinction. Because of this, we limit E(B–V) to a maximum of 0.1 in the region of M82. Image depth was nearly uniform across the two fields, yielding extinction-corrected point source detection limits of $g = 27$, $r = 26.5$, and $i = 26.2$, measured at $\sim 5\sigma$. See *Bosch et al.* (2018) for an in-depth discussion of the photometric uncertainties output by the HSC pipeline. Seeing was relatively stable, resulting in consistent point-sources sizes of 0.″7–0.″8 down to the detection limits.

4.4 Star–Galaxy Separation & RGB Selection

For galaxies such as M81, which are well beyond the Local Group ($D_{\rm M81} \simeq 3.6$ Mpc; *Radburn-Smith et al.* 2011), the bulk of the resolvable stellar populations (i.e. the stellar main sequence) is too faint to observe. In M81, for example, the main-sequence turn-off of the average halo population (e.g., Age ~ 9 Gyr, [M/H] ~ -1.2; *Durrell et al.* 2010) occurs around $i \sim 31$. Characterization of the stellar halo populations therefore requires a more luminous sub-population to trace the underlying stellar population. Red giant branch (RGB) stars are numerous, luminous, and are well-tied to the underlying stellar population, making them excellent tracers. We detect RGB stars to two magnitudes below the tip (the 'TRGB').

At the depths achieved by this survey (i.e. $g{\sim}27$, $r{\sim}26.5$, $g{\sim}26.2$), the majority of detected sources are background galaxies, rather than stars in M81's halo. As an example, an initial morphological cut selecting sources with FWHM $\leqslant 0\farcs75$ eliminates *80% of sources from our catalog*. For shallower ground-based observations (e.g., the PAndAS survey *Ibata et al.*, 2014), detected background galaxies at the relevant magnitudes are typically more morphologically distinct than at deeper limits, and such a cut results in reasonable star–galaxy separation. Likewise, for *HST* observations, despite reaching comparable limits to this survey, the majority of even faint high-redshift galaxies are morphologically distinguishable from stars (see e.g., *Radburn-Smith et al.*, 2011).

It is at the interface reached by this survey — deep detection limits, yet ground-based image quality — where star–galaxy separation becomes truly challenging. In this regime, many faint background galaxies are as equally point-like as stars, motivating selection criteria beyond morphological cuts. As they are amalgams of numerous stellar populations, galaxies exist at virtually every position in the color–magnitude diagram. Many distant galaxies are located at relatively bluer $g{-}i$ colors compared to RGB stars, resulting in a CMD feature located at $g{-}i \sim 0.1$. However, select-

Table 4.2. RGB Selection Criteria

Type	Description	Criterion
Morphological	Size constraints in each filter and along each axis	$\theta_x(g) < 0\farcs75$ $\theta_y(g) < 0\farcs75$ $\theta_x(r) < 0\farcs75$ $\theta_y(r) < 0\farcs75$ $\theta_x(i) < 0\farcs75$ $\theta_y(i) < 0\farcs75$
Color–Color	Proximity to stellar locus in $g-r$ color	$\lvert(g-r) - (g-r)_{\rm SL}\rvert < \sigma_{g-r} + 0.2$
Color–Magnitude	Vertices of the $g-i$ vs. i RGB selection box	$(g-i,\, i) =$ (0.75,26.0), (1.55,26.0), (2.8,24.5), (2.25,24.2), (1.4, 24.2), (1.0,25.0)

Note. — Morphological: Size is FWHM along each axis. Color–Color: $(g-r)_{\rm SL}$ is the $g-r$ color of the stellar locus at a given $r-i$. σ_{g-r} is the measured source uncertainty in $g-r$.

ing RGB stars by their position in the CMD does not eliminate contamination from background galaxies.

Fortunately, stars inhabit a well-defined 'stellar locus' (SL) in broadband (e.g., $g-r/r-i$) color–color space (e.g., *Ivezić et al.*, 2007; *High et al.*, 2009; *Davenport et al.*, 2014). Our addition of the r filter allows us to leverage this distinct color–color information to distill our RGB sample by an additional 30%. 'Stars' are classified as sources $<0\farcs75$ in size (along both axes) and with $g-r$ distance from the SL $< \sigma_{g-r} + 0.2$ mag at a measured $r-i$ color, where σ_{g-r} is the $g-r$ photometric color uncertainty and 0.2 mag is the adopted systematic width of the SL (from *High et al.* 2009; see also *Smercina et al.* 2017). Figure 4.2 demonstrates this selection process, showing the CMD and color–color diagrams of *all* sources, as well as the final, distilled CMD following our selection algorithm. Though the RGB is easily distinguishable using the SL, the unresolved background galaxy locus at blue colors remains. The locations of each are marked. Finally, we show the CMD of 'contaminant' sources thrown out by our selection. While very similar to the full CMD, the RGB is significantly weaker, especially at bright magnitudes. This highlights the success of our selection process, but also indicates the likely continued presence of faint RGB stars in our 'contaminant' sample, which did not meet our stringent selection criteria. This

choice reflects our *HST* calibration technique, described in § 4.5, which prioritizes the purity of the RGB sample, rather than overall completeness. Table 4.2 gives the parameters for our selection process. The resulting culled sample of 45,619 RGB stars is used throughout the rest of the paper.

4.5 *HST* Calibration

4.5.1 Density Calibration

Though our sample of RGB stars is highly pure, due in large part to the addition of the r-band filter and excellent ground-based image quality, we face a number of competing issues which work to inhibit quantitative inferences from the observed stellar populations — mainly: (1) remaining contamination (from background galaxies), (2) crowding, and (3) incompleteness. We attempt to simultaneously correct for all three of these issues by using existing *Hubble Space Telescope (HST)* observations from the GHOSTS survey, similar to the strategy adopted by *Bailin et al.* (2011) for NGC 253. Within our HSC footprint, there are 13 ACS and WFC3 fields with high-quality stellar catalogs from GHOSTS (*Radburn-Smith et al.*, 2011; *Monachesi et al.*, 2013, 2016a). Furthermore, *Harmsen et al.* (2017) calibrate GHOSTS RGB counts, detected in the F606W/F814W filters, to V-band surface brightness (μ_V), taking into account survey completeness with artificial star tests.

In order to simultaneously account for crowding and incompleteness, we calibrate our Subaru RGB counts against those obtained using HST, within each of the GHOSTS field regions. Figure 4.3 shows a greyscale density map of RGB stars in M81's halo with the positions of existing GHOSTS *HST* fields overlaid. Additionally, we show the sub-linear power-law relationship between RGB surface density measured with HST and Subaru,

$$\log_{10} \Sigma_{\rm RGB}^{\rm Subaru} = 0.68 \log_{10} \Sigma_{\rm RGB}^{\rm GHOSTS} - 0.055, \tag{4.1}$$

which arises primarily from crowding at high densities and photometric incompleteness at low densities. The conversion from density to μ_V in mag arcsec^{-2}, assuming a 10 Gyr, [M/H] $= -1.2$ isochrone, is then

$$\mu_V = -2.5 \log_{10}(\Sigma_{\rm RGB}^{\rm GHOSTS} \times 2.09{\times}10^{-10}), \tag{4.2}$$

where $\Sigma_{\rm GHOSTS}$ is in units of arcsec^{-2} (*Harmsen et al.*, 2017).

The relationship is quite tight, suggesting that all three issues (contamination, crowding, and incompleteness) are relatively uniform across the footprint. Conducting 10,000 bootstrap fits to the data gives a 68% confidence interval which yields only a 0.1 dex uncertainty at the lowest and highest densities, respectively. This method thus allows us to robustly predict the RGB source density one would measure with *HST*, across our entire HSC footprint — allowing derivation of quantitative halo properties such as inferred surface brightness and stellar mass (see § 4.6.1).

4.5.2 Color Calibration

Perhaps the more nuanced measurement of the observed stellar populations is that of color, and in turn estimates of abundance. Our survey is optimally geared to efficiently detecting RGB stars at colors of $g{-}i = 1$–1.5. For M81, this corresponds to limiting g-band magnitudes of $\sim$27. However, the most metal-rich RGB stars, i.e. those with [M/H] $\gg -0.5$, will have g-band magnitudes of 28–29 — substantially fainter than the depths achieved by this survey. Therefore, unless g-band observations are substantially deeper than i-band, any metal-rich populations that might exist will be too faint to observe in this survey, and all similarly-designed ground-based surveys. However, the GHOSTS data for M81 reaches to substantially redder colors in the 13 overlapping fields used in the RGB density calibration (§ 4.5.1). We attempt to use the GHOSTS data to correct for this effect.

Monachesi et al. (2016a) measured color profiles along the major and minor axes of the GHOSTS sample, including M81. To measure more robust colors, which also are intrinsically better-tied to population changes due to metallicity, they adopt a revised color metric, Q. As the isochrone model curve for a metal-poor stellar population is nearly a straight line for the upper portion of the RGB, the Q-color corresponds to a CMD which has been rotated around a point 0.5 magnitudes below the TRGB, such that the RGB is nearly vertical. We adopt the Q metric for this paper as well, for all of our color-based analysis. As we are operating in the $g{-}i$ filters, we define a new $Q_{\rm Col}$ corresponding to a rotation angle of $-22°$.

For direct comparison to our Subaru observations, we convert the GHOSTS CMDs, in each of the 13 fields, from F606W−F814W vs. F814W to $g{-}i$ vs. i, using a [M/H] = −1.2, 10 Gyr old isochrone model (following *Monachesi et al.*, 2016a; *Harmsen et al.*, 2017). A stacked CMD of the 13 fields is shown in Figure 4.4 (top left), as well as a comparison CMD of Subaru stellar candidate sources (top right). The resulting $Q_{\rm Col}$ distributions (bottom left), show a distinct red cut-off in the Subaru sources, relative to GHOSTS. This cut-off results in an offset in the median $Q_{\rm Col}$, between Subaru and GHOSTS, of 0.2 mag bluewards. To better understand this offset, we plot the predicted F606W−F814W vs. $g{-}i$ color–color curves for a grid of 10 Gyr PARSEC isochrones (*Bressan et al.*, 2012; *Chen et al.*, 2015), ranging from [M/H] = −1.5 to 0 (Figure 4.4, bottom right). The median F606W−F814W color in each GHOSTS field (*Monachesi et al.*, 2016a) is shown, against the corresponding $Q_{\rm Col}$-based median $g{-}i$ color measured in Subaru. Four of the fields used for density calibration are very stochastic in their measured colors, as only one or two RGB stars are detected with Subaru. We neglect these fields for our color analysis. The rest of the Subaru/GHOSTS points are well-fit by curves of the same shape as the models, but offset by the same 0.2 mag as seen in the $Q_{\rm Col}$ distributions. This consistent presence of this 0.2 mag 'blue-bias' indicates that we can correct our Subaru colors to

a GHOSTS-equivalent colors, which include the hidden red populations.

We caution that without similar extensive overlap with high-quality *HST*-derived stellar catalogs, it would be impossible to estimate the contribution from higher-metallicity stellar populations and, thus, this 'blue-bias' is *unable to be reliably corrected for*. This effect has been, and will continue to be, an issue for all similarly-designed ground-based stellar population surveys at distances $\gg$1 Mpc.

4.6 Results

In this section, we first present quantitative measurements along M81's minor axis, including average surface brightness (SB) and $g-i$ color profiles (given in Table 4.3 of the APPENDIX). We then present our results for the global stellar halo, including a map of resolved RGB stars, as well as a census of stellar mass in the M81 Group, including the contribution of tidal debris to the stellar halo.

4.6.1 The Minor Axis: Estimating M81's Past Accretion History

The minor axes of galaxy halos are predicted to be relatively free of contamination by *in situ* stars (generally defined as stars which were formed in the central galactic potential, rather than accreted; e.g., *Pillepich et al.* 2015 and references therein) beyond 10 kpc (*Monachesi et al.*, 2016b). As M81 is a highly-inclined galaxy (inclination = 62°; *Karachentsev et al.* 2013), its projected minor axis should be relatively free of such *in situ* stellar populations, allowing minor axis measurements to directly trace the accreted stellar populations. As its current interaction appears to still be in its early stages, M81's minor axis is also relatively free of 'contamination' from the debris of M82 and NGC 3077 (e.g., *Okamoto et al.*, 2015, Fig. 4.3). We discuss the properties and impact of accounting for this debris in § 4.6.2. Thus, M81 is in a unique stage, where despite its ongoing interaction, its minor axis provides a reliable window onto its past ($\gtrsim$1 Gyr ago) accretion history. Figure 4.5 shows the measured average

SB and $g-i$ color profiles along M81's minor axis. Their derivations are described in § 4.6.1.1 and § 4.6.1.2, respectively.

4.6.1.1 Surface Brightness Profile

We define the minor axis according to the region shown in Figure 4.3 (left panel) in red. Leveraging our large survey footprint, we define a much wider minor axis region than is covered by the GHOSTS survey, allowing for more robust averaging and inclusion of any potential substructure absent in the sparse GHOSTS measurements.

We divide the minor axis into projected radial bins, 2 kpc wide from 10–40 kpc, and wider 5 kpc bins outside 40 kpc, to account for the lower number of sources. In each bin, we evaluate the density of RGB-like sources in $\sim$1 arcmin $\times$ 1 arcmin square bins. We then take the mean density across all density bins for each radial bin. Visually inspecting the CMDs in each bin, we find that at radii >60 kpc along the minor axis, the RGB was indistinguishable from a $\sim$uniform background. We thus consider the halo beyond 60 kpc along the minor axis to be undetected. The mean density in each bin is then converted to *HST*-equivalent RGB counts using the method described in § 4.5. Finally, the density was converted to surface brightness using Equation 4.2 (assuming a 10 Gyr, $[\mathrm{M/H}] = -1.2$ isochrone model).

Uncertainties on the density measurements were carefully accounted for from three distinct sources. First, we assume errors on the average density in each bin by taking the standard deviation in density across all pixels, divided by the square root of the number of pixels. Second, we account for the uncertainty in the Subaru–*HST* conversion, denoted by the red 68% confidence region in Figure 4.3. Last, we estimate the systematic uncertainty due to changes in isochrone model parameters, such as age, metallicity, and IMF assumption. To account for this uncertainty, we estimate the change in integrated brightness assuming: age — 10±2 Gyr, metallicity — −1.2±0.2 dex, and IMF — *Chabrier* (2001) vs. (*Kroupa*, 2001). Of these ef-

fects, age accounts for a 15% uncertainty, IMF 27%, and metallicity 3%. Combined, these yield a ∼36% systematic error due to model uncertainty, corresponding to a of 0.5 mag arcsec^{-2} uncertainty in SB.

Figure 4.5 shows the minor axis SB profile for M81. Our measurements are shown in blue, with the GHOSTS points shown in gray for comparison. Our measurements extend ∼30% farther than GHOSTS and reach remarkable depths of $\mu_V > 34$ mag arcsec^{-2} at 60 kpc. This is among the deepest SB profiles ever measured (e.g., compare to: $\mu_V \sim 32$ mag arcsec^{-2}, PISCeS Survey, *Crnojević et al.* 2016; $\mu_V \sim 30$ mag arcsec^{-2}, Dragonfly Survey, *Merritt et al.* 2016).

Fitting a power-law of the form $\Sigma \propto r^{\alpha}$ to the density profile yields a slope of $\alpha = -3.54$, in good agreement with the results of *Harmsen et al.* (2017), despite covering a much wider area along the minor axis. Following (*Harmsen et al.*, 2017), we integrate the profile from 10–40 kpc, using elliptical annuli with the same assumed projected axis ratio of 0.61, obtaining an accreted stellar mass from 10–40 kpc of $M_{\star,10-40} = 3.73 \times 10^8\, M_{\odot}$. Extrapolating to total accreted mass using the *Harmsen et al.* (2017) 10–40-to-total ratio of 0.32, we estimate a total accreted mass of $M_{\star,\mathrm{Acc}} = 1.16 \times 10^9\, M_{\odot}$ — within 2% of the GHOSTS estimate.

Finally, we compare our resolved star-based minor axis SB profile to integrated light measurements, which excel in the bright innermost parts of the galaxy, where resolved star measurements suffer from strong crowding. Figure 4.6 combines our measured profile with a near-infrared version of M81's minor axis SB profile, following *Harmsen et al.* (2017). In this case, we have chosen the *WISE W1* (3.4 µm) profile measured as part of the *WISE* Enhanced Resolution Galaxy Atlas (*Jarrett et al.* 2012; *Jarrett et al.* 2013; T.H. Jarrett, private communication; *Jarrett et al.* 2019). We have adjusted the elliptically-averaged profile to a minor axis-only version using the measured axis ratio for each elliptical annulus. Then, using the same 10 Gyr, [Fe/H] = −1.2 isochrone model which was used to convert our RGB counts to μ_V, we

instead convert these counts to $W1$. The *WISE* profile agrees well with our resolved star-based profile, with the the different methods converging nicely at 10 kpc.

4.6.1.2 Color Profile

We calculate the average minor axis $g-i$ color profile using the same minor axis region, radial bins, and $\sim$arcmin^2 pixels as used for the SB profile (§ 4.6.1.1). For detected sources in each bin, we convert the measured $g-i$ color to $Q_{\rm Col}$ by rotating the CMD -22° around a point (1.62,24.8) 0.5 mag below the TRGB (see § 4.5.2; Figure 4.4). To estimate the average color, we take the median $Q_{\rm Col}$ in each bin and then rotate it back to $g-i$. Finally, we add a 0.2 mag color-correction, following § 4.5.2.

We accounted for uncertainties on our average color measurements from three sources. As described above for the SB profile, we first calculate the standard Poisson uncertainties (from the square root of the number of stars in each bin). Second, we account for uncertainties associated with our *HST* color-correction by drawing 10,000 boostrap samples from both the stacked Subaru and stacked GHOSTS $Q_{\rm Col}$ distributions (see Fig. 4.4), and computing the standard deviation of the difference in the median between the two — resulting in a 0.013 mag uncertainty. The final considered source of uncertainty stems from the intrinsic crowding which afflicts our ground-based data at high densities. Crowding preferentially affects the detection of fainter stars. Because of the increasing RGB $g-i$ color towards brighter RGB stars, as the data become more crowded (i.e. at smaller radii relative to M81, as evident by its steep density profile), the average detected RGB star will also be redder. In an attempt to account for this, we construct distributions of i-band magnitude for stars in each radial bin. We then measure the median magnitude and assess whether this average value shifts with radius. Though not a large effect, we do find that at radii $\gtrsim 25$ kpc the median magnitude is $\sim$constant (at $i \simeq 25$), while getting brighter towards smaller radii — culminating in a maximum difference of 0.25 mag at 10 kpc.

To fold this effect into the uncertainties, we use a range of PARSEC isochrone models (*Bressan et al.*, 2012, and references therein), Age = 10 Gyr and [Fe/H] = −1 to −2, to calculate the change in $g-i$ color, given the measured change in i at each radius. Finding good agreement between the models, we then add the average color difference in quadrature with the Poisson and background uncertainties.

Figure 4.7 shows the minor axis color profile for M81. Our measurements are again shown in blue, and the GHOSTS points again in gray for comparison (*Monachesi et al.*, 2016a). Similarly to the SB profile, our Subaru profile agrees exceptionally well with the GHOSTS profile, though measured over a larger area. As discussed in § 4.5.2, this agreement is entirely contingent on our accounting for the loss of the reddest, most metal-rich RGB stars seen in GHOSTS. We recover the GHOSTS measurement of a ∼flat profile at $R \gtrsim 25$ kpc, $g-i \sim 1.7$. However, we also observe a distinct negative color gradient for $R \lesssim 25$ kpc, which cannot be explained by the effects of crowding (which is incorporated into the error bars). This gradient smoothly connects the flat region of the profile to a single inner GHOSTS field (10 kpc), observed by *Monachesi et al.* (2016a), which is quite red. At first a seemingly 'anomalous' point in the profile, when combined with our Subaru observations, this inner field measurement appears to confirm that M81 possesses a steep minor axis color gradient within 25 kpc.

To estimate how this translates to metallicity, we use the model *HST*–SDSS color–color tracks (§ 4.5.2) to convert our average $g-i$ colors to metallicity, using the calibration of *Streich et al.* (2014). Though this conversion is somewhat uncertain, it is heartening that the outer portion (i.e. >25 kpc) of our halo profile matches the *Durrell et al.* (2010) estimate of [M/H] = −1.2, which used deep *HST* data reaching the 'Red Clump', almost exactly. With this metallicity calibration, we estimate that the ∼0.3 mag change in color from 10–25 kpc corresponds to a ∼0.6 dex change in [M/H], from ~ -1.2 to ~ -0.6. This yields a metallicity gradient of slope ~ -0.04 dex kpc^{-1} inside 25 kpc — 4× steeper than the global metallicity profile of M31, and comparable

to M31's inner 25 kpc (*Gilbert et al.*, 2014).

While this is the first observed case of such a distinct break in the color/metallicity profile of a MW-mass galaxy, galaxies with similar metallicity profiles to M81 — i.e. displaying negative initial gradients, which flatten at large radii — have been observed in simulations (e.g., *Monachesi et al.*, 2019). However, it is very rare to find even a simulated galaxy with such a sharp transition at < 30 kpc. We discuss two possible origins of this steep color profile in § 4.7.

4.6.2 The Global Stellar Halo of M81

While M81's minor axis is a window onto its past accretion history, the global halo properties provide a window onto the current interaction. We first present the globally resolved populations in M81's halo and conduct a census of stellar mass (§ 4.6.2.1), followed by an accounting of the tidal debris around M82 and NGC 3077, and how it impacts M81's current halo properties (§ 4.6.2.2).

4.6.2.1 Stellar Populations and Stellar Mass

In Figure 4.8 we present a global map of resolved RGB stars in M81's halo. Each star has been color-coded by its best-fit photometric metallicity, rather than $g-i$ color, as metallicity is the more intuitive (while uncertain) quantity, and is more directly comparable to other similar datasets. For this result, we estimate metallicity for each individual star, using a grid of PARSEC isochrones, Age = 10 Gyr, ranging from [M/H] = -2 to 0 with steps of Δ[M/H] = 0.05 dex. The distance in $g-i$ color, at the given i magnitude, is evaluated for each star, for each isochrone. The best-fit metallicity is then defined as the model which minimizes the data$-$model $g-i$ color residual. We then add a constant 0.4 dex to the metallicity of each star, reflecting the change in metallicity when adjusting for the 0.2 mag blue color-bias discussed in § 4.5.2 & 4.6.1.2. We display [M/H], rather than [Fe/H], so as to remain agnostic

about [α/Fe]. Accounting for photometric uncertainties alone (not systematic uncertainties associated with different stellar evolution models), the typical [Fe/H] error is $\leqslant 0.2$ dex.

The ongoing interaction between M81, M82, and NGC 3077 is immediately visible in the resolved star map. NGC 3077 outskirts display an 'S' shape, typical in tidally disrupting systems, while M82's debris is more compact. The tidal debris around both satellites is quite metal-rich. The rest of the halo, however, is quite metal-poor, comparable to M81's minor axis. Other than the interaction debris, five previously-known satellite galaxies are visible (IKN: *Karachentsev et al.* 2006; BK5N: *Caldwell et al.* 1998; KDG 61: *Karachentseva and Karachentsev* 1998; d0955+70: *Chiboucas et al.* 2009, 2013; d1005+68: *Smercina et al.* 2017), though there are no obvious substructures.

Figure 4.9 turns our map of resolved RGB stars into a map stellar mass density in M81's halo. Using the method described in § 4.5, we convert our RGB map to *HST*-calibrated counts. Again using a fiducial Age = 12 Gyr, [Fe/H] −1.2 isochrone (following *Harmsen et al.* 2017), we convert RGB density to a corresponding stellar mass density, $\Sigma_\star$ in $M_\odot\,\mathrm{kpc}^{-2}$, computed within $\sim$kpc $\times$ kpc pixels. We showed in Figure 4.6 that this method of SB/stellar mass estimation agrees well with ground-based integrated light measurements. The crowded centers of M81, M82, and NGC 3077 (see Figure 4.8) have been filled in with publicly available K_s-band images from the 2MASS Large Galaxy Atlas (*Jarrett et al.*, 2003). We have clipped $\Sigma_\star$ to $>3\times10^3\,M_\odot\,\mathrm{kpc}^{-2}$ — roughly equivalent to one RGB star kpc^{-2}. Combining our star count measurements with traditional near-infrared imaging, this map of stellar mass spans >4 orders of magnitude — from the dense stellar bulges at the centers of the primary galaxies, to the faintest stellar outskirts. This is among the most sensitive maps of stellar mass-density ever constructed for a MW-mass galaxy.

4.6.2.2 Tidal Debris Around M82 and NGC 3077

Figure 4.8 & 4.9 clearly indicate that there is a significant amount of metal-rich stellar material around M82 and NGC 3077. While M81's minor axis gives the properties of its past accretion history (i.e. $M_{\rm Acc}$ =1.16 $\times 10^9\,M_\odot$; see § 4.6.1.1), any of the material around the two satellites which is unbound should be included in the *current* halo properties. To estimate how much of the material is unbound from M82 and NGC 3077, we estimate their respective tidal radii, using the basic approximation (*von Hoerner*, 1957; *King*, 1962),

$$r_{\rm tid} \simeq R \left(\frac{M_{\star,\rm sat}}{2\,M_{\rm enc}(R)} \right)^{1/3}, \tag{4.3}$$

where $r_{\rm tid}$ is the tidal radius, R is the separation between the central and the satellite adjusted for projection (i.e. $R = \sqrt{3}\,R_{proj}$), $M_{\star,\rm sat}$ is the stellar mass of the satellite, and $M_{\rm enc}(R)$ is the total mass of the central enclosed within R. To estimate $M_{\rm enc}(R)$, we adopt the familiar approximation for a flat rotation curve,

$$M_{\rm enc}(R) = \frac{v_{\rm c}^2\,R}{G}, \tag{4.4}$$

where we have taken $v_{\rm c} = 230\,{\rm km\,s^{-1}}$ from M81's H I rotation curve at 10 kpc (*de Blok et al.*, 2008).

The projected separations from M81 of M82 and NGC 3077 are 39 kpc and 48 kpc, respectively, and their stellar masses are $2.8\times10^{10}\,M_\odot$ and $2.3\times10^9\,M_\odot$ (S4G; *Sheth et al.* 2010, *Querejeta et al.* 2015). Taking $v_{\rm c} = 230\,{\rm km\,s^{-1}}$, this yields projected tidal radii of 10 kpc for M82 and 8.2 kpc for NGC 3077. Circles with radii equal to these tidal radii are shown in white on Figure 4.9. We then consider all material outside of these circles to be unbound. This amounts to $\sim6\times10^8\,M_\odot$ — a substantial fraction of M81's integral past accreted mass ($\sim10^9\,M_\odot$). Taking a mass-weighted average

metallicity of this material yields [Fe/H] $\simeq -0.9$ — significantly more metal-rich than the rest of the halo.

Figure 4.10 combines Figures 4.8 and 4.9. The mass-density map is divided into three average metallicity channels: [Fe/H] ~ -0.5 (red), [Fe/H] ~ -1 (green), and [Fe/H] ~ -1.5 (blue). Each channel is then intensity-weighted and combined into a three-channel color image. This figure highlights the visual impact that the massive and metal-rich debris around M82 and NGC 3077 has on the inferred mass and metallicity of M81's halo.

4.7 The Saga of M81

4.7.1 A Quiet History

As discussed in § 4.6.1.1, the sum total accreted stellar mass from M81's past accretions is $M_{\star,Acc} = 1.16 \times 10^9\, M_\odot$, and is quite metal-poor ([Fe/H] ~ -1.2). If we take the limit that a single satellite dominates the halo properties, then the relationship between stellar halo mass and the mass of the most dominant satellite from *D'Souza and Bell* (2018a) suggests M81's largest past merger was *at most* $M_\star \sim 5 \times 10^8\, M_\odot$ — the mass of the Small Magellanic Cloud (SMC; *McConnachie* 2012). Further, though we cannot reliably constrain the origin of M81's inner color profile, if it has an accretion origin, the steepness of the slope ($\sim$0.04 dex kpc^{-1}) suggests that the event likely occurred early in M81's life (*D'Souza and Bell*, 2018a). It is interesting to note that the MW shows tentative evidence for a rising metallicity profile inside 30 kpc as well (*Conroy et al.*, 2019), though the 3-D measurements, aided by precise distances, are very different from the 2-D projected measurements presented here.

If, instead, the color gradient is driven by increasing contribution of *in situ* material at small radii (e.g., *Zolotov et al.*, 2009; *Font et al.*, 2011), then the current stellar halo mass estimate is an upper limit. To estimate the range of possible *in*

situ fractions, we assume the color of accreted material to be the average color of the 'flat' part of the color profile — $g{-}i \simeq 1.7$. The average color (using the Q method described in § 4.5.2) of RGB stars in the center of M81 — using a central *HST* pointing from the GHOSTS survey (Field 01, ∼3 kpc) — is $g{-}i = 2.17$, which we adopt as an upper limit on the 'fiducial color' of the *in situ* populations. Using the accreted (f_{Acc}) and *in situ* ($f_{\rm IS} = 1{-}f_{Acc}$) fractions as weights to produce the observed average color profile, we calculate f_{Acc} as a function of radius, and then convolve it with the observed density profile to estimate the integral change to estimated stellar halo mass. In the case of an *in situ* origin for the steep inner color profile, we find a lower limit on the accreted fraction of $f_{Acc} = 0.59$ — corresponding to a lower limit on M81's total accreted mass of $M_{\star,Acc} = 6.8{\times}10^8\,M_\odot$.

The punch line: regardless of the origin of its intriguing steep inner color profile, M81 has likely experienced a quiet accretion history for the vast majority of its life, accreting only satellites the size of the SMC or smaller.

4.7.2 The Formation of a Massive Stellar Halo

That quiet history is over, however. M81 ($6.3{\times}10^{10}\,M_\odot$; *Querejeta et al.* 2015) is currently undergoing a ∼1:2 merger with its massive satellite M82 ($2.8{\times}10^{10}\,M_\odot$; *Querejeta et al.* 2015) and the ∼LMC-mass NGC 3077 ($2.3{\times}10^9\,M_\odot$; *Querejeta et al.* 2015). In § 4.6.2.2, we showed that there is a significant amount of metal-rich material currently unbound from M82 and NGC 3077 — $\sim 6{\times}10^8\,M_\odot$, [Fe/H] ≃ −0.9. Accounting for this unbound material increases M81's average halo metallicity and increases M81's halo mass by ∼50%. It is clear from their star formation histories that M82 and NGC 3077 began their interaction with M81 *at the same time*. Moreover, the star formation history of the group, including bursts of star formation in the disk of M82 (e.g., *Rodríguez-Merino et al.*, 2011; *Lim et al.*, 2013), the center of NGC 3077 (e.g., *Notni et al.*, 2004), the tidal H I field between the three galaxies (e.g., *de*

Mello et al., 2008), and 'tidal' dwarf galaxies such as Holmberg IX (e.g., *Sabbi et al.*, 2008), all suggest that this merger began $<1\,\mathrm{Gyr}$ ago. In $<1\,\mathrm{Gyr}$ this merger has already had a substantial impact on the properties of M81's stellar halo.

Though a robust dynamical model does not exist for the future of the M81 system, such models have been constructed for the MW's interaction with the LMC. *Cautun et al.* (2019) estimate that the LMC will merge with the MW within $\sim$2.4 Gyr. Though the orbital properties of M82 and NGC 3077 are unclear, M82 is significantly more massive than the LMC, and thus will likely merge with M81 within the next $\sim$2 Gyr. What, then, will be the properties of M81's stellar halo $\sim$2 Gyr in the future, following its accretion of M82 and NGC 3077? The addition to the accreted mass is simply the combined stellar mass of both satellites — an addition of $\sim 3\times10^{10}\,M_{\odot}$ (93% comes from M82), which is $>20\times$ larger than the total current accreted mass. Clearly this merger event will dominate the stellar halo mass of M81. The metallicity will also be significantly impacted. Assuming M82 and NGC 3077 follow the galaxy stellar mass–metallicity relation, they possess metallicities of $[\mathrm{Fe/H}]\sim0$ and $[\mathrm{Fe/H}]\sim-0.6$, respectively (*Gallazzi et al.*, 2005) — much higher than the stellar halo's current metallicity of $[\mathrm{Fe/H}]\simeq-1.2$.

In Figure 4.11, we show the evolution of M81's stellar halo properties in the context of the observed stellar halo mass–metallicity relation for eight nearby MW-mass galaxies (e.g., *Bell et al.*, 2017), discussed in § 4.2. Though several versions of this relation exist in the literature, here we adopt, as metrics, total accreted stellar mass ($M_{\star,Acc}$; x-axis) and metallicity measured at 30 kpc ($[\mathrm{Fe/H}]_{30\,\mathrm{kpc}}$; y-axis).

Prior to its current interaction, M81 possessed one of the lowest-mass and metal-poorest stellar halos in the nearby universe; among the eight examples shown here, only the MW is comparable in mass and metallicity. The massive tidal debris from M82 and NGC 3077 augments and enriches its stellar halo, but *rapidly*. This is no modest evolution of halo properties, but an initial step precipitating a giant

leap. In the next several Gyrs, after the merger has completed, the enormous amount ($M_\star \simeq 3{\times}10^{10}\,M_\odot$) of metal-rich material accreted from M82 and NGC 3077 ([Fe/H] ~ -0.1; mass-weighted material from both M82 and NGC 3077) will have completely transformed M81's stellar halo — the resulting behemoth will have few peers in the nearby Universe. Among its few rivals will be well-known examples of massive stellar halos such as Cen A, NGC 3115, and the stellar halo paragon: M31. In fact, in stellar mass, central density, and starbursting nature, M82 strongly resembles the proposed progenitor galaxy M32p, which *D'Souza and Bell* (2018b) hypothesize merged with M31 $\sim$2 Gyr ago, resulting in M31's current massive stellar halo.

This is the first complete view of the evolution of a galaxy's stellar halo throughout a merger event. It is clear that such a window on a major merger event has the potential to help us better understand the formation and evolution of systems with massive stellar halos, such as M31. Between the measurements along M81's minor axis and the analysis of its current merger with M82 and NGC 3077, we have constrained M81's three largest merger partners over its lifetime: (1) M82, (2) NGC 3077 — an LMC-analog, and (3) the ancient $\sim$SMC-mass primary progenitor of M81's past halo. If not for M82, M81's dominant merger history would closely resemble that of the MW. M81's ancient accreted halo is very comparable to the MW's halo (Figure 4.11), indicating that a single stochastic, M82-like merger is capable of transforming a MW-like halo into a halo such as M31's. This is direct and powerful evidence that the diversity in stellar halo properties is thus driven primarily by the diversity in the properties of the most dominant mergers.

4.8 Conclusions

We have presented a survey of the stellar halo of M81 with Subaru HSC. Using abundant existing *HST* fields, we have calibrated our wide-field, ground-based catalog of RGB stars to space-based catalogs from the GHOSTS survey, in order to obtain

one of the most detailed views of a stellar halo outside of the LG. We find the *HST* data to be *crucial for measuring accurate stellar population properties*, and caution that without similar extensive overlap with space-based stellar catalogs, the effects of completeness and 'blue-bias' in any distant ($\gg$1 Mpc), ground-based stellar halo measurements are unable to be reliably corrected for. We measure:

1. M81's minor axis SB profile (inferred from resolved star counts) out to 60 kpc, reaching $\mu_V > 34\,\mathrm{mag\,arcsec^{-2}}$ — among the deepest SB profiles ever measured. We measure a density slope of -3.54, consistent with the profile measured by the GHOSTS survey with *HST* (*Harmsen et al.*, 2017). We also convert our star count profile to near-infrared SB and compare to *WISE W1* measurements of the inner 10 kpc of M81, finding good agreement. Using this calibrated SB profile, we estimate a total past accreted stellar mass for M81 of $1.16\times10^9\,M_\odot$ — indicating a largest past accretion of *at most* the mass of the SMC.

2. M81's average $g-i$ color profile out to 60 kpc. We measure a flat color profile ($g-i=1.7$, [Fe/H] ~ -1.2) from 25–60 kpc, as seen by the GHOSTS survey (*Monachesi et al.*, 2016a). We also observe, for the first time, a steep negative color gradient ($\sim$0.04 dex kpc^{-1}) at $R=10$–25 kpc. Though we are unable to differentiate an accreted vs. *in situ* origin for the inner color gradient, M81's halo metallicity of [Fe/H] ~ -1.2 at 30 kpc is in line with its past accreted mass of $\sim10^9\,M_\odot$, relative to the stellar halo mass–metallicity relation (see Figure 4.11).

3. Globally resolved stellar halo populations. Our metallicity-coded map of RGB stars reveals the triple interaction between M81, M82, and NGC 3077, highlighting the stark contrast between properties of M81's halo at large radii and the metal-rich debris around the interacting satellites.

4. Stellar mass density on $\sim$1 kpc scales, down to $\Sigma_\star < 10^4\,M_\odot\,\mathrm{kpc^{-2}}$. Using this

sensitive map of stellar mass density, we estimate the amount of tidal debris which is currently unbound from M82 and NGC 3077 — $\sim 6 \times 10^8\, M_\odot$, with an average metallicity of [Fe/H] ~ -0.9. This unbound debris represents a significant infusion of metal-rich material to the 'current' stellar halo of M81.

Together, these measurements allow us to piece together 'the saga of M81'. This MW-analog experienced a quiet history, accreting at most an SMC-mass satellite, likely sometime early in its life. Its current mergers with M82 and NGC 3077, however, has already altered M81's stellar halo properties on a short (< 1 Gyr) timescale, providing a substantial infusion of unbound metal-rich material. In the next several Gyrs, its merger with M82 will transform M81's halo from one of the least massive and metal-poorest, into one of the most massive and metal-rich halos known, rivaling (perhaps even exceeding) prototypical examples of massive halos such as that of M31.

Furthermore, M81's stochastic stellar halo transition, from a low-mass and metal-poor halo to high-mass and metal-rich, is direct evidence that the *diversity in stellar halo properties* at the MW-mass scale translates directly to a *diversity in the largest mergers* these galaxies have experienced.

Acknowledgements

We thank Tom Jarrett and the WISE extragalactic working group for access to the *WISE* surface brightness data for M81. A.S. acknowledges support for this work by the National Science Foundation Graduate Research Fellowship Program under grant No. DGE 1256260. Any opinions, findings, and conclusions or recommendations expressed in this material are those of the author(s) and do not necessarily reflect the views of the National Science Foundation. E.F.B. is partly supported by NASA grant NNG16PJ28C through subcontract from the University of Washington as part of the *WFIRST* Infrared Nearby Galaxies Survey. A.M. acknowledges support from

CONICYT FONDECYT Regular 1181797.

Based on observations utilizing Pan-STARRS1 Survey. The Pan-STARRS1 Surveys (PS1) and the PS1 public science archive have been made possible through contributions by the Institute for Astronomy, the University of Hawaii, the Pan-STARRS Project Office, the Max-Planck Society and its participating institutes, the Max Planck Institute for Astronomy, Heidelberg and the Max Planck Institute for Extraterrestrial Physics, Garching, The Johns Hopkins University, Durham University, the University of Edinburgh, the Queen's University Belfast, the Harvard-Smithsonian Center for Astrophysics, the Las Cumbres Observatory Global Telescope Network Incorporated, the National Central University of Taiwan, the Space Telescope Science Institute, the National Aeronautics and Space Administration under Grant No. NNX08AR22G issued through the Planetary Science Division of the NASA Science Mission Directorate, the National Science Foundation Grant No. AST-1238877, the University of Maryland, Eotvos Lorand University (ELTE), the Los Alamos National Laboratory, and the Gordon and Betty Moore Foundation.

Based on observations obtained at the Subaru Observatory, which is operated by the National Astronomical Observatory of Japan, via the Gemini/Subaru Time Exchange Program. We thank the Subaru support staff — particularly Akito Tajitsu, Tsuyoshi Terai, Dan Birchall, and Fumiaki Nakata — for invaluable help preparing and carrying out the observing run.

The authors wish to recognize and acknowledge the very significant cultural role and reverence that the summit of Maunakea has always had within the indigenous Hawaiian community. We are most fortunate to have the opportunity to conduct observations from this mountain.

4.9 Appendix: Minor Axis Profile Table

In Table 4.3 we provide the radial profiles along M81's minor axis for μ_V (V-band SB) and average $g-i$ color, respectively. See Figure 4.5 & 4.7 for plots of each profile.

Table 4.3: Minor Axis SB & Color Profiles

R (kpc)	μ_V (mag arcsec^{-2})	$g-i$ (mag)
10	28.02 ± 1.46	$1.99^{-0.13}_{+0.02}$
12	28.23 ± 1.02	$1.94^{-0.09}_{+0.02}$
14	28.71 ± 0.66	$1.89^{-0.09}_{+0.02}$
16	29.26 ± 0.45	$1.90^{-0.09}_{+0.02}$
18	29.52 ± 0.44	$1.78^{-0.04}_{+0.02}$
20	30.27 ± 0.34	$1.79^{-0.05}_{+0.02}$
22	30.75 ± 0.29	$1.79^{-0.02}_{+0.02}$
24	31.13 ± 0.31	$1.75^{-0.02}_{+0.02}$
26	31.75 ± 0.31	$1.76^{-0.02}_{+0.02}$
28	31.93 ± 0.32	$1.72^{-0.02}_{+0.02}$
30	32.13 ± 0.33	$1.71^{-0.02}_{+0.02}$
32	32.54 ± 0.35	$1.70^{-0.02}_{+0.02}$
34	32.51 ± 0.34	$1.67^{-0.02}_{+0.02}$
36	32.32 ± 0.34	$1.70^{-0.02}_{+0.02}$
38	32.69 ± 0.36	$1.71^{-0.02}_{+0.02}$
40	32.64 ± 0.35	$1.69^{-0.02}_{+0.02}$
45	33.18 ± 0.39	$1.71^{-0.02}_{+0.02}$
50	33.60 ± 0.42	$1.72^{-0.02}_{+0.02}$
55	34.10 ± 0.45	$1.67^{-0.03}_{+0.03}$
60	34.46 ± 0.48	$1.68^{-0.02}_{+0.02}$

Note. — The radial minor axis average surface brightness and average $g-i$ color profiles as shown in Figure 4.5 & 4.7. See § 4.6.1.1 and § 4.6.1.2 for discussion of how the measurements and uncertainties are computed.

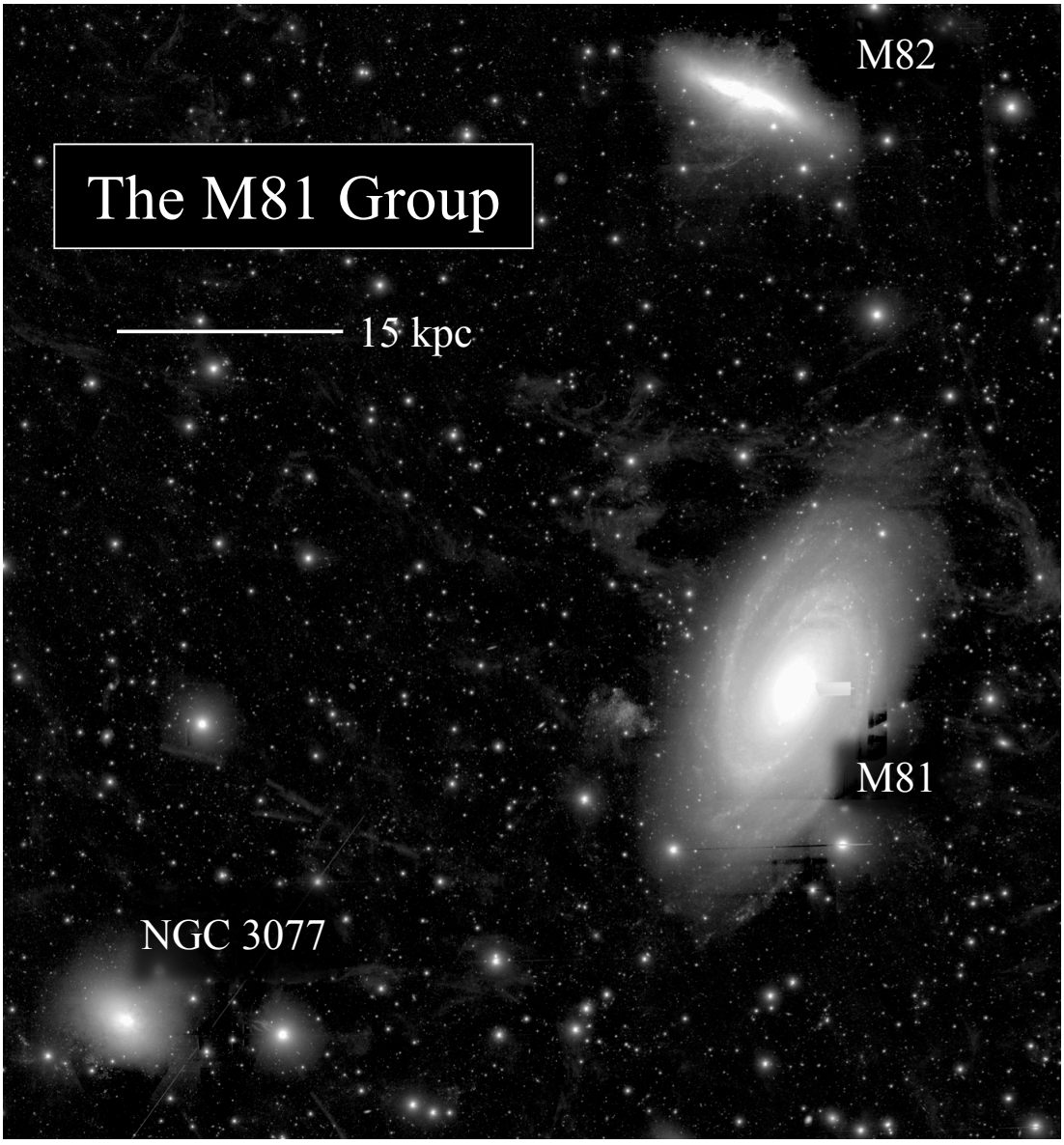

Figure 4.1: A deep, wide-field ($\sim$50 kpc $\times$ 60 kpc) g-band mosaic of the M81 Group, taken with Subaru HSC. A logarithmic stretch was used. The three primary interacting group members are labeled (M81, M82, and NGC 3077). The visible dark patches around the three galaxies, as well as bright stars, represent chip bleeds. The M81 Group is located behind a region of significant galactic cirrus, visible as patches of scattered light. This widespread cirrus impedes the inference of stellar halo properties through integrated light alone.

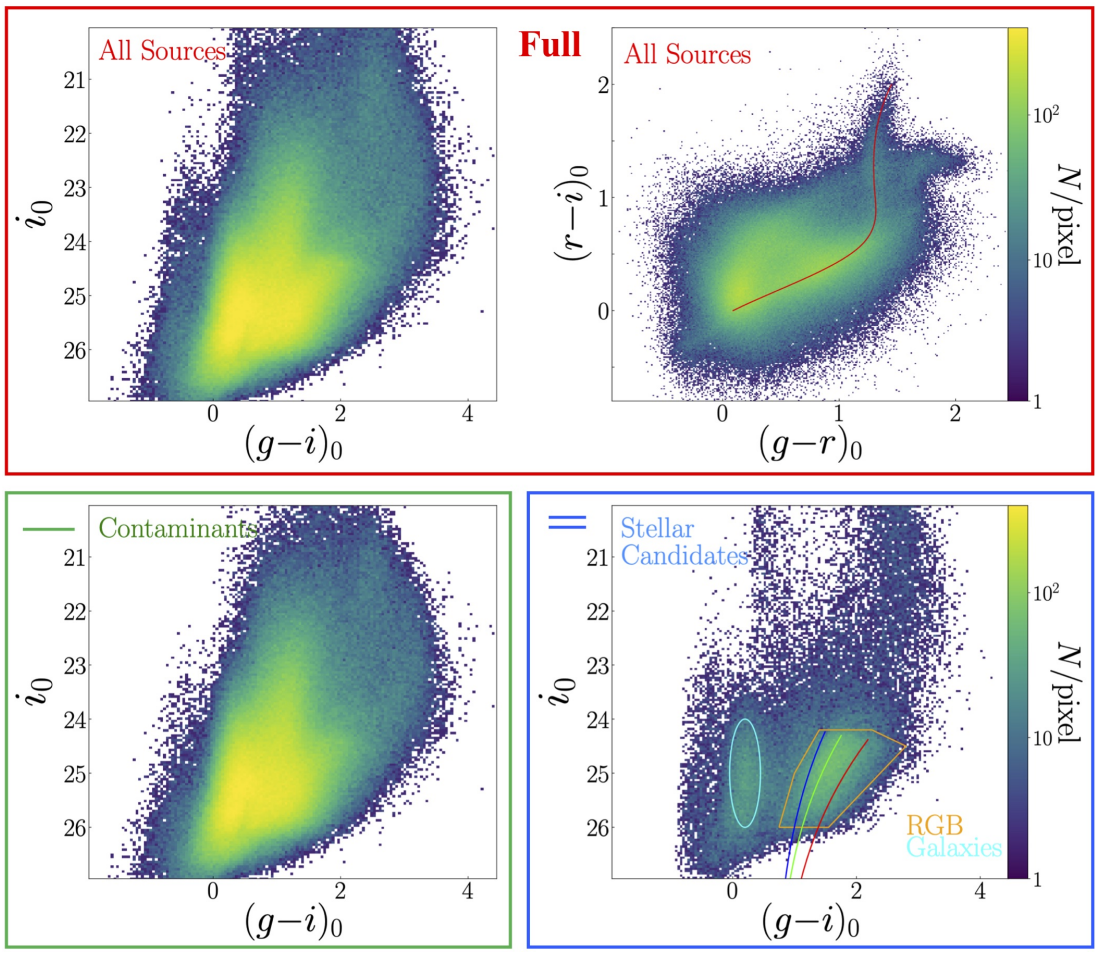

Figure 4.2: **Top left:** $g-i$ vs. i CMD of all detected sources in our survey footprint. **Top right:** Color–color diagram of all detected sources. The stellar locus is shown as a red curve. Only sources lying on the stellar locus, within their photometric uncertainties, are selected. **Bottom left:** $g-i$ vs. i CMD of all sources thrown out in our selection process. **Bottom right:** $g-i$ vs. i CMD of all morphologically ($<0\farcs75$) and color-selected ($<\sigma+0.2$ mag from SL) stars. The locus of unresolved background galaxies (cyan ellipse) is now easily distinguishable from the RGB selection box (orange). Three stellar isochrone models are shown (age = 12 Gyr), with metallicities of [Fe/H] = -2, -1.5, and -1.

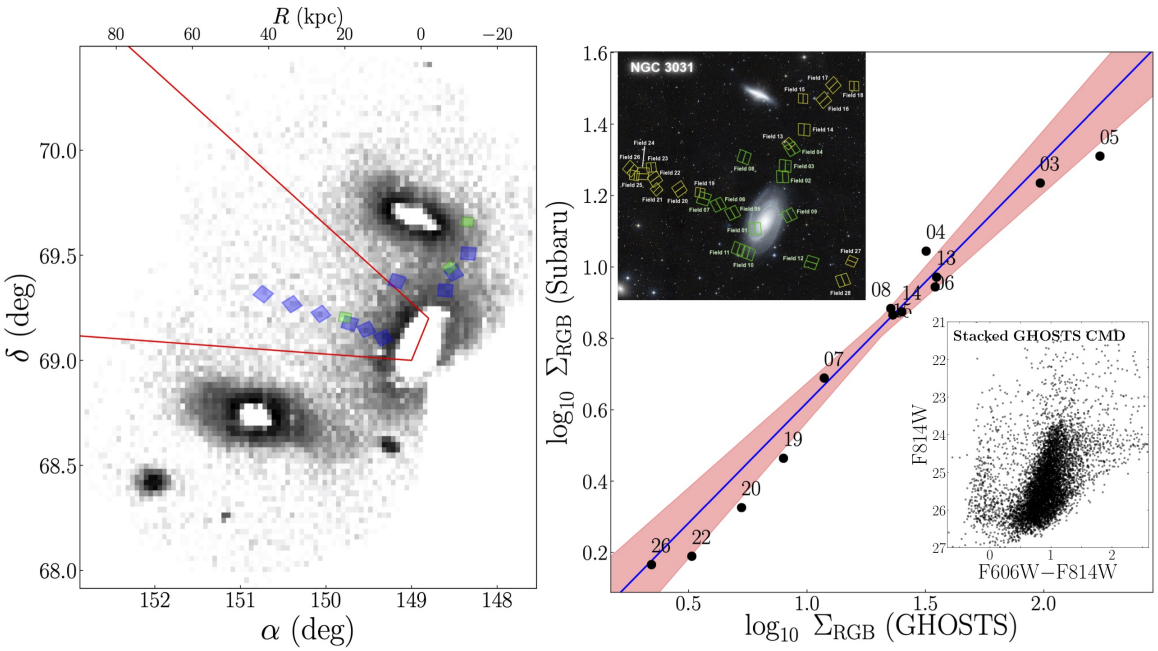

Figure 4.3: **Left:** Grayscale density map of RGB stars in M81's halo. Existing HST fields from the GHOSTS survey (e.g., *Radburn-Smith et al.*, 2011; *Monachesi et al.*, 2013) are overlaid (ACS—blue/WFC3—green). The region defined as M81's 'minor axis' in this paper is shown in red. **Right:** Plot showing our calibration of HSC RGB counts using the GHOSTS survey. The x-axis gives the density of RGB stars within a given GHOSTS field, corresponding to the *Harmsen et al.* (2017) selection box, while the y-axis gives the density of RGB-like sources in the same area from HSC, obtained using our selection criteria (see 4.4). The best-fit power-law is shown (blue), as well as the confidence region containing 68% of the points ($\sim 1\sigma$), obtained from 10,000 bootstrap fits (red shaded). Each field is labeled individually. An inset showing the published GHOSTS field layout on an optical image of the M81 Group is included. Also inset is a stacked CMD of the 13 GHOSTS fields used for this analysis (taken from *Harmsen et al.*, 2017), presented in the F606W & F814W filters.

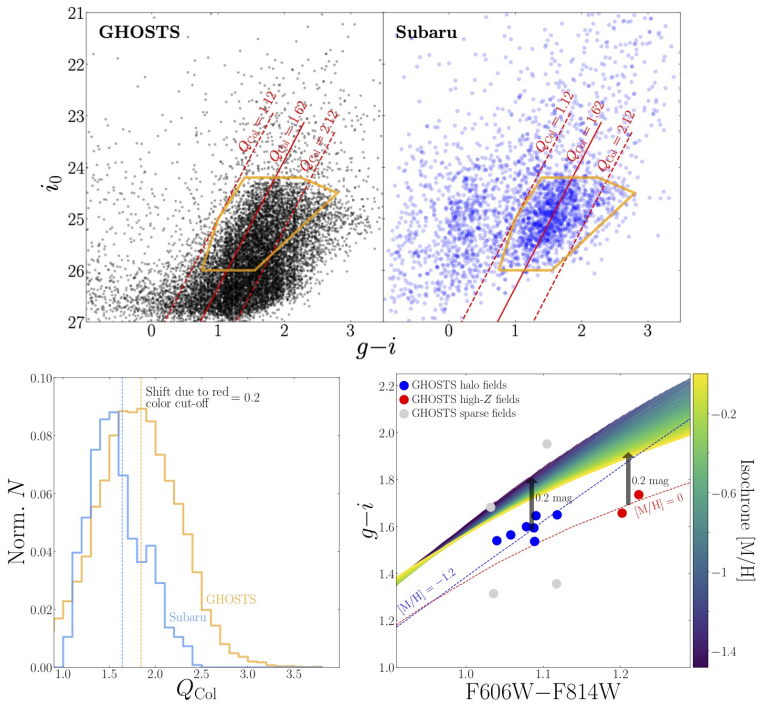

Figure 4.4: Top left: Stacked $g-i$ CMD of stars (black points) in the 13 GHOSTS fields used for calibration, converted from F606W−F814W using isochrone models. Our Subaru RGB selection box (Table 4.2) is overlaid in orange. The solid red line shows the near-straight path of an adopted 'fiducial' isochrone ($[\mathrm{M/H}]\sim-1.2$) through the CMD, with a $g-i$ color of 1.62 (i.e. a line of constant $Q_{\rm Col}=1.62$) at a point 0.5 mag below the TRGB ($i\sim24.8$). Two additional lines of constant $Q_{\rm Col}$ are shown (red dashed), showing a ±0.5 mag change in $Q_{\rm Col}$. Top right: Same as left, but for candidate stellar sources observed with Subaru in the 13 fields. Bottom left: Stacked $Q_{\rm Col}$ distributions for detected Subaru RGB candidates (blue) and detected GHOSTS RGB stars (orange) in the 13 GHOSTS fields. The median $Q_{\rm Col}$ for the Subaru sources is 0.2 mag bluer than the GHOSTS median. When comparing the CMDs obtained from Subaru and GHOSTS (top), it is clear that this offset results from the Subaru $g-i$ completeness curve. We fail to detect a sub-dominant, but substantial, population of red, higher-metallicity stars present in the halo. Bottom right: PARSEC isochrone (e.g., *Bressan et al.*, 2012) predictions for F606W−F814W vs. $g-i$ color–color relationship for RGB stars, as a function of metallicity (colored curves). Overlaid are the median F606W−F814W colors in each of the GHOSTS fields from (*Monachesi et al.*, 2016a) and corresponding median $g-i$ colors, both obtained using the $Q_{\rm Col}$ rotated-CMD metric. Blue points denote 'halo' fields (>10 kpc from M81). Red points denote fields with higher-metallicity populations, which are closer (< 10 kpc) to M81's disk. Gray points are fields which are sparse, often with only one or two stellar candidate sources in Subaru. The halo fields lie on a low-metallicity (e.g., $[\mathrm{M/H}]=-1.2$) model curve (blue dashed), offset bluewards by a constant 0.2 magnitudes in $g-i$. Similarly, the two higher-metallicity fields lie on a high-metallicity (e.g., $[\mathrm{M/H}]=0$) model curve (red dashed), offset 0.2 magnitudes in $g-i$. Though many of the reddest stars are lacking in our Subaru observations, it appears that the stellar halo populations are stable enough to correct for this effect using the GHOSTS data.

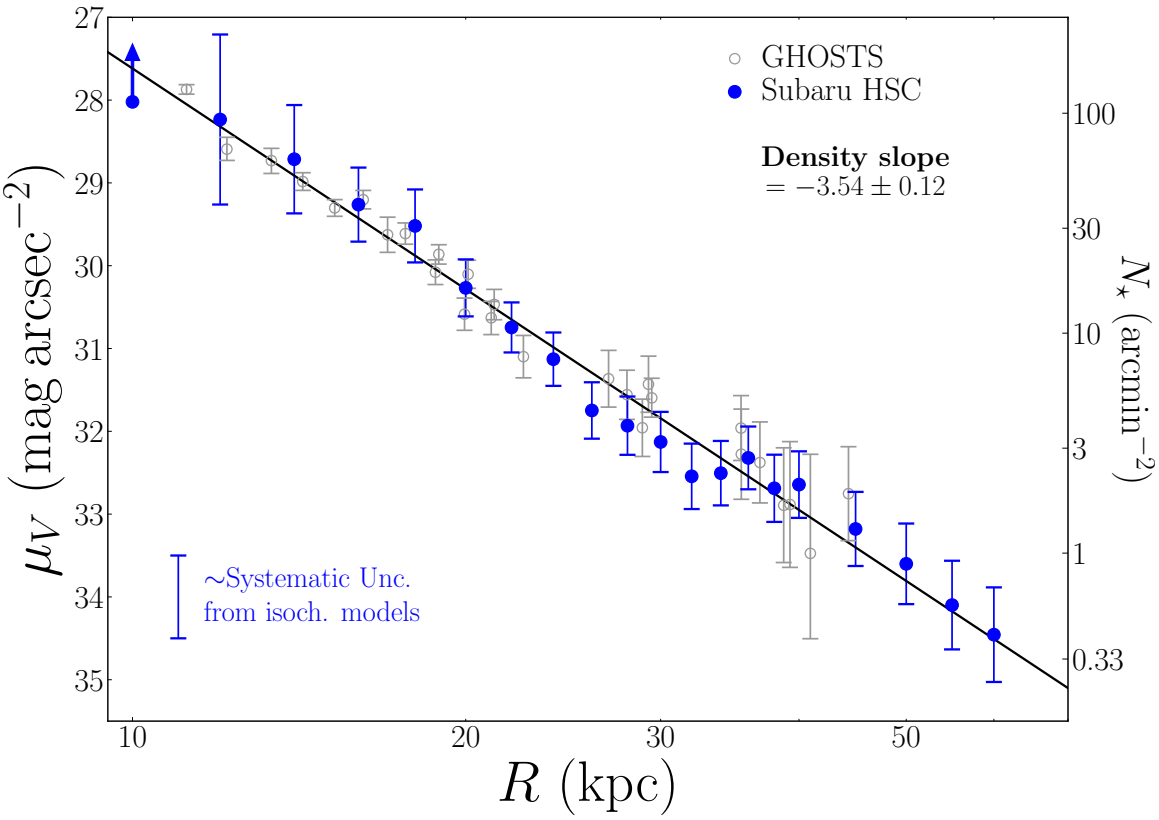

Figure 4.5: M81's average minor axis SB profile (where SB is reported in V-band and radii in kpc) calculated from resolved star counts as described in § 4.6.1.1. The measurements made through this work are shown in blue, while measurements from the GHOSTS survey (*Harmsen et al.*, 2017) are shown in gray for comparison. Corresponding star counts (stars per arcmin^2) are given on the right-hand y-axis. The solid black line is the best-fit density power-law to the data. The best-fit density slope is reported in the top right, which agrees well with the fit of *Harmsen et al.* (2017). We have included a 0.5 mag arcsec $^{-2}$ systematic model uncertainty in the bottom left (§ 4.6.1.1). Reaching $\mu > 34$ mag arcsec $^{-2}$ at 60 kpc, this profile is *one of the deepest ever measured*.

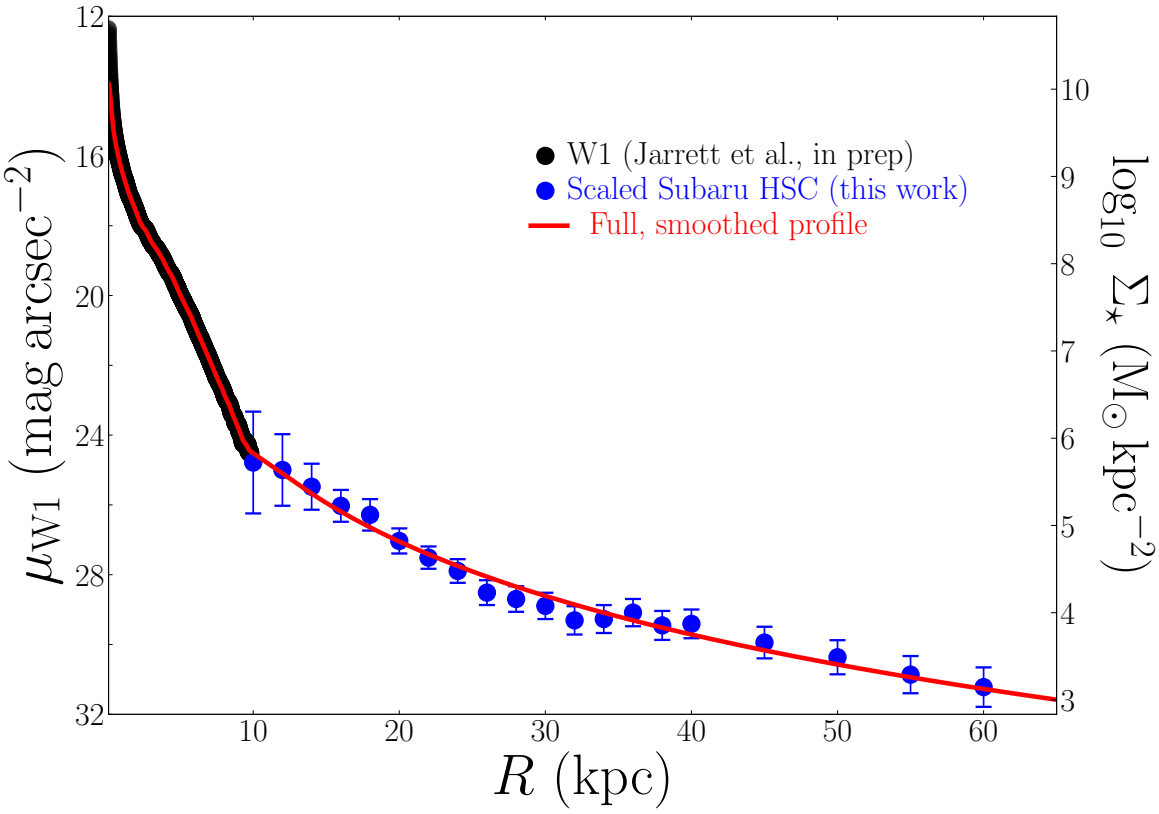

Figure 4.6: Near-infrared SB profile along M81's minor axis, combining *WISE W*1 (*Jarrett et al.*, 2019), which probes M81's interior, with the outer resolved star profile obtained from this work. Corresponding stellar mass density is shown on the right axis (see § 4.6.2 for conversion of μ_{W1} to $\Sigma_\star$). Star counts have been converted to *W1* using our adopted fiducial isochrone model (10 Gyr, [Fe/H] $= -1.2$; see § 4.6.1.1). Black points show the *W1* measurements, while blue points show this work. A smooth, integrated profile is fit to the total profile and shown in red, for visual effect.

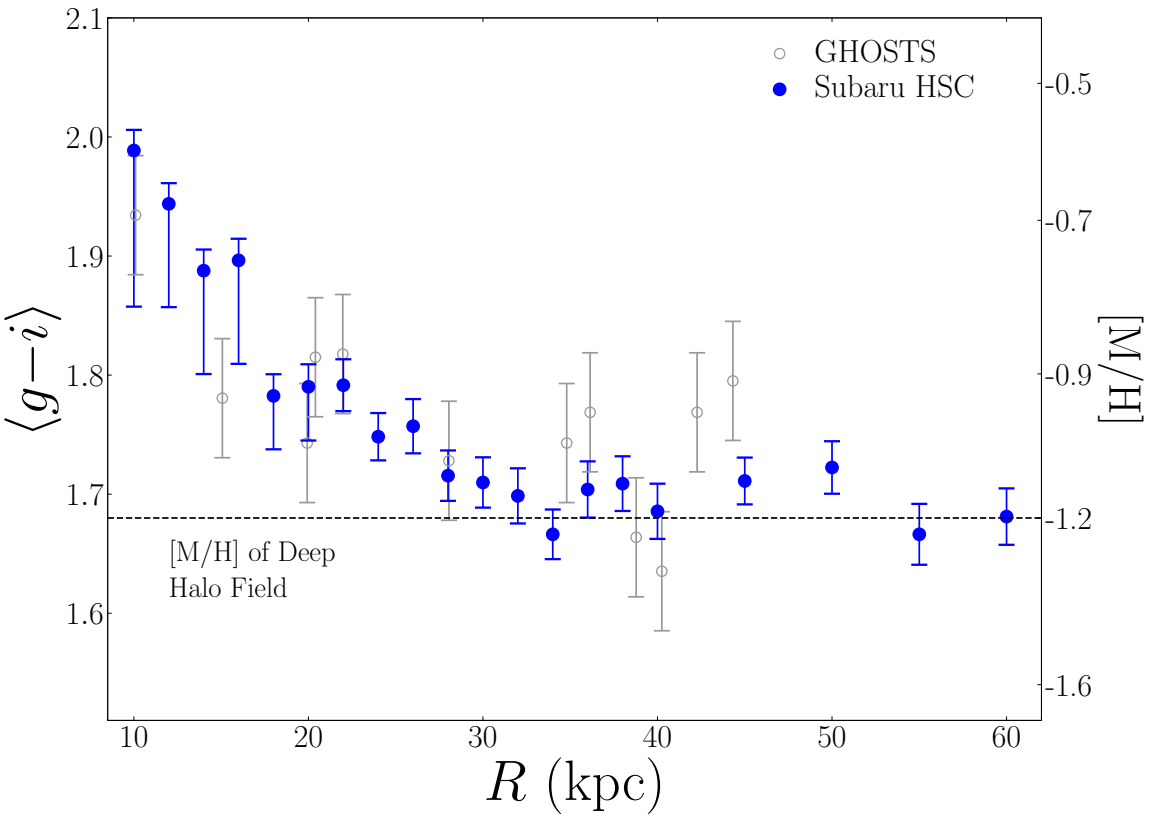

Figure 4.7: Average $g-i$ color profile of resolved RGB stars along M81's minor axis, as described in § 4.6.1.2. Subaru HSC measurements are again shown in blue, while GHOSTS measurements (*Monachesi et al.*, 2016a) are shown in gray. Metallicity, calculated from equivalent F606W−F814 color (*Streich et al.*, 2014), is shown along the righthand y-axis. Additionally, we show the $[\mathrm{M/H}] = -1.2$ metallicity measurement (dashed line) of M81's halo estimated from deep *HST* data (reaching the Red Clump; *Durrell et al.* 2010). We reproduce the flat outer profile ($R \gtrsim 25$ kpc) observed by *Monachesi et al.* (2016a), extending the profile to 60 kpc. We also resolve, for the first time, a distinct break in the color profile at $R \lesssim 25$ kpc, inside which the profile rises steeply — $\sim$0.3 mag in color, ~ 0.6 dex in metallicity from 10–30 kpc.

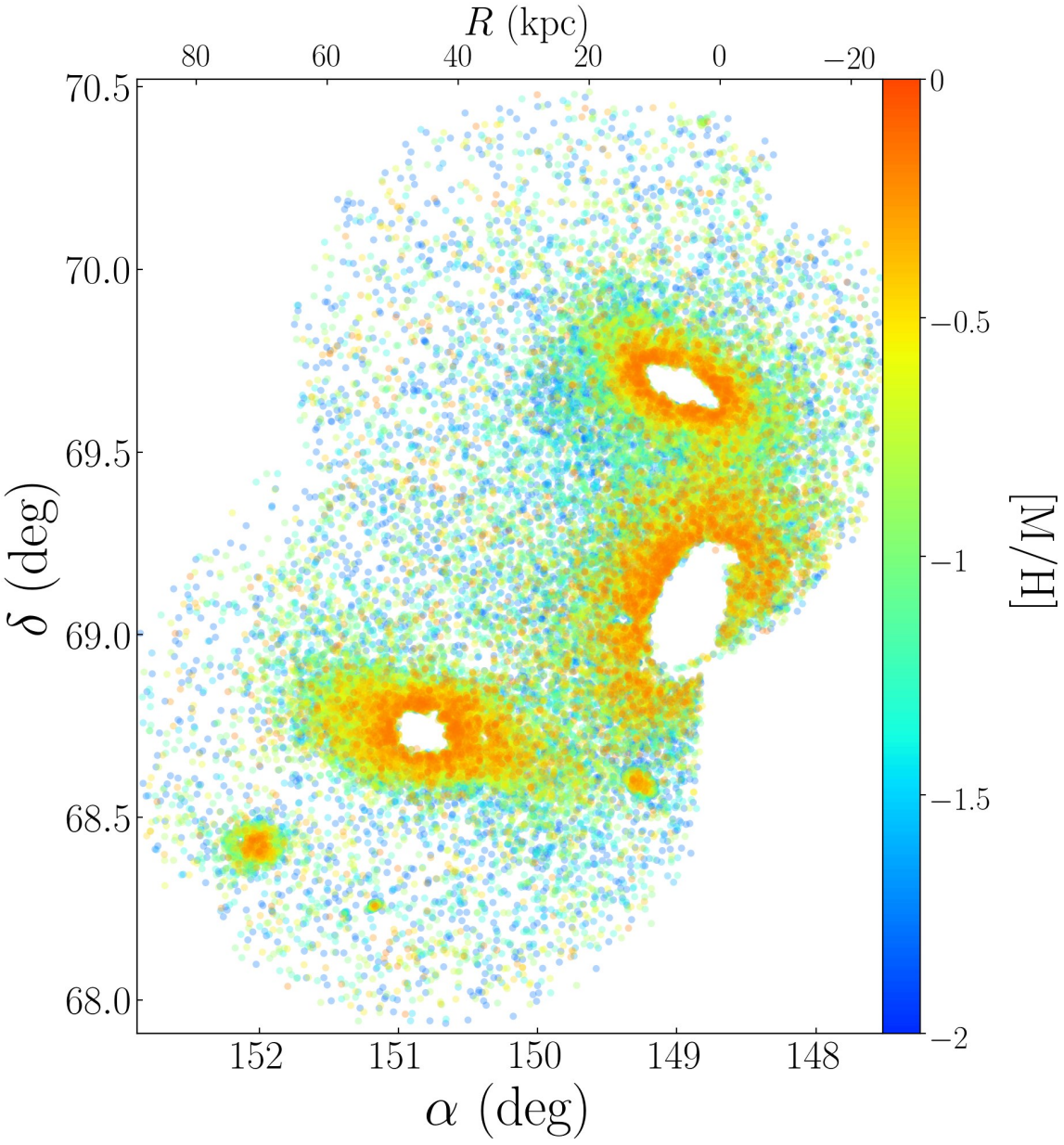

Figure 4.8: Map of resolved RGB stars in the stellar halo of M81. Points have been color-coded by metallicity, determined from isochrone fitting (§ 4.6.2). A scale bar giving projected distance from M81 is shown along the top x-axis. The metal-rich debris from the triple-interaction visually dominates against the surrounding metal-poor halo, though the minor axis remains clear of this debris.

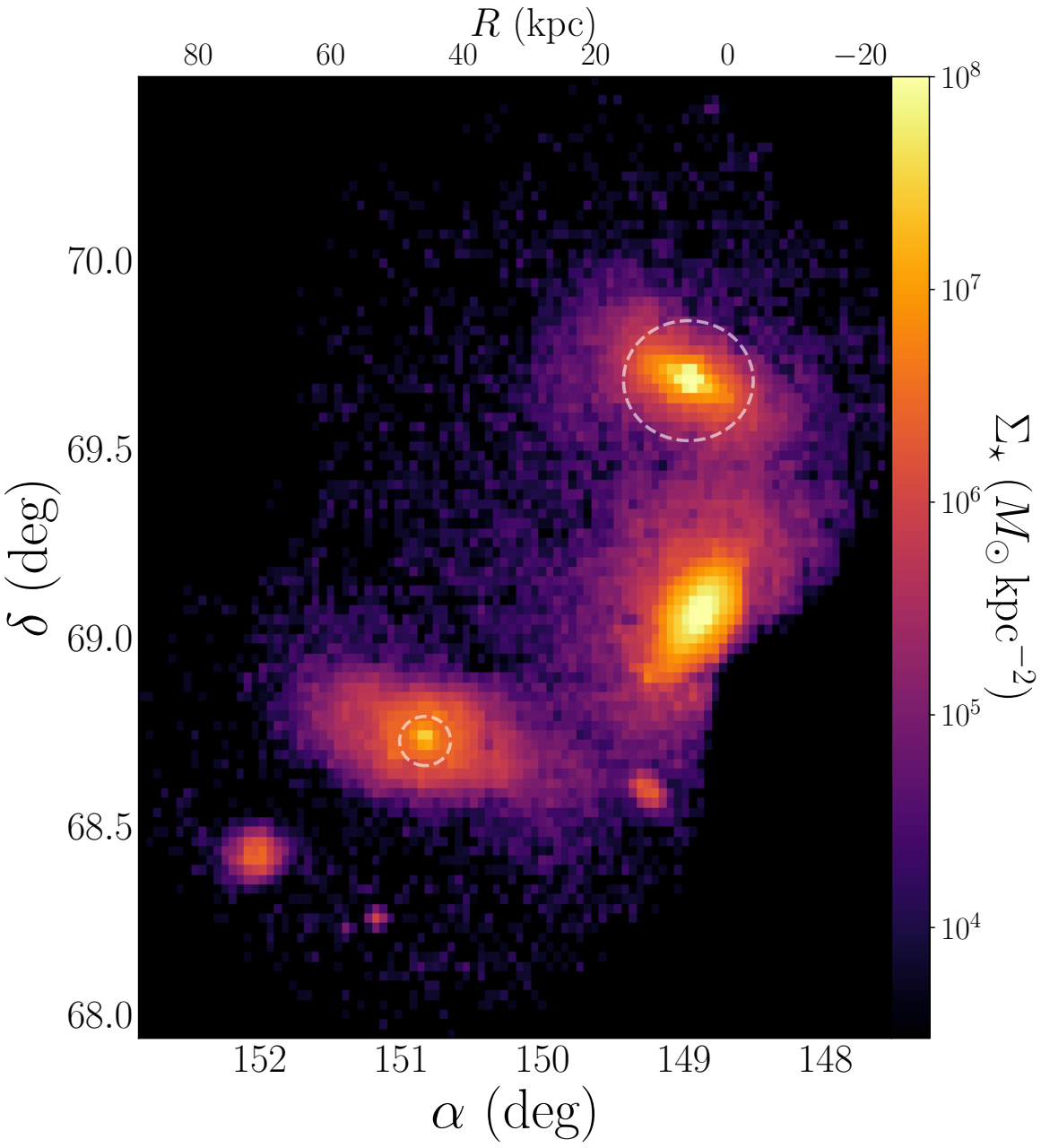

Figure 4.9: Stellar mass density map of the M81 Group. The map has been logarithmically scaled, with each decade in mass color-coded according to the bar on the right. Density was calculated for each $\sim$1 kpc^2 pixel, and converted to stellar mass according to § 4.5 and § 4.6.2.1. The interior regions of M81, M82, and NGC 3077, where the data were too crowded to detect individual stars with Subaru (see Figure 4.8), were filled in using calibrated K_s images from the 2MASS Large Galaxy Atlas (*Jarrett et al.*, 2003), which were re-binned to $\sim$1 kpc physical resolution. The final map was lightly smoothed with a 0.5 kpc Gaussian kernel. The final map spans an impressive four orders of magnitude in mass density. White dashed circles show the estimated tidal radii of M82 and NGC 3077. We count all material outside of these circles as unbound.

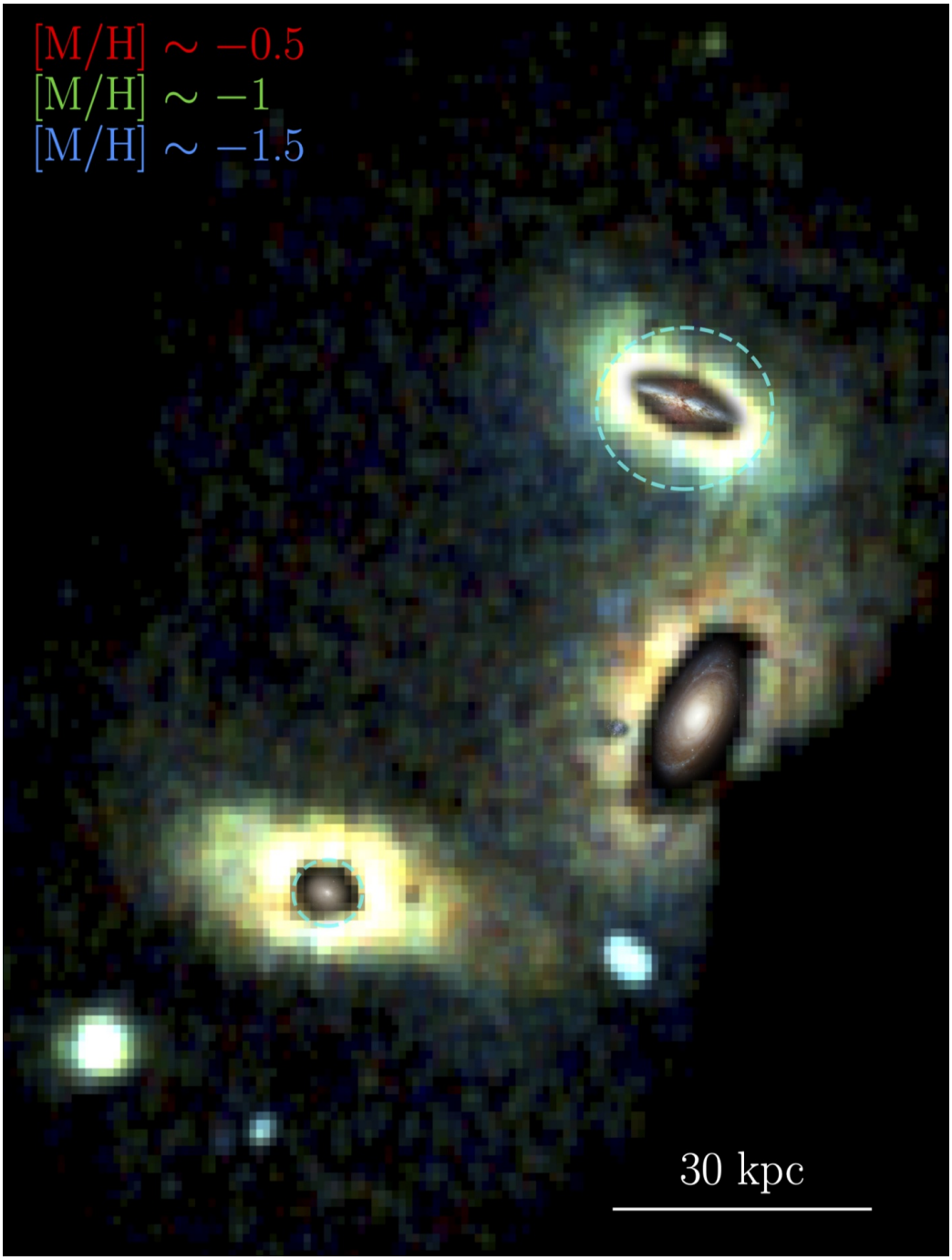

Figure 4.10: Density image of RGB stars, with intensity mapped to stellar density, where each 'channel' represents stars in three bins of metallicity: [Fe/H] ~ -1 (red), [Fe/H] ~ -1 (green), and [Fe/H] ~ -1.5 (blue). Each channel was smoothed using first a tophat filter of size $\sim$20 kpc (to bring out substructure), and then a Gaussian filter of width $\sim$1 kpc. The interiors of M81, M82, and NGC 3077 have been filled with to-scale images from *HST* (credit: NASA, ESA, and the Hubble Heritage Team).

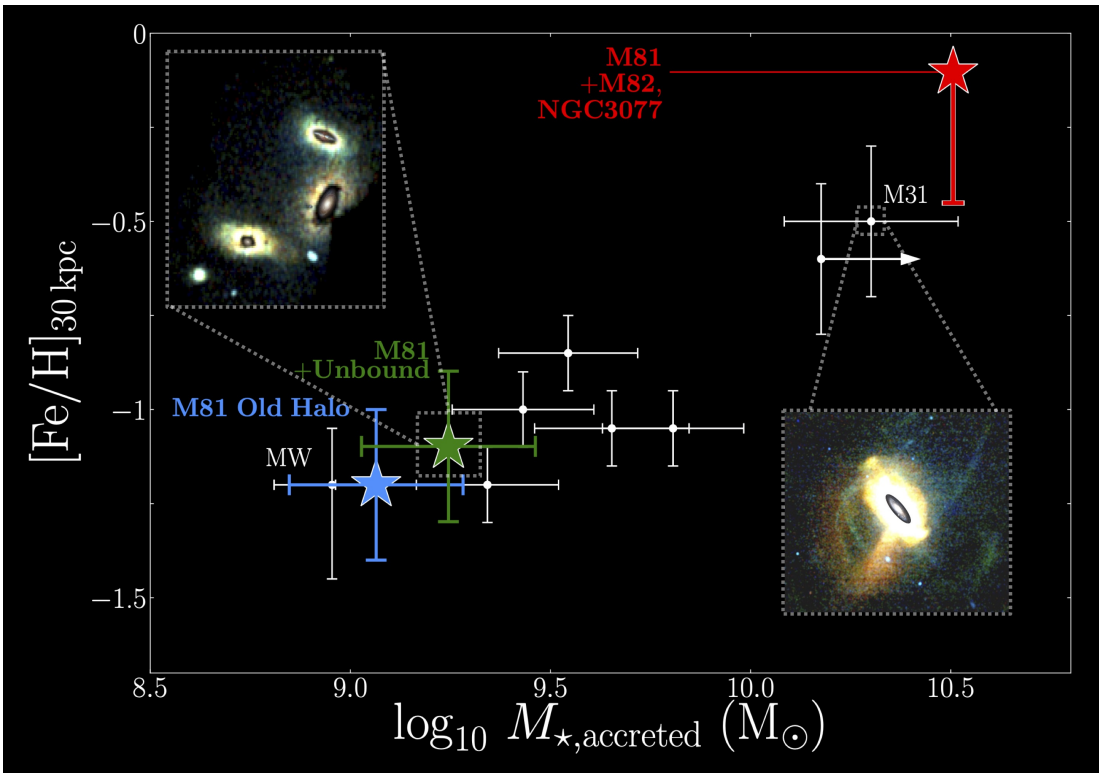

Figure 4.11: The stellar halo mass–metallicity relation. Total accreted mass ($M_{\star,Acc}$) is plotted against metallicity measured at 30 kpc ($[Fe/H]_{30\,kpc}$). The evolution of M81's stellar halo is shown at three points (large stars): (1) its past accretion history (**blue**), measured from the minor axis (see § 4.6.1.1 & 4.6.1.2), (2) its 'current' halo (**green**), accounting for unbound tidal debris around M82 and NGC 3077 (see § 4.6.2.2), and (3) its estimated properties following the accretion of M82 and NGC 3077 (**red**; see § 4.7.2). For comparison, nearby galaxies (taken from *Bell et al.* 2017) are shown in white; the MW and M31 are labeled separately, to highlight their opposite positions on the relation. The MW's stellar halo mass and metallicity are taken from *Mackereth and Bovy* (2020) and *Conroy et al.* (2019), respectively. We adopt 50% larger error bars than intially reported for each, to reflect the substantial spread from other measurements (e.g., *Bell et al.*, 2008; *Deason et al.*, 2019). Metallicity-coded channel density maps are shown as zoomed insets for both M81 (e.g., see Figure 4.10) and M31 (PAndAS; *Martin et al.* 2013) as visual guides of M81's potential halo evolution. For points (1) and (2) we adopt 50% uncertainties on total accreted mass and 0.2 dex uncertainties on metallicity, following *Harmsen et al.* (2017). For (3), the large error in metallicity indicates our uncertainty about the final metallicity gradient of the halo. In this case, the red star assumes the central metallicities for both M82 and NGC 3077 (mass-weighted), while the error bar shows the impact of assuming a steep halo metallicity gradient such as observed in M31 (*Gilbert et al.*, 2014). Dominated by the accreted material from M82, M81's halo will be transformed from low-mass and metal-poor, to a massive and metal-rich halo, rivaling that of M31.

CHAPTER V

A Link Between Satellite Populations and Merger History

5.1 Introduction

In our current Λ–Cold Dark Matter (ΛCDM) paradigm, galaxies assemble hierarchically (e.g., *White and Rees*, 1978). Through this hierarchical growth, they accrete extensive populations of lower-mass 'dwarf' galaxies, while also experiencing frequent mergers with galaxies of all masses, some of which are cataclysmic in their impact on the central galaxy (e.g., *Barnes and Hernquist*, 1991). Modern cosmological simulations, built on a ΛCDM framework, are now able to reproduce many of the large-scale properties of galaxies, such as the galaxy luminosity function (e.g., *Bell et al.*, 2003), galaxy scaling relations (e.g., Kennicutt-Schmidt star formation relation, *Kennicutt* 1998; Tully-Fisher relation, *Tully and Fisher* 1977), and the cosmic star formation rate (SFR; *Madau et al.* 1998). Yet, the regime of small-scale galaxy formation has remained a 'problem-area' for models, mostly due to both physical and time resolution limitations, as stellar feedback can operate on both extremely small spatial and short time scales. Thus, a model-based link between small- and large-scale galaxy formation has thus far proved elusive.

Of the elements of this hierarchical picture of galaxy formation and evolution,

dwarf galaxies are among the most important. Difficult to detect observationally, owing to their intrinsic faintness, dwarf galaxies are both the lowest-mass and most dark matter-dominated galaxies in the Universe (e.g., see the recent review by *Wechsler and Tinker*, 2018). As such, these small galaxies are the observational bedrock of our understanding of small-scale cosmology, and their properties are critical benchmarks for our models of galaxy formation (e.g., see the recent review by *Bullock and Boylan-Kolchin*, 2017). While they are predicted to also exist in isolation, until recently nearly all of the low-mass dwarf galaxies readily accessible to us are 'satellites' of Milky Way (MW)-mass galaxies (e.g., see *McConnachie*, 2012, for an overview of the Local Group satellite populations) — existing within an environment which is dominated by the central galaxy. Galaxies like the MW are not closed boxes — they are complex ecosystems which frequently experience substantial mergers with other such systems throughout their lives.

Recent evidence from the Local Group suggests that this may be an important component in the lives of satellites. Studies of the MW's satellites using *Gaia* data postulate that a number of its satellites may have been brought in during the infall of the Large Magellanic Cloud system (e.g., *Gaia Collaboration et al.*, 2018). Additionally, deep star formation histories of M31's satellites now reveal that nearly 50% share a common 'shutdown' time — $\sim$6 Gyr ago (*Weisz et al.*, 2019). This is approximately coincident with the first infall of the massive galaxy whose merger with M31 likely formed M31's massive stellar halo (*D'Souza and Bell*, 2018b). It seems as though the merger histories of the MW and M31 may have helped to shape their satellite populations.

Meanwhile, recent evidence suggests that the satellite populations of nearby MW-mass galaxies are significantly more diverse than currently predicted in galaxy formation simulations (e.g., *Smercina et al.* 2018, also Chapter III; *Bennet et al.* 2019), and that these galaxies' merger histories are equally diverse (*Harmsen et al.*, 2017; *Bell*

et al., 2017; *D'Souza and Bell*, 2018a; *Smercina et al.*, 2019, also Chapter IV). Thus, while neither the MW's satellites nor its merger history are 'typical' of galaxies at its mass scale, it serves as the benchmark for our understanding of both. Understanding possible relationships between galaxy merger histories and their satellite populations represents an important new avenue to test theoretical models of galaxy formation. Addressing this requires an empirical test of whether or not a direct correlation exists between these two fundamental galactic components. *How do mergers impact galactic satellite populations?*

5.2 Background

Addressing the question of how galaxy mergers may impact the evolution of the satellite populations around MW-mass galaxies requires measurement of two notoriously difficult-to-measure properties: (1) complete satellite populations, and (2) merger history. Efforts to study both of these properties for MW-mass systems have remained a substantial focus of the field. However, they have been historically kept in separate 'intellectual boxes'. In this paper, we have combined these insights to ask the question: how do mergers impact galactic satellites? In this section we summarize the current insight regarding the satellites (§ 5.2.1) and merger histories (§ 5.2.2) of nearby MW-mass galaxies.

5.2.1 The Diverse Satellite Population of MW-mass Galaxies

Understanding the origin of the MW's satellite population has been a field-wide effort for the last two decades. Tensions in the number and properties of observed MW satellites, relative to model predictions — e.g., the 'Missing Satellites' and 'Too Big to Fail' problems (*Klypin et al.*, 1999; *Moore et al.*, 1999; *Boylan-Kolchin et al.*, 2011) — constitute some of the most pressing problems for the ΛCDM paradigm (e.g., *Bullock and Boylan-Kolchin*, 2017). Solutions to these problems — often focusing on

the impact of baryonic processes such as reionization (e.g., *Bullock et al.*, 2001) and stellar feedback (e.g., *Brooks et al.*, 2013) — have used the satellite population of the MW as a benchmark. *Identically one system* has been used to direct the scope of some of the most important problems in galaxy formation.

Motivated by this potential 'house of cards', the field's focus has shifted to surveying the satellite populations of nearby MW-analogs (i.e. central galaxies in the Local Volume with stellar mass $M_\star \sim 3$–$10\times10^{10}\,M_\odot$), to help place the MW in context. The fruits of these efforts? Seven MW-mass ecosystems have now been surveyed to the depth of the MW's 'classical' satellite population ($M_V \lesssim -9$): the MW and M31 (compiled by *McConnachie*, 2012), M81 (compiled by *Karachentsev and Kudrya*, 2014), M101 (*Danieli et al.*, 2017; *Bennet et al.*, 2019), Centaurus A (*Crnojević et al.*, 2019), M94 (*Smercina et al.*, 2018), and M83 (e.g., *Müller et al.*, 2015b, 2017; *Carrillo et al.*, 2017).

With this newfound access to a true sample of satellite populations in MW-like galactic systems has come the realization that these populations are far more diverse than expected. The sparse satellite population of the 'lonely giant' M94 constitutes a powerful constraint: drawing on standard models of galaxy formation, M94 should not exist (*Smercina et al.*, 2018). Its overall paucity of satellites, coupled with its lack of any satellite above 10^6 in stellar mass challenges all current galaxy formation simulations. Combined with the discovery of additional sparse satellite populations, such as M101 and M83, the overall diversity of satellite populations is in tension with model predictions. Figure 5.1 shows the satellite V-band luminosity functions within 150 kpc projected galactic radius for the seven MW-mass galaxies which have been studied down to $M_V \lesssim -9$.

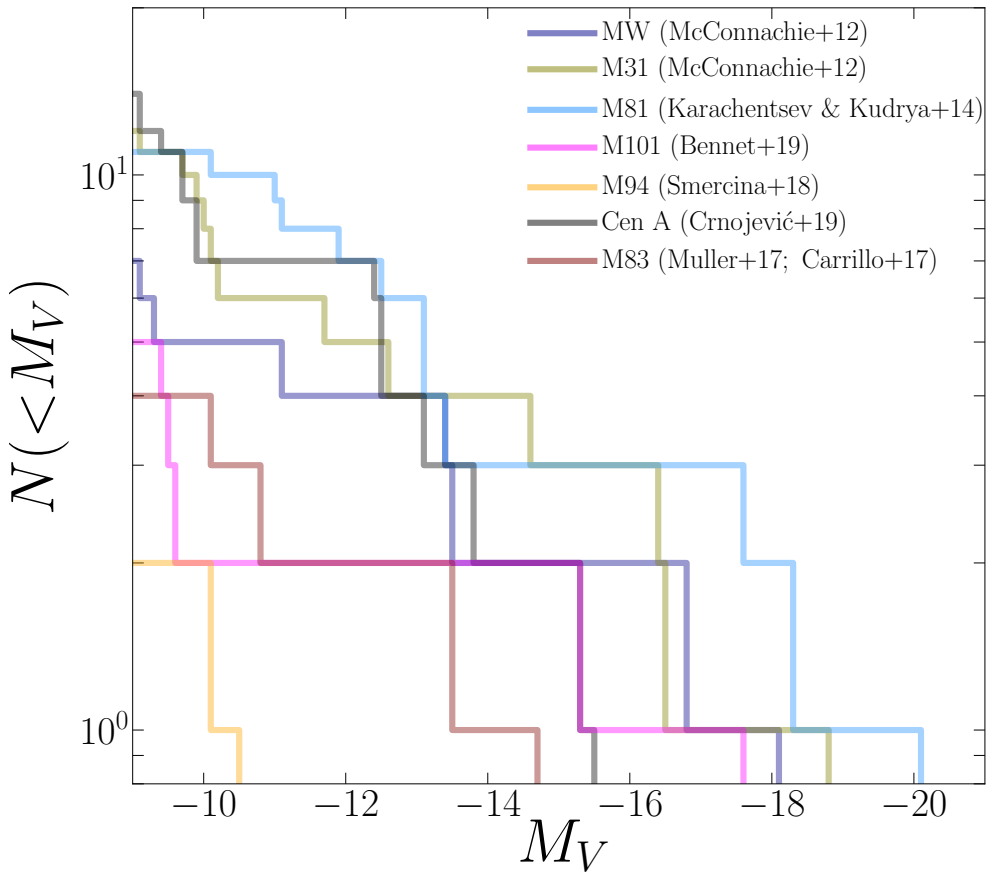

Figure 5.1: Cumulative V-band satellite luminosity functions, within a projected 150 kpc galactic radius, for the seven MW-mass systems which appear to be complete to $M_V \lesssim -9$ (i.e. 'classical' satellites). Adapted and from *Smercina et al.* (2018) and updated with recent work. Highlighted particularly well by the sparse satellite population of the 'lonely giant' M94, these seven systems showcase a broad diversity in the satellite populations of galaxies at the MW-mass scale.

5.2.2 Inferring a Galaxy's Most Dominant Merger from its Stellar Halo Properties

With near-equal vigor to the efforts to study the satellite populations of MW-analogs, there has been a significant push to extract information about these galaxies' merger histories. Motivated by insight from galaxy formation models, suggesting that MW-mass galaxies likely experience diverse merger histories (e.g., *Bullock and Johnston*, 2005), such efforts have sought to use the stellar halos of these galaxies as probes of past merger events. Long studied as ambiguous repositories of extended, and often metal-poor, stellar populations, comparisons between the observed properties of MW-analogs' stellar halos and galaxy formation models suggests that stellar halos are primarily composed of the disrupted remnants of accreted satellites (e.g., *Harmsen et al.*, 2017; *D'Souza and Bell*, 2018a).

Further, models predict that the measurable properties of these accreted stellar populations are often dominated by the most massive merger the central has experienced (e.g., *Deason et al.*, 2015b; *D'Souza and Bell*, 2018a; *Monachesi et al.*, 2019). Recent detailed studies of the halos of M31 (*D'Souza and Bell*, 2018b) and M81 (*Smercina et al.*, 2019) support this picture. Since the stellar mass present in the stellar halo is primarily accreted from the largest merger partner, the measured accreted mass is approximately equivalent to the stellar mass of the dominant progenitor galaxy. Samples of galaxies for which stellar halo properties have been well-measured now exist (e.g., *Merritt et al.*, 2016; *Monachesi et al.*, 2016a; *Harmsen et al.*, 2017). The results of these surveys indicate: (1) that the stellar halos of MW-mass galaxies are diverse, forming a crude-but-powerful stellar halo mass–metallicity relation (*Harmsen et al.*, 2017), and (2) that this diversity must be primarily driven by the properties of the most dominant merger these galaxies have experienced.

Figure 5.2 shows the inferred total accreted stellar mass plotted against inferred photometric metallicity measured at 30 kpc along the minor axis for 13 galaxies in the

Local Volume for which both properties have been measured (or have robust limits). Total accreted stellar mass has been estimated for each galaxy, following *Harmsen et al.* (2017), by integrating the star count-scaled projected 2-D density profile in the range of 10–40 kpc and multiplying by a factor of 3 — obtained from comparisons to the models of *Bullock and Johnston* (2005). The metallicity at 30 kpc is inferred from the minor axis average metallicity profile of the resolved stellar populations, obtained from stellar population modeling.

5.3 Comparing Galaxies' Most Dominant Mergers with their Satellite Populations

5.3.1 Observations

Through these heroic efforts in both the fields of satellite galaxy and stellar halo surveys, the field now has access to a sample of MW-analogs for which both components have been well-measured. This sample of seven systems — the MW, M31, M81, Cen A, M101, M94, and M83 — constitutes our first opportunity to explore possible connections between these two important predictions of the CDM model.

First, we will define several quantities which will be used in this analysis. Following *Smercina et al.* (2018), the 'satellite populations', $N_{\rm Sat}$, of these seven galaxies will include all satellites within a projected galactic radius of 150 kpc and down to an absolute V-band magnitude of $M_V < -9$. Though some of the surveys cover a wider area, are slightly deeper, or both, all seven systems are considered complete within these cuts on radius and luminosity. Uncertainties are then assessed on the total number of satellites within these criteria. We estimate a 20% uncertainty on the number of satellites, reflecting both modest survey incompleteness (based on artificial satellite galaxies; e.g., *Smercina et al.* 2018, *Bennet et al.* 2019), and occasional misclassification of foreground/background dwarf galaxies due to uncertain distances

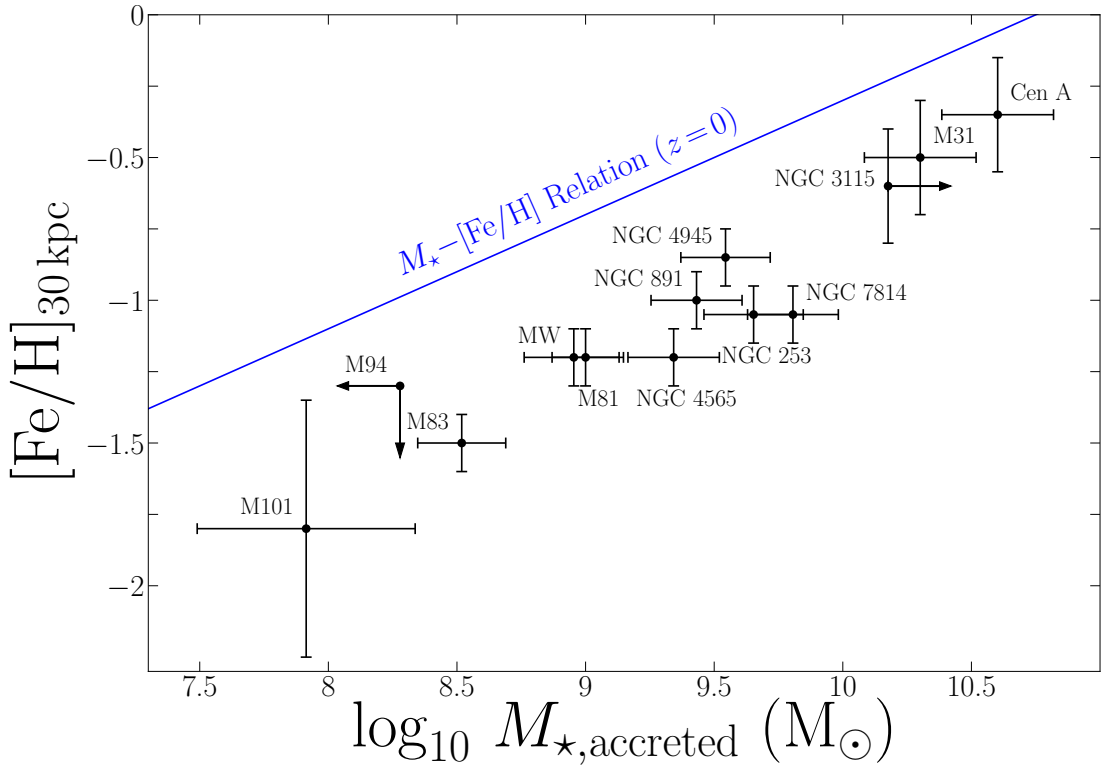

Figure 5.2: The stellar halo mass–metallicity relation for 13 nearby galaxies. Total accreted mass ($M_{\star,\mathrm{accreted}}$), estimated following *Harmsen et al.* (2017) (see text), is plotted against metallicity measured at 30 kpc ($[\mathrm{Fe/H}]_{30\,\mathrm{kpc}}$). The data were compiled from *Rejkuba et al.* (2014), *Monachesi et al.* (2016a), *Harmsen et al.* (2017), *Bell et al.* (2017), *D'Souza and Bell* (2018b), *Conroy et al.* (2019), *Deason et al.* (2019), *Smercina et al.* (2019), *Jang et al.* (2020) and *Bell et al., in prep.* The lower limit on NGC 3115's total accreted mass was taken from *Bell et al.* (2017), and the limits on M94's accreted mass and metallicity were assessed from data that will be presented in *Smercina et al., in prep.* The $z = 0$ stellar mass–metallicity relation (*Gallazzi et al.*, 2005; *Kirby et al.*, 2013) is shown in blue for reference. The broad range of stellar halo properties displayed here — three orders of magnitude in mass and nearly two dex in metallicity — indicate a broad range in the mergers these galaxies have experienced.

from the tip of the red giant branch (TRGB). We adopt a higher uncertainty of 50% for M83, given the lack of a single, cohesive strategy for surveying its satellites.

Next, we follow *D'Souza and Bell* (2018a) in taking the total accreted stellar mass, estimated from stellar halo measurements, as the mass estimate of the most dominant merger that galaxy has experienced. However, following *Smercina et al.* (2019), in systems such as M81, while currently experiencing a dominant merger with the massive M82, the merger is not advanced enough to have redistributed the accreted material into the stellar halo. The estimate of M81's accreted mass, measured along its minor axis, is $\sim$1/20 of its total accreted mass, represented mostly by the mass of M82. We instead adopt a revised metric for the mass of the largest merger, $M_{\rm Dom}$, where this mass is *either* the total accreted mass estimated from the stellar halo, *or* the mass of the most massive satellite within 150 kpc — whichever is larger. This revised definition of $M_{\rm Dom}$ impacts nearly half of the sample, across a wide range (e.g., M101, MW, and M81).

Figure 5.3 (top panel) shows $M_{\rm Dom}$ plotted against $N_{\rm Sat}$ for the seven available MW-mass systems. A strong relationship is visible, with the systems that have experienced the largest mergers hosting the most satellites. The data return a Pearson rank correlation coefficient of 0.98 when including the M94 limit, and 0.97 if excluded — both indicating highly-correlated data. What is the nature of this relationship? Are merger events responsible for bringing fresh satellites into the system?

5.3.2 Comparison to Galaxy Formation Simulations

CDM is self-similar (e.g., *White and Rees*, 1978), and thus hierarchical build-up of structure is predicted. All dark matter halos should contain their own subhalos, thus satellite galaxies should host their own populations of satellites prior to infall. There has been some recent evidence of 'satellites-of-satellites' in both the Local Group and around M81 (e.g., *Deason et al.*, 2014, 2015a; *Smercina et al.*, 2017; *Dooley*

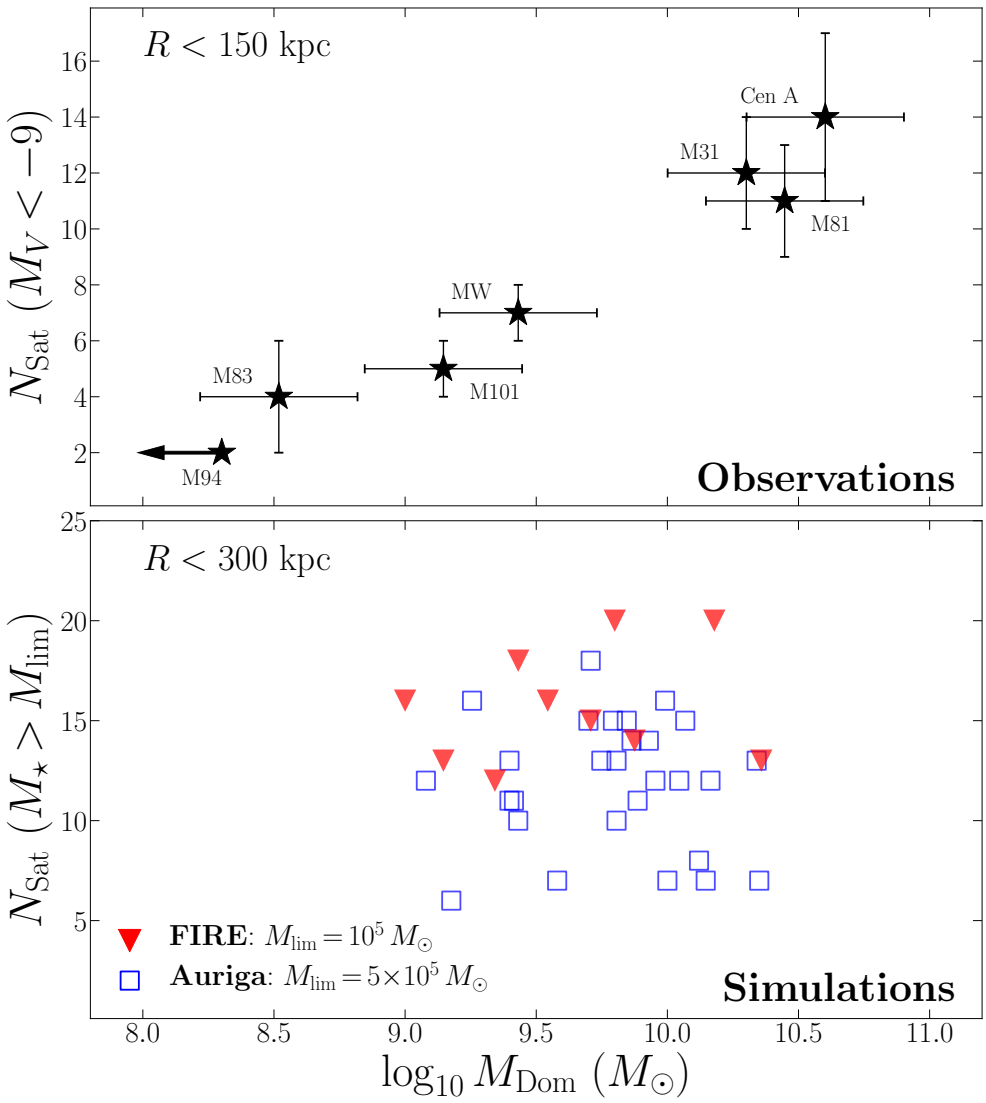

Figure 5.3: **Top**: Total number of 'classical' satellites, within 150 kpc projected radius, around each of seven nearby MW-mass galaxies, plotted against the mass of the most dominant merger they have experienced (see § 5.3.1). Uncertainties of 0.3 dex have been assumed for $M_{\rm Dom}$, following *Harmsen et al.* (2017), *Bell et al.* (2017), and *D'Souza and Bell* (2018a). An upper limit is estimated for M94, which displays little-to-no observable stellar halo (*Smercina et al., in-prep*). A 20% uncertainty has also been estimated for the total number of satellites, accounting for modest survey incompleteness or misclassification of foreground/background dwarf galaxies. We adopt a 50% uncertainty on satellite number for M83. A clear and decisive relationship is visible. **Bottom**: MW-mass systems taken from the Auriga and FIRE simulations, showing the mass of their most dominant merger plotted against the total number of simulated satellites ($M_\star > 10^5\,M_\odot$) within 300 kpc projected radius (*Simpson et al.*, 2018; *Sanderson et al.*, 2018; *Monachesi et al.*, 2019; *Garrison-Kimmel et al.*, 2019a). No relationship is visible, yet there are clear and differences between the two simulations. The stark contrast between the observed systems and the results from these high-resolution hydrodynamic simulations may represent a fundamental gap in our understanding of galaxy formation.

et al., 2017). In this paradigm, in the absence of baryons, the number of surviving subhalos within a central halo should be some monotonic function of the mass of the largest halo the central has accreted, not to mention the mass of the central halo itself. However, the baryonic physics, involving infalling satellites' interactions with circumgalactic gas, tidal disruption by the central galaxy, and internal stellar feedback, complicates matters significantly (e.g., *Wetzel et al.*, 2015). Testing whether or not the relationship between merger history and satellite populations shown in Figure 5.3 is predicted in current galaxy formation theory requires simulations that: (1) can produce realistic dwarf galaxy populations in a group environment, even down to low masses, and (2) produce a sample of MW-mass systems with diverse merger histories.

Currently, two fully hydrodynamic, high-resolution galaxy formation simulations meet these criteria: the Feedback in Realistic Environments (FIRE) project (*Hopkins et al.*, 2014), and the Auriga project (*Grand et al.*, 2017). Each simulation has resolved both the satellite galaxy populations (*Simpson et al.*, 2018; *Garrison-Kimmel et al.*, 2019a) and stellar halo properties (*Sanderson et al.*, 2018; *Monachesi et al.*, 2019) of a sample of MW-mass galaxies, with total virial masses approximately between $8{\times}10^{11}\,M_{\odot}$–$2{\times}10^{12}\,M_{\odot}$. The simulated satellite populations differ from the observed sample in that they are reported within 300 kpc 3-D radius, rather than 150 kpc projected. We use 300 kpc for this work also, as projection effects should not be a substantial source of error (see *Smercina et al.*, 2018) and *Samuel et al.* (2020) report little diversity in the radial profiles, at least in FIRE. Additionally, FIRE and Auriga achieve slightly different resolutions. While FIRE reports satellite statistics down to $M_{\star} > 10^5\,M_{\odot}$, Auriga only resolves satellites to $M_{\star} > 5{\times}10^5\,M_{\odot}$. As tidal destruction is highly resolution-dependent, this difference in mass resolution is likely worth considering when comparing the results of the two simulations.

In the bottom panel of Figure 5.3 we show the mass of the most dominant merger

plotted against the number of satellites within 300 kpc with stellar mass above either $10^5\,M_\odot$ (FIRE) or $5{\times}10^5\,M_\odot$ (Auriga). We adopt the same metric for the mass of the dominant merger as in § 5.3. One potential limitation of this comparison is that accreted mass (which we take as $M_{\rm Dom}$ for galaxies without larger satellites) is directly measured in the simulations, while the estimate for observed galaxies is a model-informed inferred quantity. A more direct comparison would use measurement of stellar mass from 10–40 kpc along the minor axis of the simulated galaxies, as is done in observed systems. However, this is an involved independent project (see *D'Souza and Bell*, 2018a) and the results of *Harmsen et al.* (2017) suggest that, while relatively large, the uncertainties on total accreted mass from the stellar halo measurements are robust to any reasonable range of mass distributions and still much smaller than the range of estimated $M_{\rm Dom}$ (see Figure 5.3).

Unlike the observations, little-to-no relationship is visible for either simulation. Pearson rank correlation coefficients return comparable results, with a weak coefficient of 0.21 for the FIRE systems and -0.04 for Auriga, indicating a lack of correlation. Moreover, the range of both dominant mergers and satellite populations is significantly less than observed, for both simulations. There are some interesting differences between the simulations, particularly in the distribution of both satellite populations and dominant mergers. However, the lack of a correlation in both is robust to these differences and, thus, is a powerful statement on the ability of our flagship models to accurately produce galactic systems.

5.4 This Unexpected Relationship Presents a Challenge for Galaxy Formation

CDM predicts the hierarchical buildup of structure, and thus that the build up accreted material and satellite populations should be related. Yet, with increasing

resolution and recent improvements which incorporate baryonic processes, current standard galaxy formation models predict little-to-no relationship between a MW-mass system's satellite population and its merger history (e.g., FIRE & Auriga; see Figure 5.3, bottom). This suggests that other factors present in the complexity of simulated galaxy formation physics are more important in regulating the satellite populations of galaxies at the MW-mass scale. However, surprisingly this is not what we see in the Universe. For the first time, we have compiled a sample of MW-mass systems for which both the most dominant mergers and satellite galaxy populations have been robustly measured. The result is an unexpectedly tight correlation between the mass of the most dominant merger the galaxies' have experienced and the number of satellites they host.

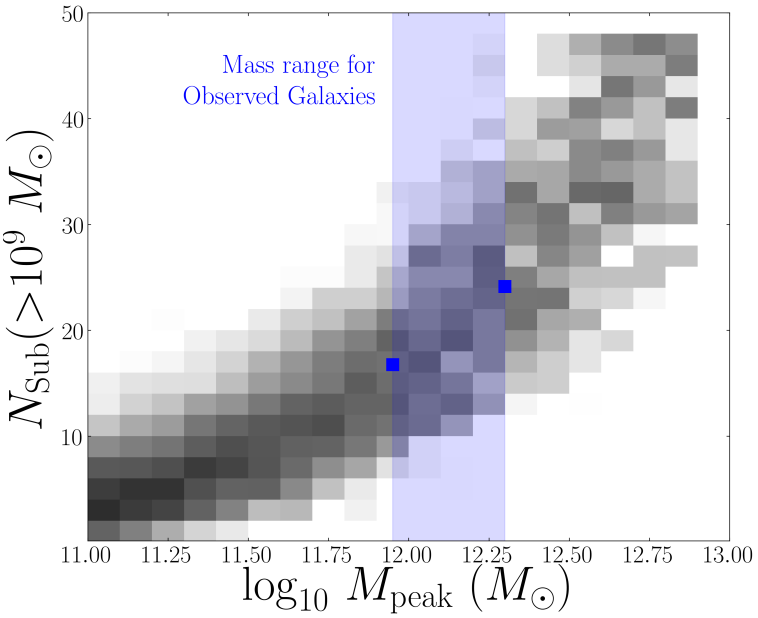

Figure 5.4: A 2-D histrogram showing the peak (virial) masses of 10,334 central galaxies in the EAGLE simulation (*Schaye et al.*, 2015), plotted against the total number of subhalos with virial masses $>10^9\,M_\odot$ within 150 kpc radius of each. The estimated halo mass range for the seven galaxies shown in Figure 5.3 is highlighted in blue. The average total number of $>10^9\,M_\odot$ subhalos at is shown for halos at each end of this mass range, denoted by blue squares.

There is a possible source of uncertainty encoded in the range of stellar masses in the observed galaxies. The observed seven galaxy sample ranges from approximately

$3\times10^{10}\,M_\odot$ (M94) to $10^{11}\,M_\odot$ (M31, Cen A). Using the stellar mass–halo mass relation (e.g., *Behroozi et al.*, 2013), this corresponds to a halo mass range of $\sim9\times10^{11}\,M_\odot$–$2\times10^{12}\,M_\odot$. This is almost identical to the range of halo masses probed by both FIRE and Auriga (e.g., § 5.3.2), and both simulations also produce a comparable range in stellar mass. In fact, the FIRE `m12z` simulation is an isolated MW-mass galaxy with approximately the mass of M94, yet has substantially more satellites (*Garrison-Kimmel et al.*, 2019a). We better quantify this effect in Figure 5.4, where we show the total number of all satellite subhalos within 150 kpc of all central galaxies in the EAGLE simulation (*Schaye et al.*, 2015), plotted against the virial mass of the central halo. The difference in the average number of subhalos within a $\sim9\times10^{11}\,M_\odot$ halo and $2\times10^{12}\,M_\odot$ halo is only $\sim$30% — 18 and 24, respectively. This suggests that the observations probe a comparable diversity of galaxy/halo properties as the simulations and that differences in halo mass is not the primary driver of the observed satellite–merger relationship. An alternative explanation is that the halo mass range is simply much larger than expected. However, explaining the factor of seven range in total number of satellites would require a halo mass range of $\sim10^{11}\,M_\odot$–$10^{13}\,M_\odot$ for the observed sample of MW-mass galaxies.

Using halo occupation techniques in concert with the Illustris simulation, *Carlsten et al.* (2020) found that nearby galaxies display a positive correlation between stellar mass and number of satellites, albeit with very large scatter. This correlation is a natural outcome of CDM (e.g., Figure 5.4) when combined with the stellar mass–halo mass relation. They argue that halo mass is thus an important factor in explaining the observed diversity in satellite populations. However, this high-scatter correlation, combined with no predicted correlation between $M_{\rm Dom}$ and $M_\star$, cannot explain the tightness of the $N_{\rm Sat}$–$M_{\rm Dom}$ correlation shown in Figure 5.3. In the absence of alternative insight, it appears that mergers help to build galactic satellite populations in a way that our models do not currently predict.

5.5 Conclusions

For the first time, we explored an empirical link between the satellite populations and merger histories of a sample of MW-mass galaxies. Using surveys conducted around seven nearby galaxies, we compared the total number of 'classical' satellites, down to $M_V < -9$, within 150 kpc projected radius of each galaxy with estimates of the mass of the most dominant merger each galaxy has experienced. We note that more than half of these galaxies are *currently* experiencing this dominant merger event, in the form of a massive close satellite. In these cases, we adopt the stellar mass of this most massive satellite as the most dominant merger mass.

In the seven-galaxy sample, we find a strong positive correlation: the more massive its largest merger, the more satellites a galaxy seems to host. The correlation is equally strong whether or not the upper limit from M94's stellar halo is included. We then compare the observed relationship to predictions from the high-resolution FIRE and Auriga hydrodynamic simulations. Surprisingly, neither simulation reproduces any correlation between the number of satellites and largest mergers of the simulated MW-mass systems, despite nearly identical stellar and virial mass ranges for the observed and simulated samples.

Ultimately, this crucial and potentially transformative empirical link between the merger histories of MW-mass galaxies and the buildup of their satellite populations is a powerful observational test of the hierarchical nature of galaxy formation. The inability of the current highest-resolution galaxy formation simulations to reproduce this relationship represents an acute shortcoming of the theoretical framework upon which our current galaxy formation paradigm is built.

CHAPTER VI

Coda

6.1 Summary

The MW and M31 are host to substantial populations of dwarf satellite galaxies (e.g., *McConnachie*, 2012) and each possess stellar halos, which encode details of their merger histories (e.g., *Bell et al.*, 2008; *Ibata et al.*, 2014) — two of the central predictions in the hierarchical model of CDM. In addition to numerous differences in the properties of the galaxies themselves, including morphology and star formation history, M31 appears to host a much richer satellite population, and to have experienced a much more massive and recent merger (e.g., *D'Souza and Bell*, 2018b), than the MW (e.g., *Helmi et al.*, 2018). Despite these clear differenecs, the satellites and stellar halos of the MW and M31 serve as benchmarks for our understanding of galaxy assembly in the CDM model. Long-standing questions regarding the observed properties of dwarf galaxies, as well as the role of merger history in galaxy evolution, have largely been addressed using *only these two systems* — a fragile foundation for galaxy formation.

Recent insight from model–observation comparison underlines the precariousness of this lack of context. Current galaxy formation simulations predict substantial diversity in both the satellites (e.g., *Simpson et al.*, 2018; *Garrison-Kimmel et al.*, 2019a,b) and merger histories (e.g., *Monachesi et al.*, 2016b; *D'Souza and Bell*, 2018a)

of MW-mass galaxies. Yet, recent surveys, attempting to reduce the observational deficit around other systems, indicate that these models may not be capturing the full range of either (e.g., *Spencer et al.*, 2014; *Geha et al.*, 2017; *Harmsen et al.*, 2017).

This work uses new observations of the satellite populations and stellar halos of several nearby galaxies, along with careful comparisons to galaxy formation models, to bridge this knowledge gap of how the Local Group's assembly compares to other galaxies of similar mass. This began with the realization that deep, wide-field observations with the Subaru Hyper Suprime-Cam (HSC) of nearby galaxy outskirts could detect dwarf galaxies fainter than nearly any survey to-date (Chapter II). This newfound technical insight enabled a new approach to the question: *is the MW representative of galaxies at its mass scale and how might the answer impact our understanding of galaxy formation?*

To address this, a survey of the satellite population of the nearby MW-mass galaxy M94 was conducted with Subaru HSC (Chapter III). Reaching out to 150 kpc in projected radius, this deep survey was sensitive to all dwarf galaxies in the 'classical' regime ($M_V < -9$). Surprisingly, only two low-mass satellites were detected. Artificial satellite testing confirmed that these are, indeed, the only two 'classical' satellites within 150 kpc of M94, in contrast with the MW's seven and M31's 12 within the same radius. Detailed comparisons of M94's sparse satellite population with the EAGLE simulation were conducted. Using a 'standard' model of halo occupation, it was found that: (1) M94's satellite population is in considerable tension with current galaxy formation models, and moreover the observed diversity in the satellite populations of MW-mass galaxies is considerably larger than current models predict (e.g., *Garrison-Kimmel et al.*, 2019a), and (2) M94's satellite population is much better represented by a more 'stochastic' halo occupation model, suggesting that the scatter in galaxy formation even at intermediate halo masses $M_h \sim 10^{10}$ may be more stochastic than predicted in current models, which use the MW as a benchmark.

The characteristics which make Subaru HSC perhaps the best existing for detecting faint satellites around nearby galaxies — its large mirror, wide field-of-view, and excellent seeing — also make it an outstanding instrument for the study of stellar halos. With the same dataset used in Chapter II, a survey of the stellar halo of M81 was conducted (Chapter IV). M81 is in an unusual evolutionary stage, having recently begun a significant interaction with its massive satellite M82, as well as the lower-mass NGC 3077. Using deep point-source photometry of individual red giant branch (RGB) stars, along with exquisite overlapping archival *HST* fields, M81's stellar halo, and its triple-interaction, was revealed in never-before-seen detail. Using the deepest-ever census of stellar mass in a stellar halo outside of the Local Group, M81's stellar halo properties were estimated at three points: (1) its ancient halo, representing its past accretion history, measured along its minor axis, (2) its 'current' halo, which incorporates unbound debris from its two interacting satellites, M82 and NGC 3077, and (3) its future halo, following the accretion and incorporation of all stellar material from M82 and NGC 3077. These three distinct evolutionary stages show a dramatic evolution of M81's stellar halo properties throughout its current merger, quickly transforming from one of the least massive and metal-poorest halos around a MW-mass galaxy to one of the most massive and metal-rich — rivaling the halo of M31. This dramatic transformation of M81's halo is powerful evidence that the observed diversity in stellar halo properties (e.g., *Harmsen et al.*, 2017) is primarily driven by diversity in the largest mergers these galaxies have experienced.

Lastly, Chapter V combines the insight gained in Chapter III & IV, as well as the numerous other recent studies of the satellite populations and stellar halos of nearby MW-mass galaxies. For the first time, a possible link between satellite populations and merger history is explored — two principal components of the CDM model. A strong correlation was found between the mass of the most dominant merger experienced and the total number of 'classical' satellites in a compiled sample of seven

nearby MW-mass galaxies. Moreover, comparison with two of the current highest-resolution galaxy formation simulations, FIRE (*Hopkins et al.*, 2014) and Auriga (*Grand et al.*, 2017), finds completely disparate results. Neither simulation shows any discernible relationship between these same quantities, despite covering a nearly identical stellar mass range (and therefore, presumably, virial mass range) as the observed galaxy sample. The inability of current flagship galaxy formation simulations to reproduce this relationship represents an urgent knowledge gap in the theoretical framework upon which our current galaxy formation paradigm is built.

6.2 Ongoing Work & Outlook

The stellar halos and satellite galaxy populations of MW-mass galaxies represent some of the most stringent tests of the CDM model, and of galaxy formation in general. This dissertation has worked to shore-up the fragile foundation to our understanding of these galactic components, which until recently, was grounded entirely on the Local Group. Both the satellite populations and stellar halos of nearby galaxies have been found to be incredibly diverse, the former inexplicably so, and a newfound, powerful correlation between satellite populations and merger history completely defies model predictions.

Much of my future work will involve further exploring these discoveries in the context of galaxy evolution. Several important gaps still exist in our understanding of external galactic systems: (1) the detection and properties of ultra-faint dwarf galaxies outside of the Local Group, and (2) a complete census of the 'classical' satellite populations of and dominant mergers experienced by MW-mass galaxies in the Local Volume.

6.2.1 Detecting Ultra-Faint Dwarfs in the Local Volume

Despite the considerable advancement in our understanding of the satellite populations of other nearby MW-mass galaxies, and the surprises they have held (e.g., Chapter III & V), there exists a regime of galaxy formation which remains completely unexplored outside of the Local Group. No ultra-faint dwarf (UFD) galaxy has yet been detected, which is not a MW or M31 satellite. As discussed in Chapter I, these UFDs ($M_\star \lesssim 10^5\,M_\odot$; $M_V \lesssim -8$) are completely distinct from other 'normal' dwarf galaxies, with most forming the majority of their stellar mass by redshift of 10 (*Brown et al.*, 2014; *Weisz et al.*, 2014). High-resolution galaxy formation simulations, such as FIRE, are just beginning to be able to resolve galaxies at these kinds of stellar masses (e.g., *Garrison-Kimmel et al.*, 2019a). Yet, observationally, we have absolutely no understanding about how these UFD populations vary from system to system beyond the MW and M31. Are surprises in store, with nearby UFD examples that are inexplicable in our current models, as is the case with the 'classical' satellites of M94 (Chapter III)?

Building on the detection of d1005+68 around M81, among the faintest galaxies ever detected outside of the Local Group (Chapter II), the observational techniques used in this dissertation may be the best current method of addressing this knowledge gap. Resolving stellar populations, as we have done with Subaru HSC, is the *only way UFDs can be robustly detected*. As shown in Figure 2.4, most of the MW's UFDs are incredibly low surface brightness ($\mu_V > 29\,\mathrm{mag\,arcsec^{-2}}$), and possess small half-light radii. Surveys able to reach these depths in integrated light, such as Dragonfly (e.g., *Danieli et al.*, 2018) will require deep point-source photometric follow-up to confirm any candidates.

In work conducted alongside this dissertation and the presented M81 and M94 observations, we have compiled a complete, deep resolved-star dataset of the outskirts of an additional nearby MW-mass system, M83, with at least four future programs

planned for M64, NGC 253, M51, and NGC 4258. I have begun working on methods to expand our ability to detect even fainter dwarf galaxies in our existing and planned Subaru HSC observations, including the development of artificial star and artificial galaxy architecture, which will be crucial for quantifying the completeness of our satellite surveys. This artificial galaxy testing indicates that complete UFD populations down to at least $M_V < -6$ should be accomplishable with Subaru HSC, and other comparable ground-based, wide-field imagers, for all systems within 7 Mpc. This would allow, for the first time, robust comparison between a diverse sample of UFD populations and those produced in galaxy formation models like FIRE. This is summarized in Figure 6.1, showing the substantial UFD discovery space within the Local Volume.

Combining the seven existing satellite surveys, some of which will require further ground-based follow-up, with our four new planned Subaru HSC surveys, will result in a sample of 11 MW-mass systems for which their UFD populations have been surveyed. The upcoming Rubin Observatory Legacy Survey of Space and Time (LSST) will further revolutionize this science, surveying all MW-mass galaxies in the Local Volume and the Southern half of the night sky. Though LSST is due to begin its science in 2022, it will not achieve comparable depth to our HSC datasets until at least 2030. Following close on the heels of LSST, the Nancy Grace Roman Space Telescope (*RST*; formerly *WFIRST*) will launch, providing *HST* image quality over a 100× larger field-of-view — a further 'game-changer' for UFD discovery in the Local Volume. The ability to interpret LSST's and *RST*'s observations in the context of satellite populations, as well as direct the galaxy formation models which will produce robust predictions ahead of their full scientific outputs, will require a deep existing observational training set. Once compiled, the sample of 11 MW-mass galactic systems discussed here will serve as the *intellectual foundation* for studies of the satellite populations of MW-like systems for the next decade, and beyond.

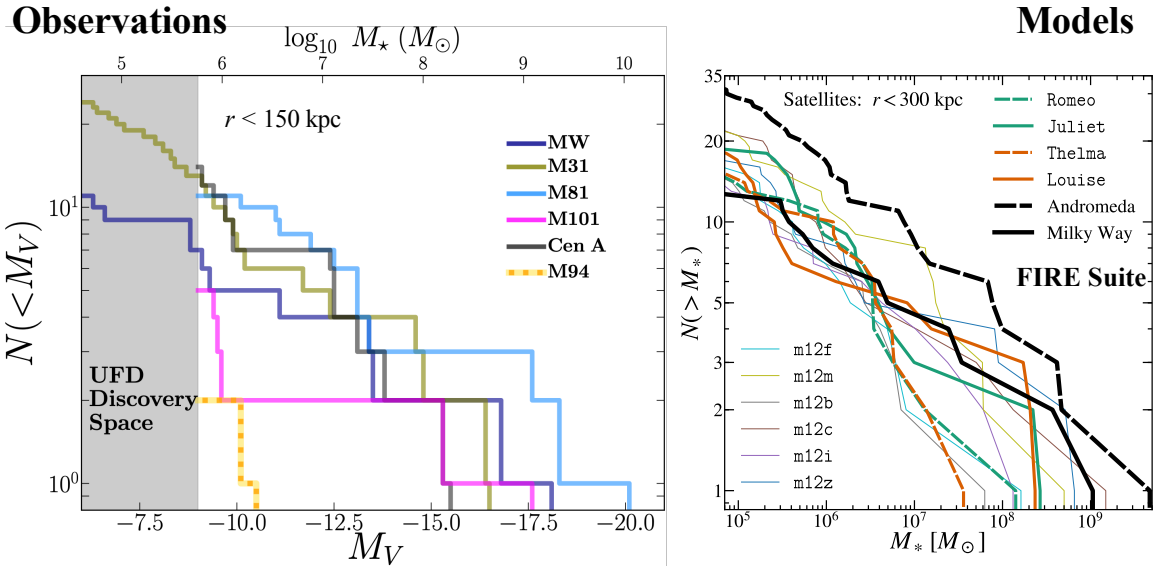

Figure 6.1: Left: Cumulative V-band luminosity functions of 'classical' satellites ($M_V < -9$) within 150 kpc projected radius for four nearby MW-mass systems. The satellite luminosity functions of the MW and M31 are also shown, but extending down to $M_V < -6$ — the ultra-faint regime. Corresponding stellar mass is shown along the top axis. The discovery space for ultra-faints in the nearby universe ($\lesssim$5–6 kpc) using ground-based telescopes is shown in gray. Right: Satellite stellar mass functions of MW-mass galaxies in the FIRE simulations (*Garrison-Kimmel et al.*, 2019a), which extend to $M_\star < 10^5\,M_\odot$, into the UFD regime and below detection threshold in current observations of any galaxies other than the MW and M31. Instruments like Subaru HSC provide a tremendous and important opportunity to study this unexplored regime of galaxy formation throughout the nearby universe — crucial groundwork leading into the LSST era.

6.2.2 Exploring the Merger–Satellite Connection in Additional Systems

Thus far, the important new insights presented in Chapter V into the surprising relationship between the satellite populations and merger histories of nearby MW-mass galaxies is based on 7 well-studied MW-mass systems, including the MW and M31 — a small sample. We have barely scratched the surface of the near-field galaxy population, an effort which will be revolutionized by the likes of next-generation instruments such as LSST and *RST*. As in the case of UFD populations, directing these future efforts, in the context of these new satellite-focused revelations, will require a large, well-studied pilot sample of galaxies in the Local Volume. The same

four systems which are accessible to Subaru HSC for UFD discovery — M64, NGC 253, M51, and NGC 4258 — are also prime candidates for resolving their stellar halos.

I plan to use the techniques developed and refined as part of this dissertation to estimate the stellar halo properties, and thus dominant merger properties, of all four of these MW-mass systems, as well as M83 and M94 using our existing Subaru HSC datasets. Though not yet complete, these datasets show immense promise. M94, for example, appears to have an unusually low-mass, anemic stellar halo (see Figure 5.2), comparable to the halo of M101 (*Jang et al.*, 2020). Did this largely secular existence somehow contribute to its current sparse satellite population? Furthermore, data for one of the proposed galaxies is already in hand. In a first-semester 2019 program, one full-depth Subaru HSC field (of six) was observed around M64 in all three planned filters (the rest of the observations were not scheduled due to weather). Though the survey of M64 is far from complete, in this single field we observe a massive, metal-rich, shell-like tidal feature in resolved RGB stars, shown in Figure 6.2. Owing to its morphology, this feature was likely created during a very recent merger event (e.g., *Johnston et al.*, 2008). In fact, this recent merger may have been responsible for the formation of M64's counter-rotating gas disk (*Braun et al.*, 1992) — unique in the nearby universe.

With this complete set of both satellite populations and detailed stellar halo maps of MW-mass ecosystems in-hand, more detailed metrics can be developed to explore the satellite–merger relationship. A large fraction of M31's satellites show evidence of having responded globally during M31's massive merger (see § 5.1; *Weisz et al.*, 2019), suggesting that satellites brought in during merger exhibit distinct signatures. Measuring recent star formation histories for the satellites in other systems currently experiencing massive mergers, such as M81 and M51, will help build much-needed intuition about which of these satellites are 'new' to the system. This can be done with resolved stellar populations with *HST*, as well as spectroscopic follow-up. In concert

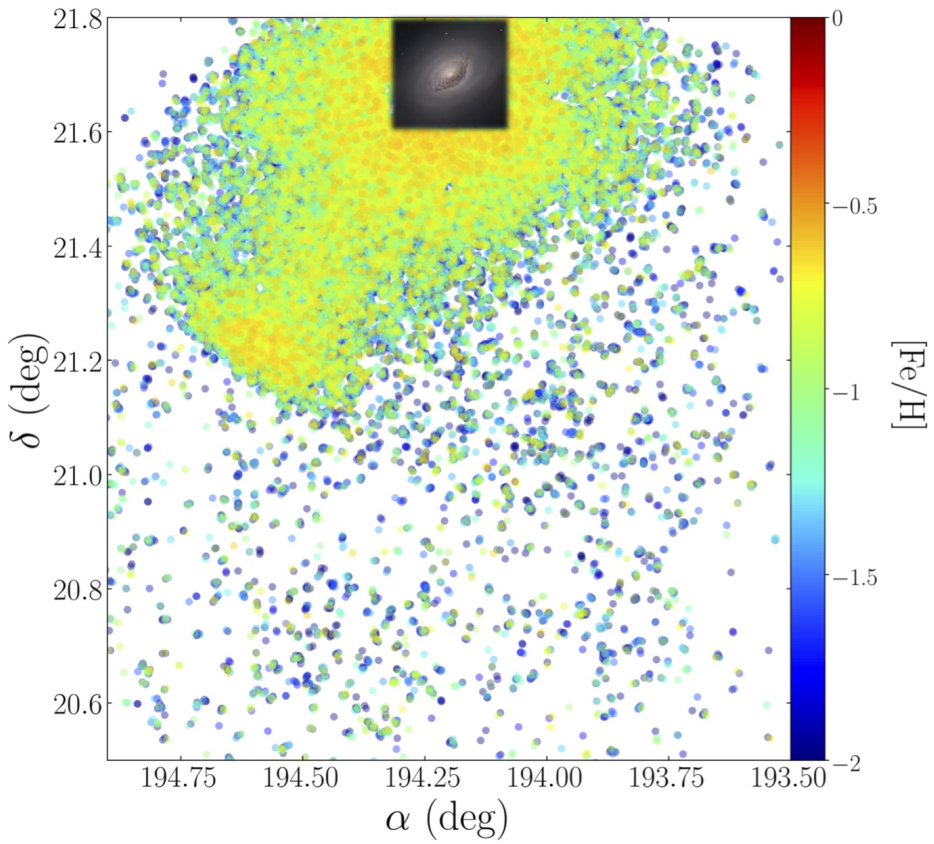

Figure 6.2: Map of resolved RGB stars in the stellar halo of M64, in the single existing Subaru HSC field with three-filter coverage from our 2019A program. Stars are color-coded by inferred photometric metallicity. Never-before-resolved, M64's stellar halo shows a spectacular metal-rich tidal feature, with a distinctive shell morphology, suggesting a recent accretion event (*Johnston et al.*, 2008). This recent merger could be the origin of M64's unique counter-rotating gas disk (e.g., *Braun et al.*, 1992). M64 is only the latest exemplar of the efficacy of wide-field resolved-star studies of stellar halos in deciphering the merger histories of nearby galaxies.

with estimates of recent star formation activity, these spectroscopic observations can be used to measure line-of-sight (LOS), or radial, velocities, which may be powerful metrics of which satellites may have been recently accreted. If large numbers of satellites were accreted during a recent merger, they may retain kinematic memory of this previous association, with a bulk angular momentum axis that aligns with the accreted material from the merger (e.g., *Johnston et al.*, 2008). There is some tentative evidence for this approach in the coherently rotating 'plane' of satellites around Cen A, which are aligned with the major axis of its stellar halo (*Crnojević*

et al., 2016; *Müller et al.*, 2018).

In addition to observational progress, careful and detailed comparisons to galaxy formation models will be absolutely critical to understand this unexpected satellite–merger relation. While these simulations currently fail to reproduce the observed correlation presented in Chapter V, they do produce galactic systems that are strikingly similar to those observed in the universe. Figure 6.3 shows a side-by-side comparison of the metallicity-coded stellar halo density map of M31 measured by PAndAS (*Martin et al.*, 2013) and of a comparable MW-mass galaxy simulated in FIRE. The two images are nearly indistinguishable. One of the strengths of such high-fidelity simulations, such as FIRE, is the ability to change the input physics. While standard models typically choose the optimal overall set of inputs to match a host of broad, observed universal properties (e.g., galactic structure, galaxy luminosity function, observed power spectrum), there still exists the powerful functionality to explore the impact of different recipes for physical processes on specific observables (e.g., *Kim et al.*, 2014; *Terrazas et al.*, 2020).

Making use of this flexibility could allow investigations of: (1) how many satellites are brought into the central ecosystem during mergers and what happens to them; under which conditions, if any, do systems which experience large mergers have larger satellite populations, as is observed? (2) Do satellite populations in simulated systems display the same enhanced star formation signatures during large mergers as observed systems? And, (3) which physical parameters can, or must, we change in the simulations to better reproduce the relationship between satellites and merger history? Such detailed comparisons to the simulations will serve to ground the observed relationship in a physics-motivated context.

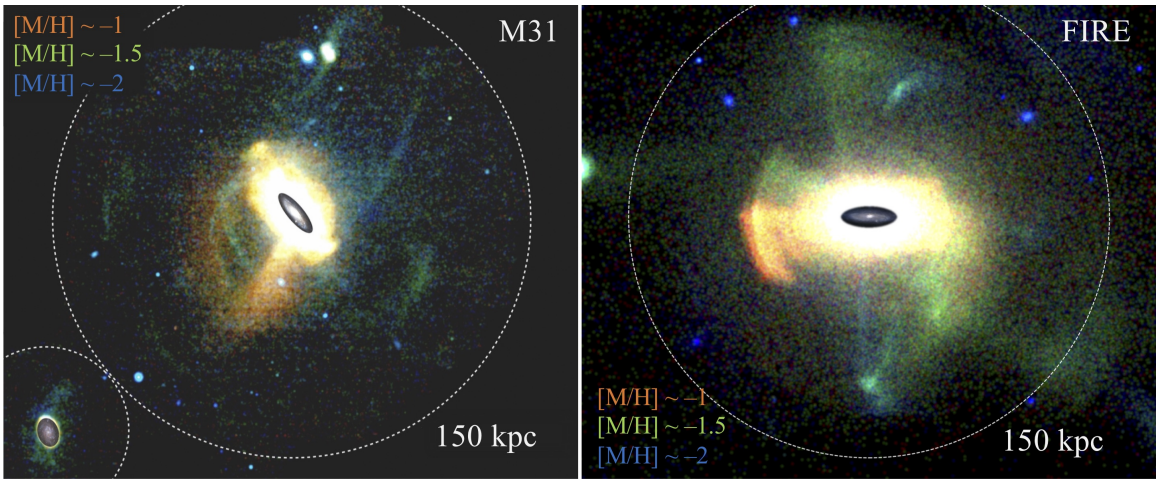

Figure 6.3: Metallicity-coded stellar mass density channel maps of the halo of M31 (left; *Martin et al.* 2013), and the simulated FIRE galaxy m12f (right; a new representation, assembled using the data of *Sanderson et al.* 2018). Red corresponds to $[\mathrm{M/H}] \sim -0.5$, green to $[\mathrm{M/H}] \sim -1$, and blue to $[\mathrm{M/H}] \sim -1.5$. Numerous faint satellites are visible in each. The m12f map showcases the incredible similarity between observed and FIRE-simulated stellar halo measurements, and satellite populations, of MW-mass ecosystems. These simulations are a necessary tools to make detailed comparisons with the current and future observational evidence of the satellite–merger relationship.

BIBLIOGRAPHY

BIBLIOGRAPHY

Abraham, R. G., and P. G. van Dokkum (2014), Ultra-Low Surface Brightness Imaging with the Dragonfly Telephoto Array, *PASP*, *126*(935), 55, doi:10.1086/674875.

Aguerri, J. A. L., M. Balcells, and R. F. Peletier (2001), Growth of galactic bulges by mergers. I. Dense satellites, *A&A*, *367*, 428–442, doi:10.1051/0004-6361:20000441.

Armandroff, T. E., E. W. Olszewski, and C. Pryor (1995), The Mass-To-Light Ratios of the Draco and Ursa Minor Dwarf Spheroidal Galaxies.I. Radial Velocities from Multifiber Spectroscopy, *AJ*, *110*, 2131, doi:10.1086/117675.

Armus, L., et al. (2009), GOALS: The Great Observatories All-Sky LIRG Survey, *PASP*, *121*(880), 559, doi:10.1086/600092.

Axelrod, T., J. Kantor, R. H. Lupton, and F. Pierfederici (2010), An open source application framework for astronomical imaging pipelines, in *Software and Cyberinfrastructure for Astronomy*, *Proc. SPIE*, vol. 7740, p. 774015, doi:10.1117/12.857297.

Baade, W., and E. Hubble (1939), The New Stellar Systems in Sculptor and Fornax, *PASP*, *51*(299), 40, doi:10.1086/124994.

Bailin, J., E. F. Bell, S. N. Chappell, D. J. Radburn-Smith, and R. S. de Jong (2011), The Resolved Stellar Halo of NGC 253, *ApJ*, *736*, 24, doi:10.1088/0004-637X/736/1/24.

Barnes, J. E., and L. E. Hernquist (1991), Fueling Starburst Galaxies with Gas-rich Mergers, *ApJ*, *370*, L65, doi:10.1086/185978.

Baugh, C. M., S. Cole, and C. S. Frenk (1996), Evolution of the Hubble sequence in hierarchical models for galaxy formation, *MNRAS*, *283*(4), 1361–1378, doi:10.1093/mnras/283.4.1361.

Bechtol, K., et al. (2015), Eight New Milky Way Companions Discovered in First-year Dark Energy Survey Data, *ApJ*, *807*, 50, doi:10.1088/0004-637X/807/1/50.

Behroozi, P. S., R. H. Wechsler, and C. Conroy (2013), The Average Star Formation Histories of Galaxies in Dark Matter Halos from z = 0-8, *ApJ*, *770*, 57, doi:10.1088/0004-637X/770/1/57.

Bell, E. F., D. H. McIntosh, N. Katz, and M. D. Weinberg (2003), The Optical and Near-Infrared Properties of Galaxies. I. Luminosity and Stellar Mass Functions, *ApJS*, *149*(2), 289–312, doi:10.1086/378847.

Bell, E. F., X. X. Xue, H.-W. Rix, C. Ruhland, and D. W. Hogg (2010), Stellar Population Variations in the Milky Way's Stellar Halo, *AJ*, *140*, 1850–1859, doi:10.1088/0004-6256/140/6/1850.

Bell, E. F., A. Monachesi, B. Harmsen, R. S. de Jong, J. Bailin, D. J. Radburn-Smith, R. D'Souza, and B. W. Holwerda (2017), Galaxies Grow Their Bulges and Black Holes in Diverse Ways, *ApJ*, *837*, L8, doi:10.3847/2041-8213/aa6158.

Bell, E. F., et al. (2008), The Accretion Origin of the Milky Way's Stellar Halo, *ApJ*, *680*, 295–311, doi:10.1086/588032.

Bellazzini, M., F. R. Ferraro, and E. Pancino (2001), A Step toward the Calibration of the Red Giant Branch Tip as a Standard Candle, *ApJ*, *556*, 635–640, doi:10.1086/321613.

Belokurov, V., M. J. Irwin, S. E. Koposov, N. W. Evans, E. Gonzalez-Solares, N. Metcalfe, and T. Shanks (2014), ATLAS lifts the Cup: discovery of a new Milky Way satellite in Crater, *MNRAS*, *441*, 2124–2133, doi:10.1093/mnras/stu626.

Belokurov, V., et al. (2006), A Faint New Milky Way Satellite in Bootes, *ApJ*, *647*, L111–L114, doi:10.1086/507324.

Belokurov, V., et al. (2007), Cats and Dogs, Hair and a Hero: A Quintet of New Milky Way Companions, *ApJ*, *654*(2), 897–906, doi:10.1086/509718.

Bennet, P., D. J. Sand, D. Crnojević, K. Spekkens, A. Karunakaran, D. Zaritsky, and B. Mutlu-Pakdil (2019), The M101 Satellite Luminosity Function and the HaloHalo Scatter among Local Volume Hosts, *ApJ*, *885*(2), 153, doi:10.3847/1538-4357/ab46ab.

Benson, A. J., C. G. Lacey, C. M. Baugh, S. Cole, and C. S. Frenk (2002), The effects of photoionization on galaxy formation - I. Model and results at z=0, *MNRAS*, *333*(1), 156–176, doi:10.1046/j.1365-8711.2002.05387.x.

Berlind, A. A., et al. (2003), The Halo Occupation Distribution and the Physics of Galaxy Formation, *ApJ*, *593*(1), 1–25, doi:10.1086/376517.

Bosch, J., et al. (2018), The Hyper Suprime-Cam software pipeline, *PASJ*, *70*, S5, doi:10.1093/pasj/psx080.

Boylan-Kolchin, M., J. S. Bullock, and M. Kaplinghat (2011), Too big to fail? The puzzling darkness of massive Milky Way subhaloes, *MNRAS*, *415*, L40–L44, doi:10.1111/j.1745-3933.2011.01074.x.

Braun, R., R. A. M. Walterbos, and J. Kennicutt, Robert C. (1992), Counter-rotating gaseous disks in the "Evil Eye" galaxy NGC4826, *Nature*, *360*, 442–444, doi:10.1038/360442a0.

Bressan, A., P. Marigo, L. Girardi, B. Salasnich, C. Dal Cero, S. Rubele, and A. Nanni (2012), PARSEC: stellar tracks and isochrones with the PAdova and TRieste Stellar Evolution Code, *MNRAS*, *427*, 127–145, doi:10.1111/j.1365-2966.2012.21948.x.

Brooks, A. M., M. Kuhlen, A. Zolotov, and D. Hooper (2013), A Baryonic Solution to the Missing Satellites Problem, *ApJ*, *765*, 22, doi:10.1088/0004-637X/765/1/22.

Brown, T. M., et al. (2014), The Quenching of the Ultra-faint Dwarf Galaxies in the Reionization Era, *ApJ*, *796*(2), 91, doi:10.1088/0004-637X/796/2/91.

Bruzual, G., and S. Charlot (2003), Stellar population synthesis at the resolution of 2003, *MNRAS*, *344*, 1000–1028, doi:10.1046/j.1365-8711.2003.06897.x.

Bullock, J. S., and M. Boylan-Kolchin (2017), Small-Scale Challenges to the ΛCDM Paradigm, *ARA&A*, *55*, 343–387, doi:10.1146/annurev-astro-091916-055313.

Bullock, J. S., and K. V. Johnston (2005), Tracing Galaxy Formation with Stellar Halos. I. Methods, *ApJ*, *635*, 931–949, doi:10.1086/497422.

Bullock, J. S., A. V. Kravtsov, and D. H. Weinberg (2001), Hierarchical Galaxy Formation and Substructure in the Galaxy's Stellar Halo, *ApJ*, *548*, 33–46, doi:10.1086/318681.

Caldwell, N., T. E. Armandroff, G. S. Da Costa, and P. Seitzer (1998), Dwarf elliptical galaxies in the M81 Group - The structure and stellar populations of BK5N and F8D1, *AJ*, *115*, 535, doi:10.1086/300233.

Carlin, J. L., et al. (2016), First Results from the MADCASH Survey: A Faint Dwarf Galaxy Companion to the Low-mass Spiral Galaxy NGC 2403 at 3.2 Mpc, *ApJ*, *828*, L5, doi:10.3847/2041-8205/828/1/L5.

Carlsten, S. G., J. E. Greene, A. H. G. Peter, R. L. Beaton, and J. P. Greco (2020), Luminosity Functions and Host-to-Host Scatter of Dwarf Satellite Systems in the Local Volume, *arXiv e-prints*, arXiv:2006.02443.

Carollo, D., T. C. Beers, M. Chiba, J. E. Norris, K. C. Freeman, Y. S. Lee, Ž. Ivezić, C. M. Rockosi, and B. Yanny (2010), Structure and Kinematics of the Stellar Halos and Thick Disks of the Milky Way Based on Calibration Stars from Sloan Digital Sky Survey DR7, *ApJ*, *712*, 692–727, doi:10.1088/0004-637X/712/1/692.

Carrillo, A., E. F. Bell, J. Bailin, A. Monachesi, R. S. de Jong, B. Harmsen, and C. T. Slater (2017), Characterizing dw1335-29, a recently discovered dwarf satellite of M83, *MNRAS*, *465*, 5026–5032, doi:10.1093/mnras/stw3025.

Cautun, M., A. J. Deason, C. S. Frenk, and S. McAlpine (2019), The aftermath of the Great Collision between our Galaxy and the Large Magellanic Cloud, *MNRAS*, *483*(2), 2185–2196, doi:10.1093/mnras/sty3084.

Chabrier, G. (2001), The Galactic Disk Mass Budget. I. Stellar Mass Function and Density, *ApJ*, *554*(2), 1274–1281, doi:10.1086/321401.

Chabrier, G. (2003), Galactic Stellar and Substellar Initial Mass Function, *PASP*, *115*, 763–795, doi:10.1086/376392.

Chen, Y., A. Bressan, L. Girardi, P. Marigo, X. Kong, and A. Lanza (2015), PARSEC evolutionary tracks of massive stars up to 350 M at metallicities 0.0001 $\leq Z \leq$0.04, *MNRAS*, *452*, 1068 − −1080, *doi* : 10.1093/*mnras*/*stv*1281.

Chiboucas, K., I. D. Karachentsev, and R. B. Tully (2009), Discovery of New Dwarf Galaxies in the M81 Group, *AJ*, *137*, 3009–3037, doi:10.1088/0004-6256/137/2/3009.

Chiboucas, K., B. A. Jacobs, R. B. Tully, and I. D. Karachentsev (2013), Confirmation of Faint Dwarf Galaxies in the M81 Group, *AJ*, *146*, 126, doi:10.1088/0004-6256/146/5/126.

Clowe, D., A. Gonzalez, and M. Markevitch (2004), Weak-Lensing Mass Reconstruction of the Interacting Cluster 1E 0657-558: Direct Evidence for the Existence of Dark Matter, *ApJ*, *604*(2), 596–603, doi:10.1086/381970.

Conroy, C., R. P. Naidu, D. Zaritsky, A. Bonaca, P. Cargile, B. D. Johnson, and N. Caldwell (2019), Resolving the Metallicity Distribution of the Stellar Halo with the H3 Survey, *arXiv e-prints*, arXiv:1909.02007.

Conselice, C. J., K. Bundy, R. S. Ellis, J. Brichmann, N. P. Vogt, and A. C. Phillips (2005), Evolution of the Near-Infrared Tully-Fisher Relation: Constraints on the Relationship between the Stellar and Total Masses of Disk Galaxies since z˜1, *ApJ*, *628*(1), 160–168, doi:10.1086/430589.

Crnojević, D., et al. (2016), The Extended Halo of Centaurus A: Uncovering Satellites, Streams, and Substructures, *ApJ*, *823*, 19, doi:10.3847/0004-637X/823/1/19.

Crnojević, D., et al. (2019), The Faint End of the Centaurus A Satellite Luminosity Function, *ApJ*, *872*(1), 80, doi:10.3847/1538-4357/aafbe7.

Dalcanton, J. J., et al. (2012), The Panchromatic Hubble Andromeda Treasury, *ApJS*, *200*(2), 18, doi:10.1088/0067-0049/200/2/18.

Dalcanton, J. J., et al. (2015), The Panchromatic Hubble Andromeda Treasury. VIII. A Wide-area, High-resolution Map of Dust Extinction in M31, *ApJ*, *814*(1), 3, doi:10.1088/0004-637X/814/1/3.

Danieli, S., P. van Dokkum, A. Merritt, R. Abraham, J. Zhang, I. D. Karachentsev, and L. N. Makarova (2017), The Dragonfly Nearby Galaxies Survey. III. The Luminosity Function of the M101 Group, *ApJ*, *837*, 136, doi:10.3847/1538-4357/aa615b.

Danieli, S., P. van Dokkum, and C. Conroy (2018), Hunting Faint Dwarf Galaxies in the Field Using Integrated Light Surveys, *ApJ*, *856*(1), 69, doi:10.3847/1538-4357/aaadfb.

Darg, D. W., et al. (2010), Galaxy Zoo: the fraction of merging galaxies in the SDSS and their morphologies, *MNRAS*, *401*(2), 1043–1056, doi:10.1111/j.1365-2966.2009.15686.x.

Davenport, J. R. A., Ž. Ivezić, A. C. Becker, J. J. Ruan, N. M. Hunt-Walker, K. R. Covey, A. R. Lewis, Y. AlSayyad, and L. M. Anderson (2014), The SDSS-2MASS-WISE 10-dimensional stellar colour locus, *MNRAS*, *440*, 3430–3438, doi:10.1093/mnras/stu466.

Davies, R. D., and A. E. Wright (1977), A tidal origin for the Magellanic Stream., *MNRAS*, *180*, 71–88, doi:10.1093/mnras/180.1.71.

de Blok, W. J. G., F. Walter, E. Brinks, C. Trachternach, S. H. Oh, and J. Kennicutt, R. C. (2008), High-Resolution Rotation Curves and Galaxy Mass Models from THINGS, *AJ*, *136*(6), 2648–2719, doi:10.1088/0004-6256/136/6/2648.

de Blok, W. J. G., et al. (2018), A High-resolution Mosaic of the Neutral Hydrogen in the M81 Triplet, *ApJ*, *865*, 26, doi:10.3847/1538-4357/aad557.

de Mello, D. F., L. J. Smith, E. Sabbi, J. S. Gallagher, M. Mountain, and D. R. Harbeck (2008), Star Formation in the H I Bridge Between M81 and M82, *AJ*, *135*(2), 548–554, doi:10.1088/0004-6256/135/2/548.

Deason, A. J., V. Belokurov, and N. W. Evans (2011), The Milky Way stellar halo out to 40 kpc: squashed, broken but smooth, *MNRAS*, *416*, 2903–2915, doi:10.1111/j.1365-2966.2011.19237.x.

Deason, A. J., V. Belokurov, and D. R. Weisz (2015a), The progenitors of the Milky Way stellar halo: big bricks favoured over little bricks., *MNRAS*, *448*, L77–L81, doi:10.1093/mnrasl/slv001.

Deason, A. J., A. R. Wetzel, S. Garrison-Kimmel, and V. Belokurov (2015b), Satellites of LMC-mass dwarfs: close friendships ruined by Milky Way mass haloes, *MNRAS*, *453*(4), 3568–3574, doi:10.1093/mnras/stv1939.

Deason, A. J., V. Belokurov, and J. L. Sanders (2019), The total stellar halo mass of the Milky Way, *MNRAS*, p. 2394, doi:10.1093/mnras/stz2793.

Deason, A. J., et al. (2014), TriAnd and its siblings: satellites of satellites in the Milky Way halo, *MNRAS*, *444*(4), 3975–3985, doi:10.1093/mnras/stu1764.

Dooley, G. A., A. H. G. Peter, T. Yang, B. Willman, B. F. Griffen, and A. Frebel (2017), An observer's guide to the (Local Group) dwarf galaxies: predictions for their own dwarf satellite populations, *MNRAS*, *471*, 4894–4909, doi:10.1093/mnras/stx1900.

Dorman, C. E., et al. (2015), A Clear Age-Velocity Dispersion Correlation in Andromeda's Stellar Disk, *ApJ*, *803*(1), 24, doi:10.1088/0004-637X/803/1/24.

Drlica-Wagner, A., et al. (2015), Eight Ultra-faint Galaxy Candidates Discovered in Year Two of the Dark Energy Survey, *ApJ*, *813*, 109, doi:10.1088/0004-637X/813/2/109.

Drlica-Wagner, A., et al. (2016), An Ultra-Faint Galaxy Candidate Discovered in Early Data from the Magellanic Satellites Survey, *ArXiv e-prints*.

D'Souza, R., and E. F. Bell (2018a), The masses and metallicities of stellar haloes reflect galactic merger histories, *MNRAS*, *474*, 5300–5318, doi:10.1093/mnras/stx3081.

D'Souza, R., and E. F. Bell (2018b), The Andromeda galaxy's most important merger about 2 billion years ago as M32's likely progenitor, *Nature Astronomy*, *2*, 737–743, doi:10.1038/s41550-018-0533-x.

Durrell, P. R., A. Sarajedini, and R. Chandar (2010), Deep HST/ACS Photometry of the M81 Halo, *ApJ*, *718*, 1118–1127, doi:10.1088/0004-637X/718/2/1118.

Eggen, O. J., D. Lynden-Bell, and A. R. Sandage (1962), Evidence from the motions of old stars that the Galaxy collapsed., *ApJ*, *136*, 748, doi:10.1086/147433.

Elias, L. M., L. V. Sales, P. Creasey, M. C. Cooper, J. S. Bullock, R. M. Rich, and L. Hernquist (2018), Stellar halos in Illustris: probing the histories of Milky Way-mass galaxies, *MNRAS*, *479*(3), 4004–4016, doi:10.1093/mnras/sty1718.

Eliche-Moral, M. C., M. Balcells, J. A. L. Aguerri, and A. C. González-García (2006), Growth of galactic bulges by mergers. II. Low-density satellites, *A&A*, *457*(1), 91–108, doi:10.1051/0004-6361:20065394.

Emerick, A., M.-M. Mac Low, J. Grcevich, and A. Gatto (2016), Gas Loss by Ram Pressure Stripping and Internal Feedback from Low-mass Milky Way Satellites, *ApJ*, *826*, 148, doi:10.3847/0004-637X/826/2/148.

Fattahi, A., V. Belokurov, A. J. Deason, C. S. Frenk, F. A. Gómez, R. J. J. Grand , F. Marinacci, R. Pakmor, and V. Springel (2019), The origin of galactic metal-rich stellar halo components with highly eccentric orbits, *MNRAS*, *484*(4), 4471–4483, doi:10.1093/mnras/stz159.

Ferrarese, L., et al. (2016), The Next Generation Virgo Cluster Survey (NGVS). XIII. The Luminosity and Mass Function of Galaxies in the Core of the Virgo Cluster and the Contribution from Disrupted Satellites, *ApJ*, *824*, 10, doi:10.3847/0004-637X/824/1/10.

Fitts, A., et al. (2017), fire in the field: simulating the threshold of galaxy formation, *MNRAS*, *471*, 3547–3562, doi:10.1093/mnras/stx1757.

Font, A. S., et al. (2011), The population of Milky Way satellites in the Λ cold dark matter cosmology, *MNRAS*, *417*, 1260–1279, doi:10.1111/j.1365-2966.2011.19339.x.

Fujimoto, M., and Y. Sofue (1976), Dynamical evolution of the triple system of the Galaxy, the Large and Small Magellanic Clouds., *A&A*, *47*(2), 263–291.

Gaia Collaboration, et al. (2016), The Gaia mission, *A&A*, *595*, A1, doi:10.1051/0004-6361/201629272.

Gaia Collaboration, et al. (2018), Gaia Data Release 2. Summary of the contents and survey properties, *A&A*, *616*, A1, doi:10.1051/0004-6361/201833051.

Gallagher, I., John S., and J. P. Ostriker (1972), A Note on Mass Loss during Collisions between Galaxies and the Formation of Giant Systems, *AJ*, *77*, 288, doi:10.1086/111280.

Gallazzi, A., S. Charlot, J. Brinchmann, S. D. M. White, and C. A. Tremonti (2005), The ages and metallicities of galaxies in the local universe, *MNRAS*, *362*(1), 41–58, doi:10.1111/j.1365-2966.2005.09321.x.

Garrison-Kimmel, S., J. S. Bullock, M. Boylan-Kolchin, and E. Bardwell (2017a), Organized chaos: scatter in the relation between stellar mass and halo mass in small galaxies, *MNRAS*, *464*, 3108–3120, doi:10.1093/mnras/stw2564.

Garrison-Kimmel, S., et al. (2017b), Not so lumpy after all: modelling the depletion of dark matter subhaloes by Milky Way-like galaxies, *MNRAS*, *471*, 1709–1727, doi:10.1093/mnras/stx1710.

Garrison-Kimmel, S., et al. (2019a), The Local Group on FIRE: dwarf galaxy populations across a suite of hydrodynamic simulations, *MNRAS*, *487*(1), 1380–1399, doi:10.1093/mnras/stz1317.

Garrison-Kimmel, S., et al. (2019b), Star formation histories of dwarf galaxies in the FIRE simulations: dependence on mass and Local Group environment, *MNRAS*, *489*(4), 4574–4588, doi:10.1093/mnras/stz2507.

Geehan, J. J., M. A. Fardal, A. Babul, and P. Guhathakurta (2006), Investigating the Andromeda stream - I. Simple analytic bulge-disc-halo model for M31, *MNRAS*, *366*(3), 996–1011, doi:10.1111/j.1365-2966.2005.09863.x.

Geha, M., M. R. Blanton, R. Yan, and J. L. Tinker (2012), A Stellar Mass Threshold for Quenching of Field Galaxies, *ApJ*, *757*, 85, doi:10.1088/0004-637X/757/1/85.

Geha, M., et al. (2017), The SAGA Survey. I. Satellite Galaxy Populations around Eight Milky Way Analogs, *ApJ*, *847*, 4, doi:10.3847/1538-4357/aa8626.

Gilbert, K. M., et al. (2012), Global Properties of M31's Stellar Halo from the SPLASH Survey. I. Surface Brightness Profile, *ApJ*, *760*, 76, doi:10.1088/0004-637X/760/1/76.

Gilbert, K. M., et al. (2014), Global Properties of M31's Stellar Halo from the SPLASH Survey. II. Metallicity Profile, *ApJ*, *796*, 76, doi:10.1088/0004-637X/796/2/76.

Gilbert, K. M., et al. (2018), Global Properties of M31's Stellar Halo from the SPLASH Survey. III. Measuring the Stellar Velocity Dispersion Profile, *ApJ*, *852*, 128, doi:10.3847/1538-4357/aa9f26.

Grand, R. J. J., F. A. Gómez, F. Marinacci, R. Pakmor, V. Springel, D. J. R. Campbell, C. S. Frenk, A. Jenkins, and S. D. M. White (2017), The Auriga Project: the properties and formation mechanisms of disc galaxies across cosmic time, *MNRAS*, *467*(1), 179–207, doi:10.1093/mnras/stx071.

Grogin, N. A., et al. (2011), CANDELS: The Cosmic Assembly Near-infrared Deep Extragalactic Legacy Survey, *ApJS*, *197*(2), 35, doi:10.1088/0067-0049/197/2/35.

Hammer, F., Y. B. Yang, J. L. Wang, R. Ibata, H. Flores, and M. Puech (2018), A 2-3 billion year old major merger paradigm for the Andromeda galaxy and its outskirts, *MNRAS*, *475*, 2754–2767, doi:10.1093/mnras/stx3343.

Harmsen, B., A. Monachesi, E. F. Bell, R. S. de Jong, J. Bailin, D. J. Radburn-Smith, and B. W. Holwerda (2017), Diverse stellar haloes in nearby Milky Way mass disc galaxies, *MNRAS*, *466*, 1491–1512, doi:10.1093/mnras/stw2992.

Helmi, A., and S. D. M. White (1999), Building up the stellar halo of the Galaxy, *MNRAS*, *307*, 495–517, doi:10.1046/j.1365-8711.1999.02616.x.

Helmi, A., C. Babusiaux, H. H. Koppelman, D. Massari, J. Veljanoski, and A. G. A. Brown (2018), The merger that led to the formation of the Milky Way's inner stellar halo and thick disk, *Nature*, *563*, 85–88, doi:10.1038/s41586-018-0625-x.

High, F. W., C. W. Stubbs, A. Rest, B. Stalder, and P. Challis (2009), Stellar Locus Regression: Accurate Color Calibration and the Real-Time Determination of Galaxy Cluster Photometric Redshifts, *AJ*, *138*, 110–129, doi:10.1088/0004-6256/138/1/110.

Homma, D., et al. (2016), A New Milky Way Satellite Discovered In The Subaru/Hyper Suprime-Cam Survey, *ArXiv e-prints*.

Hopkins, P. F., L. Hernquist, T. J. Cox, T. Di Matteo, B. Robertson, and V. Springel (2006), A Unified, Merger-driven Model of the Origin of Starbursts, Quasars, the Cosmic X-Ray Background, Supermassive Black Holes, and Galaxy Spheroids, *ApJS*, *163*(1), 1–49, doi:10.1086/499298.

Hopkins, P. F., K. Bundy, D. Croton, L. Hernquist, D. Keres, S. Khochfar, K. Stewart, A. Wetzel, and J. D. Younger (2010), Mergers and Bulge Formation in ΛCDM: Which Mergers Matter?, *ApJ*, *715*(1), 202–229, doi:10.1088/0004-637X/715/1/202.

Hopkins, P. F., D. Kereš, J. Oñorbe, C.-A. Faucher-Giguère, E. Quataert, N. Murray, and J. S. Bullock (2014), Galaxies on FIRE (Feedback In Realistic Environments): stellar feedback explains cosmologically inefficient star formation, *MNRAS*, *445*(1), 581–603, doi:10.1093/mnras/stu1738.

Hubble, E. P. (1925), Cepheids in spiral nebulae, *The Observatory*, *48*, 139–142.

Ibata, R., M. Irwin, G. Lewis, A. M. N. Ferguson, and N. Tanvir (2001), A giant stream of metal-rich stars in the halo of the galaxy M31, *Nature*, *412*, 49–52.

Ibata, R. A., G. Gilmore, and M. J. Irwin (1994), A dwarf satellite galaxy in Sagittarius, *Nature*, *370*(6486), 194–196, doi:10.1038/370194a0.

Ibata, R. A., et al. (2014), The Large-scale Structure of the Halo of the Andromeda Galaxy. I. Global Stellar Density, Morphology and Metallicity Properties, *ApJ*, *780*, 128, doi:10.1088/0004-637X/780/2/128.

Ivezić, Ž., et al. (2007), Sloan Digital Sky Survey Standard Star Catalog for Stripe 82: The Dawn of Industrial 1% Optical Photometry, *AJ*, *134*(3), 973–998, doi:10.1086/519976.

Jang, I. S., R. S. de Jong, B. W. Holwerda, A. Monachesi, E. F. Bell, and J. Bailin (2020), Tracing the anemic stellar halo of M101, *arXiv e-prints*, arXiv:2001.12007.

Jarrett, T. H., T. Chester, R. Cutri, S. E. Schneider, and J. P. Huchra (2003), The 2MASS Large Galaxy Atlas, *AJ*, *125*, 525–554, doi:10.1086/345794.

Jarrett, T. H., M. E. Cluver, M. J. I. Brown, D. A. Dale, C. W. Tsai, and F. Masci (2019), The WISE Extended Source Catalogue (WXSC) I: The 100 Largest Galaxies, *arXiv e-prints*, arXiv:1910.11793.

Jarrett, T. H., et al. (2012), Constructing a WISE High Resolution Galaxy Atlas, *AJ*, *144*(2), 68, doi:10.1088/0004-6256/144/2/68.

Jarrett, T. H., et al. (2013), Extending the Nearby Galaxy Heritage with WISE: First Results from the WISE Enhanced Resolution Galaxy Atlas, *AJ*, *145*, 6, doi:10.1088/0004-6256/145/1/6.

Jethwa, P., D. Erkal, and V. Belokurov (2016), A Magellanic origin of the DES dwarfs, *MNRAS*, *461*, 2212–2233, doi:10.1093/mnras/stw1343.

Johnston, K. V., J. S. Bullock, S. Sharma, A. Font, B. E. Robertson, and S. N. Leitner (2008), Tracing Galaxy Formation with Stellar Halos. II. Relating Substructure in Phase and Abundance Space to Accretion Histories, *ApJ*, *689*(2), 936–957, doi:10.1086/592228.

Kafle, P. R., S. Sharma, G. F. Lewis, and J. Bland-Hawthorn (2012), Kinematics of the Stellar Halo and the Mass Distribution of the Milky Way Using Blue Horizontal Branch Stars, *ApJ*, *761*, 98, doi:10.1088/0004-637X/761/2/98.

Karachentsev, I. D., and Y. N. Kudrya (2014), Orbital Masses of Nearby Luminous Galaxies, *AJ*, *148*, 50, doi:10.1088/0004-6256/148/3/50.

Karachentsev, I. D., A. Dolphin, R. B. Tully, M. Sharina, L. Makarova, D. Makarov, V. Karachentseva, S. Sakai, and E. J. Shaya (2006), Advanced Camera for Surveys Imaging of 25 Galaxies in Nearby Groups and in the Field, *AJ*, *131*(3), 1361–1376, doi:10.1086/500013.

Karachentsev, I. D., D. I. Makarov, and E. I. Kaisina (2013), Updated Nearby Galaxy Catalog, *AJ*, *145*, 101, doi:10.1088/0004-6256/145/4/101.

Karachentsev, I. D., et al. (2000), Dwarf spheroidal galaxies in the M81 group imaged with WFPC2, *A&A*, *363*, 117–129.

Karachentseva, V. E., and I. D. Karachentsev (1998), A list of new nearby dwarf galaxy candidates, *A&AS*, *127*, 409–419, doi:10.1051/aas:1998109.

Kauffmann, G. (1996), The age of elliptical galaxies and bulges in a merger model, *MNRAS*, *281*(2), 487–492, doi:10.1093/mnras/281.2.487.

Kennicutt, J., Robert C. (1998), The Global Schmidt Law in Star-forming Galaxies, *ApJ*, *498*(2), 541–552, doi:10.1086/305588.

Kerr, F. J. (1957), A Magellanic effect on the galaxy., *AJ*, *62*, 93–93, doi:10.1086/107466.

Kim, D., H. Jerjen, D. Mackey, G. S. Da Costa, and A. P. Milone (2015), A Hero's Dark Horse: Discovery of an Ultra-faint Milky Way Satellite in Pegasus, *ApJ*, *804*, L44, doi:10.1088/2041-8205/804/2/L44.

Kim, J.-h., et al. (2014), The AGORA High-resolution Galaxy Simulations Comparison Project, *ApJS*, *210*(1), 14, doi:10.1088/0067-0049/210/1/14.

Kim, S. Y., A. H. G. Peter, and J. R. Hargis (2017), There is No Missing Satellites Problem, *ArXiv e-prints*.

King, I. (1962), The structure of star clusters. I. an empirical density law, *AJ*, *67*, 471, doi:10.1086/108756.

Kirby, E. N., J. G. Cohen, P. Guhathakurta, L. Cheng, J. S. Bullock, and A. Gallazzi (2013), The Universal Stellar Mass-Stellar Metallicity Relation for Dwarf Galaxies, *ApJ*, *779*(2), 102, doi:10.1088/0004-637X/779/2/102.

Klypin, A., A. V. Kravtsov, O. Valenzuela, and F. Prada (1999), Where Are the Missing Galactic Satellites?, *ApJ*, *522*, 82–92, doi:10.1086/307643.

Koposov, S. E., V. Belokurov, G. Torrealba, and N. W. Evans (2015), Beasts of the Southern Wild: Discovery of Nine Ultra Faint Satellites in the Vicinity of the Magellanic Clouds., *ApJ*, *805*, 130, doi:10.1088/0004-637X/805/2/130.

Kroupa, P. (2001), On the variation of the initial mass function, *MNRAS*, *322*(2), 231–246, doi:10.1046/j.1365-8711.2001.04022.x.

Laevens, B. P. M., et al. (2015), A New Faint Milky Way Satellite Discovered in the Pan-STARRS1 3π Survey, *ApJ*, *802*, L18, doi:10.1088/2041-8205/802/2/L18.

Lancaster, L., S. E. Koposov, V. Belokurov, N. W. Evans, and A. J. Deason (2019), The halo's ancient metal-rich progenitor revealed with BHB stars, *MNRAS*, *486*(1), 378–389, doi:10.1093/mnras/stz853.

Laporte, C. F. P., K. V. Johnston, F. A. Gómez, N. Garavito-Camargo, and G. Besla (2018), The influence of Sagittarius and the Large Magellanic Cloud on the stellar disc of the Milky Way Galaxy, *MNRAS*, *481*(1), 286–306, doi:10.1093/mnras/sty1574.

Larson, R. B. (1969), A model for the formation of a spherical galaxy, *MNRAS*, *145*, 405, doi:10.1093/mnras/145.4.405.

Lee, M. G., I. S. Jang, R. Beaton, M. Seibert, G. Bono, and B. Madore (2017), The Carnegie-Chicago Hubble Program: Discovery of the Most Distant Ultra-faint Dwarf Galaxy in the Local Universe, *ApJ*, *835*, L27, doi:10.3847/2041-8213/835/2/L27.

Li, Y.-S., and A. Helmi (2008), Infall of substructures on to a Milky Way-like dark halo, *MNRAS*, *385*, 1365–1373, doi:10.1111/j.1365-2966.2008.12854.x.

Lianou, S., E. K. Grebel, and A. Koch (2010), Dwarf spheroidals in the M 81 group - Metallicity distribution functions and population gradients, *A&A*, *521*, A43, doi:10.1051/0004-6361/200913364.

Licquia, T. C., and J. A. Newman (2015), Improved Estimates of the Milky Way's Stellar Mass and Star Formation Rate from Hierarchical Bayesian Meta-Analysis, *ApJ*, *806*(1), 96, doi:10.1088/0004-637X/806/1/96.

Lim, S., N. Hwang, and M. G. Lee (2013), The Star Cluster System in the Nearby Starburst Galaxy M82, *ApJ*, *766*(1), 20, doi:10.1088/0004-637X/766/1/20.

Macciò, A. V., X. Kang, F. Fontanot, R. S. Somerville, S. Koposov, and P. Monaco (2010), Luminosity function and radial distribution of Milky Way satellites in a ΛCDM Universe, *MNRAS*, *402*, 1995–2008, doi:10.1111/j.1365-2966.2009.16031.x.

Mackereth, J. T., and J. Bovy (2020), Weighing the stellar constituents of the galactic halo with APOGEE red giant stars, *MNRAS*, *492*(3), 3631–3646, doi:10.1093/mnras/staa047.

Mackey, D., et al. (2019), Two major accretion epochs in M31 from two distinct populations of globular clusters, *Nature*, *574*(7776), 69–71, doi:10.1038/s41586-019-1597-1.

Madau, P., L. Pozzetti, and M. Dickinson (1998), The Star Formation History of Field Galaxies, *ApJ*, *498*(1), 106–116, doi:10.1086/305523.

Magnier, E. A., et al. (2013), The Pan-STARRS 1 Photometric Reference Ladder, Release 12.01, *The Astrophysical Journal Supplement Series*, *205*, 20, doi:10.1088/0067-0049/205/2/20.

Makarov, D., L. Makarova, L. Rizzi, R. B. Tully, A. E. Dolphin, S. Sakai, and E. J. Shaya (2006), Tip of the Red Giant Branch Distances. I. Optimization of a Maximum Likelihood Algorithm, *AJ*, *132*, 2729–2742, doi:10.1086/508925.

Malhan, K., R. A. Ibata, and N. F. Martin (2018), Ghostly tributaries to the Milky Way: charting the halo's stellar streams with the Gaia DR2 catalogue, *MNRAS*, *481*(3), 3442–3455, doi:10.1093/mnras/sty2474.

Malin, D., and B. Hadley (1997), HI in Shell Galaxies and Other Merger Remnants, , *14*(1), 52–58, doi:10.1071/AS97052.

Martin, N. F., R. A. Ibata, A. W. McConnachie, A. D. Mackey, A. M. N. Ferguson, M. J. Irwin, G. F. Lewis, and M. A. Fardal (2013), The PAndAS View of the Andromeda Satellite System. I. A Bayesian Search for Dwarf Galaxies Using Spatial and Color-Magnitude Information, *ApJ*, *776*, 80, doi:10.1088/0004-637X/776/2/80.

Martínez-Delgado, D., et al. (2010), Stellar Tidal Streams in Spiral Galaxies of the Local Volume: A Pilot Survey with Modest Aperture Telescopes, *AJ*, *140*, 962–967, doi:10.1088/0004-6256/140/4/962.

Mateo, M., E. Olszewski, D. L. Welch, P. Fischer, and W. Kunkel (1991), A Kinematic Study of the Fornax Dwarf Spheroid Galaxy, *AJ*, *102*, 914, doi:10.1086/115923.

Mateo, M., E. W. Olszewski, C. Pryor, D. L. Welch, and P. Fischer (1993), The Carina Dwarf Spheroidal Galaxy: How Dark is it?, *AJ*, *105*, 510, doi:10.1086/116449.

Mateo, M., E. W. Olszewski, S. S. Vogt, and M. J. Keane (1998), The Internal Kinematics of the Leo I Dwarf Spheroidal Galaxy: Dark Matter at the Fringe of the Milky Way, *AJ*, *116*(5), 2315–2327, doi:10.1086/300618.

Mateo, M. L. (1998), Dwarf Galaxies of the Local Group, *ARA&A*, *36*, 435–506, doi:10.1146/annurev.astro.36.1.435.

Mayer, L., F. Governato, M. Colpi, B. Moore, T. Quinn, J. Wadsley, J. Stadel, and G. Lake (2001), The Metamorphosis of Tidally Stirred Dwarf Galaxies, *ApJ*, *559*(2), 754–784, doi:10.1086/322356.

McConnachie, A. W. (2012), The Observed Properties of Dwarf Galaxies in and around the Local Group, *AJ*, *144*, 4, doi:10.1088/0004-6256/144/1/4.

McConnachie, A. W., A. M. N. Ferguson, M. J. Irwin, J. Dubinski, L. M. Widrow, A. Dotter, R. Ibata, and G. F. Lewis (2010), The Photometric Properties of a Vast Stellar Substructure in the Outskirts of M33, *ApJ*, *723*(2), 1038–1052, doi:10.1088/0004-637X/723/2/1038.

McConnachie, A. W., et al. (2018), The Large-scale Structure of the Halo of the Andromeda Galaxy. II. Hierarchical Structure in the Pan-Andromeda Archaeological Survey, *ApJ*, *868*, 55, doi:10.3847/1538-4357/aae8e7.

McGaugh, S. S., and G. D. Bothun (1994), Structural Characteristics and Stellar Composition of Low Surface Brightness Disk Galaxies, *AJ*, *107*, 530, doi:10.1086/116874.

McGaugh, S. S., and W. J. G. de Blok (1998), Testing the Dark Matter Hypothesis with Low Surface Brightness Galaxies and Other Evidence, *ApJ*, *499*(1), 41–65, doi:10.1086/305612.

McKee, C. F., and J. P. Ostriker (1977), A theory of the interstellar medium: three components regulated by supernova explosions in an inhomogeneous substrate., *ApJ*, *218*, 148–169, doi:10.1086/155667.

Melchior, P., et al. (2015), Mass and galaxy distributions of four massive galaxy clusters from Dark Energy Survey Science Verification data, *MNRAS*, *449*(3), 2219–2238, doi:10.1093/mnras/stv398.

Merritt, A., P. van Dokkum, R. Abraham, and J. Zhang (2016), The Dragonfly nearby Galaxies Survey. I. Substantial Variation in the Diffuse Stellar Halos around Spiral Galaxies, *ApJ*, *830*, 62, doi:10.3847/0004-637X/830/2/62.

Miyazaki, S., et al. (2012), Hyper Suprime-Cam, in *Ground-based and Airborne Instrumentation for Astronomy IV*, *Proc. SPIE*, vol. 8446, p. 84460Z, doi:10.1117/12.926844.

Monachesi, A., E. F. Bell, D. J. Radburn-Smith, M. Vlajić, R. S. de Jong, J. Bailin, J. J. Dalcanton, B. W. Holwerda, and D. Streich (2013), Testing Galaxy Formation Models with the GHOSTS Survey: The Color Profile of M81's Stellar Halo, *ApJ*, *766*(2), 106, doi:10.1088/0004-637X/766/2/106.

Monachesi, A., E. F. Bell, D. J. Radburn-Smith, J. Bailin, R. S. de Jong, B. Holwerda, D. Streich, and G. Silverstein (2016a), The GHOSTS survey - II. The diversity of halo colour and metallicity profiles of massive disc galaxies, *MNRAS*, *457*, 1419–1446, doi:10.1093/mnras/stv2987.

Monachesi, A., F. A. Gómez, R. J. J. Grand, G. Kauffmann, F. Marinacci, R. Pakmor, V. Springel, and C. S. Frenk (2016b), On the stellar halo metallicity profile of Milky Way-like galaxies in the Auriga simulations, *MNRAS*, *459*, L46–L50, doi:10.1093/mnrasl/slw052.

Monachesi, A., et al. (2019), The Auriga stellar haloes: connecting stellar population properties with accretion and merging history, *MNRAS*, *485*(2), 2589–2616, doi:10.1093/mnras/stz538.

Moore, B., S. Ghigna, F. Governato, G. Lake, T. Quinn, J. Stadel, and P. Tozzi (1999), Dark Matter Substructure within Galactic Halos, *ApJ*, *524*, L19–L22, doi:10.1086/312287.

Moster, B. P., T. Naab, and S. D. M. White (2013), Galactic star formation and accretion histories from matching galaxies to dark matter haloes, *MNRAS*, *428*, 3121–3138, doi:10.1093/mnras/sts261.

Mountford, C. P. (1956), *Records of the American-Australian Scientific Expedition to Arnhem Land: Vol 1: Art, Myth and Symbolism: Vol 4: Zoology*, Melbourne University Press.

Muñoz, R. P., et al. (2015), Unveiling a Rich System of Faint Dwarf Galaxies in the Next Generation Fornax Survey, *ApJ*, *813*, L15, doi:10.1088/2041-8205/813/1/L15.

Müller, O., H. Jerjen, and B. Binggeli (2015a), New dwarf galaxy candidates in the Centaurus group, *A&A*, *583*, A79, doi:10.1051/0004-6361/201526748.

Müller, O., H. Jerjen, and B. Binggeli (2015b), New dwarf galaxy candidates in the Centaurus group, *A&A*, *583*, A79, doi:10.1051/0004-6361/201526748.

Müller, O., R. Scalera, B. Binggeli, and H. Jerjen (2017), The M 101 group complex: new dwarf galaxy candidates and spatial structure, *A&A*, *602*, A119, doi:10.1051/0004-6361/201730434.

Müller, O., H. Jerjen, and B. Binggeli (2018), The Leo-I group: new dwarf galaxy and ultra diffuse galaxy candidates, *A&A*, *615*, A105, doi:10.1051/0004-6361/201832897.

Munshi, F., A. M. Brooks, E. Applebaum, D. R. Weisz, F. Governato, and T. R. Quinn (2017), Going, going, gone dark: Quantifying the scatter in the faintest dwarf galaxies, *ArXiv e-prints*.

Navarro, J. F., C. S. Frenk, and S. D. M. White (1996), The Structure of Cold Dark Matter Halos, *ApJ*, *462*, 563, doi:10.1086/177173.

Notni, P., I. D. Karachentsev, and L. N. Makarova (2004), The central region of NGC 3077: ground-based photometry and age of bright 'starlike' objects, *Astronomische Nachrichten*, *325*(4), 307–316, doi:10.1002/asna.200310175.

Ocvirk, P., et al. (2016), Cosmic Dawn (CoDa): the First Radiation-Hydrodynamics Simulation of Reionization and Galaxy Formation in the Local Universe, *MNRAS*, *463*, 1462–1485, doi:10.1093/mnras/stw2036.

Okamoto, S., N. Arimoto, A. M. N. Ferguson, E. J. Bernard, M. J. Irwin, Y. Yamada, and Y. Utsumi (2015), A Hyper Suprime-Cam View of the Interacting Galaxies of the M81 Group, *ApJ*, *809*, L1, doi:10.1088/2041-8205/809/1/L1.

Papastergis, E., R. Giovanelli, M. P. Haynes, and F. Shankar (2015), Is there a "too big to fail" problem in the field?, *A&A*, *574*, A113, doi:10.1051/0004-6361/201424909.

Pawlowski, M. S., P. Kroupa, and H. Jerjen (2013), Dwarf galaxy planes: the discovery of symmetric structures in the Local Group, *MNRAS*, *435*, 1928–1957, doi:10.1093/mnras/stt1384.

Peebles, P. J. E. (1978), Stability of a hierarchical clustering pattern in the distribution of galaxies., *A&A*, *68*(3), 345–352.

Peebles, P. J. E. (1982), Large-scale background temperature and mass fluctuations due to scale-invariant primeval perturbations, *ApJ*, *263*, L1–L5, doi:10.1086/183911.

Pillepich, A., P. Madau, and L. Mayer (2015), Building Late-type Spiral Galaxies by In-situ and Ex-situ Star Formation, *ApJ*, *799*(2), 184, doi:10.1088/0004-637X/799/2/184.

Pillepich, A., et al. (2014), Halo mass and assembly history exposed in the faint outskirts: the stellar and dark matter haloes of Illustris galaxies, *MNRAS*, *444*(1), 237–249, doi:10.1093/mnras/stu1408.

Press, W. H., and P. Schechter (1974), Formation of Galaxies and Clusters of Galaxies by Self-Similar Gravitational Condensation, *ApJ*, *187*, 425–438, doi:10.1086/152650.

Purcell, C. W., J. S. Bullock, and S. Kazantzidis (2010), Heated disc stars in the stellar halo, *MNRAS*, *404*(4), 1711–1718, doi:10.1111/j.1365-2966.2010.16429.x.

Querejeta, M., et al. (2015), The Spitzer Survey of Stellar Structure in Galaxies (S^4G): Precise Stellar Mass Distributions from Automated Dust Correction at 3.6 μm, *ApJS*, *219*, 5, doi:10.1088/0067-0049/219/1/5.

Radburn-Smith, D. J., et al. (2011), The GHOSTS Survey. I. Hubble Space Telescope Advanced Camera for Surveys Data, *ApJS*, *195*, 18, doi:10.1088/0067-0049/195/2/18.

Rejkuba, M., W. E. Harris, L. Greggio, and G. L. H. Harris (2011), How old are the stars in the halo of NGC 5128 (Centaurus A)?, *A&A*, *526*, A123, doi:10.1051/0004-6361/201015640.

Rejkuba, M., W. E. Harris, L. Greggio, G. L. H. Harris, H. Jerjen, and O. A. Gonzalez (2014), Tracing the Outer Halo in a Giant Elliptical to 25 R $_{eff}$, *ApJ*, *791*(1), L2, doi:10.1088/2041-8205/791/1/L2.

Richstone, D. O. (1976), Collisions of galaxies in dense clusters. II. Dynamical evolution of cluster galaxies., *ApJ*, *204*, 642–648, doi:10.1086/154213.

Rodríguez-Merino, L. H., D. Rosa-González, and Y. D. Mayya (2011), Spatially Resolved Star Formation History Along the Disk of M82 Using Multi-band Photometric Data, *ApJ*, *726*(1), 51, doi:10.1088/0004-637X/726/1/51.

Rubin, V. C. (1983), The Rotation of Spiral Galaxies, *Science*, *220*(4604), 1339–1344, doi:10.1126/science.220.4604.1339.

Ryden, B. S., and J. E. Gunn (1987), Galaxy Formation by Gravitational Collapse, *ApJ*, *318*, 15, doi:10.1086/165349.

Sabbi, E., J. S. Gallagher, L. J. Smith, D. F. de Mello, and M. Mountain (2008), Holmberg IX: The Nearest Young Galaxy, *ApJ*, *676*(2), L113, doi:10.1086/587548.

Samuel, J., et al. (2020), A profile in FIRE: resolving the radial distributions of satellite galaxies in the Local Group with simulations, *MNRAS*, *491*(1), 1471–1490, doi:10.1093/mnras/stz3054.

Sand, D. J., K. Spekkens, D. Crnojević, J. R. Hargis, B. Willman, J. Strader, and C. J. Grillmair (2015), Antlia B: A Faint Dwarf Galaxy Member of the NGC 3109 Association, *ApJ*, *812*, L13, doi:10.1088/2041-8205/812/1/L13.

Sanders, D. B., and I. F. Mirabel (1996), Luminous Infrared Galaxies, *ARA&A*, *34*, 749, doi:10.1146/annurev.astro.34.1.749.

Sanderson, R. E., S. Garrison-Kimmel, A. Wetzel, T. Keung Chan, P. F. Hopkins, D. Kereš, I. Escala, C.-A. Faucher-Giguère, and X. Ma (2018), Reconciling Observed and Simulated Stellar Halo Masses, *ApJ*, *869*(1), 12, doi:10.3847/1538-4357/aaeb33.

Sawala, T., et al. (2015), Bent by baryons: the low-mass galaxy-halo relation, *MNRAS*, *448*, 2941–2947, doi:10.1093/mnras/stu2753.

Sawala, T., et al. (2016), The APOSTLE simulations: solutions to the Local Group's cosmic puzzles, *MNRAS*, *457*, 1931–1943, doi:10.1093/mnras/stw145.

Schaye, J., et al. (2015), The EAGLE project: simulating the evolution and assembly of galaxies and their environments, *MNRAS*, *446*, 521–554, doi:10.1093/mnras/stu2058.

Schlafly, E. F., and D. P. Finkbeiner (2011a), Measuring Reddening with Sloan Digital Sky Survey Stellar Spectra and Recalibrating SFD, *ApJ*, *737*, 103, doi:10.1088/0004-637X/737/2/103.

Schlafly, E. F., and D. P. Finkbeiner (2011b), Measuring Reddening with Sloan Digital Sky Survey Stellar Spectra and Recalibrating SFD, *ApJ*, *737*, 103, doi:10.1088/0004-637X/737/2/103.

Schlegel, D. J., D. P. Finkbeiner, and M. Davis (1998), Maps of Dust Infrared Emission for Use in Estimation of Reddening and Cosmic Microwave Background Radiation Foregrounds, *ApJ*, *500*, 525–553, doi:10.1086/305772.

Schmidt-Kaler, T. (1967), Reddening and distance of M33 and M31 as derived from open clusters, *AJ*, *72*, 526, doi:10.1086/110260.

Searle, L., and R. Zinn (1978), Composition of halo clusters and the formation of the galactic halo., *ApJ*, *225*, 357–379, doi:10.1086/156499.

Shao, S., M. Cautun, C. S. Frenk, R. J. J. Grand, F. A. Gómez, F. Marinacci, and C. M. Simpson (2018), The multiplicity and anisotropy of galactic satellite accretion, *MNRAS*, *476*, 1796–1810, doi:10.1093/mnras/sty343.

Sheth, K., et al. (2010), The Spitzer Survey of Stellar Structure in Galaxies (S4G), *PASP*, *122*, 1397, doi:10.1086/657638.

Shu, F. H., F. C. Adams, and S. Lizano (1987), Star formation in molecular clouds: observation and theory., *ARA&A*, *25*, 23–81, doi:10.1146/annurev.aa.25.090187.000323.

Sick, J. (2018), The Andromeda Optical and Infrared Disk Survey, Ph.D. thesis, Queen's University (Canada).

Simon, J. D., and M. Geha (2007), The Kinematics of the Ultra-faint Milky Way Satellites: Solving the Missing Satellite Problem, *ApJ*, *670*, 313–331, doi:10.1086/521816.

Simon, J. D., A. D. Bolatto, A. Leroy, and L. Blitz (2003), High-Resolution Measurements of the Dark Matter Halo of NGC 2976: Evidence for a Shallow Density Profile, *ApJ*, *596*(2), 957–981, doi:10.1086/378200.

Simon, J. D., A. D. Bolatto, A. Leroy, L. Blitz, and E. L. Gates (2005), High-Resolution Measurements of the Halos of Four Dark Matter-Dominated Galaxies: Deviations from a Universal Density Profile, *ApJ*, *621*(2), 757–776, doi:10.1086/427684.

Simpson, C. M., R. J. J. Grand, F. A. Gómez, F. Marinacci, R. Pakmor, V. Springel, D. J. R. Campbell, and C. S. Frenk (2018), Quenching and ram pressure stripping of simulated Milky Way satellite galaxies, *MNRAS*, *478*(1), 548–567, doi:10.1093/mnras/sty774.

Slater, C. T., and E. F. Bell (2014), The Mass Dependence of Dwarf Satellite Galaxy Quenching, *ApJ*, *792*, 141, doi:10.1088/0004-637X/792/2/141.

Smercina, A., E. F. Bell, C. T. Slater, P. A. Price, J. Bailin, and A. Monachesi (2017), D1005+68: A New Faint Dwarf Galaxy in the M81 Group, *ApJ*, *843*, L6, doi:10.3847/2041-8213/aa78fa.

Smercina, A., E. F. Bell, P. A. Price, R. D'Souza, C. T. Slater, J. Bailin, A. Monachesi, and D. Nidever (2018), A Lonely Giant: The Sparse Satellite Population of M94 Challenges Galaxy Formation, *ApJ*, *863*, 152, doi:10.3847/1538-4357/aad2d6.

Smercina, A., et al. (2019), The Saga of M81: Global View of a Massive Stellar Halo in Formation, *arXiv e-prints*, arXiv:1910.14672.

Spencer, M., S. Loebman, and P. Yoachim (2014), A Survey of Satellite Galaxies around NGC 4258, *ApJ*, *788*, 146, doi:10.1088/0004-637X/788/2/146.

Spight, L., and E. Grayzeck (1977), Warping of the galactic plane by the LMC., *ApJ*, *213*, 374–378, doi:10.1086/155165.

Spitzer, J., Lyman, and S. L. Shapiro (1972), Random Gravitational Encounters and the Evolution of Spherical Systems. III. Halo, *ApJ*, *173*, 529, doi:10.1086/151442.

Springel, V., and L. Hernquist (2005), Formation of a Spiral Galaxy in a Major Merger, *ApJ*, *622*(1), L9–L12, doi:10.1086/429486.

Springel, V., T. Di Matteo, and L. Hernquist (2005), Black Holes in Galaxy Mergers: The Formation of Red Elliptical Galaxies, *ApJ*, *620*(2), L79–L82, doi:10.1086/428772.

Streich, D., R. S. de Jong, J. Bailin, P. Goudfrooij, D. Radburn-Smith, and M. Vlajic (2014), On the relation between metallicity and RGB color in HST/ACS data, *A&A*, *563*, A5, doi:10.1051/0004-6361/201220956.

Telford, O. G., J. K. Werk, J. J. Dalcanton, and B. F. Williams (2019), Spatially Resolved Metal Loss from M31, *ApJ*, *877*(2), 120, doi:10.3847/1538-4357/ab1b3f.

Terrazas, B. A., et al. (2020), The relationship between black hole mass and galaxy properties: examining the black hole feedback model in IllustrisTNG, *MNRAS*, *493*(2), 1888–1906, doi:10.1093/mnras/staa374.

Tinsley, B. M., and R. B. Larson (1978), Chemical evolution and the formation of galactic disks., *ApJ*, *221*, 554–561, doi:10.1086/156056.

Tohline, J. E. (1980), The gravitational fragmentation of primordial gas clouds, *ApJ*, *239*, 417–427, doi:10.1086/158125.

Toloba, E., et al. (2016), A Tidally Disrupting Dwarf Galaxy in the Halo of NGC 253, *ApJ*, *816*, L5, doi:10.3847/2041-8205/816/1/L5.

Toomre, A., and J. Toomre (1972), Galactic Bridges and Tails, *ApJ*, *178*, 623–666, doi:10.1086/151823.

Trujillo, I., I. Martinez-Valpuesta, D. Martínez-Delgado, J. Peñarrubia, R. J. Gabany, and M. Pohlen (2009), Unveiling the Nature of M94's (NGC4736) Outer Region: A Panchromatic Perspective, *ApJ*, *704*, 618–628, doi:10.1088/0004-637X/704/1/618.

Tully, R. B., and J. R. Fisher (1977), Reprint of 1977A&A....54..661T. A new method of determining distance to galaxies., *A&A*, *500*, 105–117.

van den Bergh, S. (1974), The Dwarf Spheroidal Companions to the Andromeda Nebula, *ApJ*, *191*, 271–272, doi:10.1086/152964.

van den Bosch, F. C., B. E. Robertson, J. J. Dalcanton, and W. J. G. de Blok (2000), Constraints on the Structure of Dark Matter Halos from the Rotation Curves of Low Surface Brightness Galaxies, *AJ*, *119*(4), 1579–1591, doi:10.1086/301315.

van den Bosch, F. C., X. Yang, and H. J. Mo (2003), Linking early- and late-type galaxies to their dark matter haloes, *MNRAS*, *340*(3), 771–792, doi:10.1046/j.1365-8711.2003.06335.x.

Vogelsberger, M., S. Genel, V. Springel, P. Torrey, D. Sijacki, D. Xu, G. Snyder, D. Nelson, and L. Hernquist (2014), Introducing the Illustris Project: simulating the coevolution of dark and visible matter in the Universe, *MNRAS*, *444*, 1518–1547, doi:10.1093/mnras/stu1536.

von Hoerner, S. (1957), Internal structure of globular clusters, *ApJ*, *125*, 451, doi:10.1086/146321.

Watkins, A. E., J. C. Mihos, and P. Harding (2016), The Red and Featureless Outer Disks of Nearby Spiral Galaxies, *ApJ*, *826*, 59, doi:10.3847/0004-637X/826/1/59.

Wechsler, R. H., and J. L. Tinker (2018), The Connection Between Galaxies and Their Dark Matter Halos, *ARA&A*, *56*, 435–487, doi:10.1146/annurev-astro-081817-051756.

Weisz, D. R., A. E. Dolphin, E. D. Skillman, J. Holtzman, K. M. Gilbert, J. J. Dalcanton, and B. F. Williams (2014), The Star Formation Histories of Local Group Dwarf Galaxies. I. Hubble Space Telescope/Wide Field Planetary Camera 2 Observations, *ApJ*, *789*(2), 147, doi:10.1088/0004-637X/789/2/147.

Weisz, D. R., et al. (2019), Comparing the Quenching Times of Faint M31 and Milky Way Satellite Galaxies, *ApJ*, *885*(1), L8, doi:10.3847/2041-8213/ab4b52.

Weldrake, D. T. F., W. J. G. de Blok, and F. Walter (2003), A high-resolution rotation curve of NGC 6822: a test-case for cold dark matter, *MNRAS*, *340*(1), 12–28, doi:10.1046/j.1365-8711.2003.06170.x.

Wetzel, A. R., A. J. Deason, and S. Garrison-Kimmel (2015), Satellite Dwarf Galaxies in a Hierarchical Universe: Infall Histories, Group Preprocessing, and Reionization, *ApJ*, *807*(1), 49, doi:10.1088/0004-637X/807/1/49.

Wetzel, A. R., P. F. Hopkins, J.-h. Kim, C.-A. Faucher-Giguère, D. Kereš, and E. Quataert (2016), Reconciling Dwarf Galaxies with ΛCDM Cosmology: Simulating a Realistic Population of Satellites around a Milky Way-mass Galaxy, *ApJ*, *827*, L23, doi:10.3847/2041-8205/827/2/L23.

White, S. D. M., and M. J. Rees (1978), Core condensation in heavy halos - A two-stage theory for galaxy formation and clustering, *MNRAS*, *183*, 341–358, doi:10.1093/mnras/183.3.341.

Williams, B. F., et al. (2015), Tracing the Metal-poor M31 Stellar Halo with Blue Horizontal Branch Stars, *ApJ*, *802*, 49, doi:10.1088/0004-637X/802/1/49.

Williams, B. F., et al. (2017), PHAT. XIX. The Ancient Star Formation History of the M31 Disk, *ApJ*, *846*(2), 145, doi:10.3847/1538-4357/aa862a.

Willman, B., M. R. Blanton, A. A. West, J. J. Dalcanton, D. W. Hogg, D. P. Schneider, N. Wherry, B. Yanny, and J. Brinkmann (2005a), A New Milky Way Companion: Unusual Globular Cluster or Extreme Dwarf Satellite?, *AJ*, *129*(6), 2692–2700, doi:10.1086/430214.

Willman, B., et al. (2005b), A New Milky Way Dwarf Galaxy in Ursa Major, *ApJ*, *626*(2), L85–L88, doi:10.1086/431760.

Yang, X., H. J. Mo, and F. C. van den Bosch (2008), Galaxy Groups in the SDSS DR4. II. Halo Occupation Statistics, *ApJ*, *676*(1), 248–261, doi:10.1086/528954.

Yaryura, C. Y., A. Helmi, M. G. Abadi, and E. Starkenburg (2016), The low-mass end of the neutral gas mass and velocity width functions of galaxies in ΛCDM, *MNRAS*, *457*, 2415–2422, doi:10.1093/mnras/stw139.

York, D. G., et al. (2000), The Sloan Digital Sky Survey: Technical Summary, *AJ*, *120*(3), 1579–1587, doi:10.1086/301513.

Yun, M. S., P. T. P. Ho, and K. Y. Lo (1994), A high-resolution image of atomic hydrogen in the M81 group of galaxies, *Nature*, *372*, 530–532, doi:10.1038/372530a0.

Zolotov, A., B. Willman, A. M. Brooks, F. Governato, C. B. Brook, D. W. Hogg, T. Quinn, and G. Stinson (2009), The Dual Origin of Stellar Halos, *ApJ*, *702*(2), 1058–1067, doi:10.1088/0004-637X/702/2/1058.

Zolotov, A., et al. (2012), Baryons Matter: Why Luminous Satellite Galaxies have Reduced Central Masses, *ApJ*, *761*(1), 71, doi:10.1088/0004-637X/761/1/71.

Zucker, D. B., et al. (2006a), A New Milky Way Dwarf Satellite in Canes Venatici, *ApJ*, *643*(2), L103–L106, doi:10.1086/505216.

Zucker, D. B., et al. (2006b), A Curious Milky Way Satellite in Ursa Major, *ApJ*, *650*(1), L41–L44, doi:10.1086/508628.

Zwaan, M. A., J. M. van der Hulst, W. J. G. de Blok, and S. S. McGaugh (1995), The Tully-Fisher relation for low surface brightness galaxies: implications for galaxy evolution, *MNRAS*, *273*(2), L35–L38, doi:10.1093/mnras/273.1.L35.